Laboratoire de Mécanique des Sols (LMS)

Prof. Lyesse Laloui, Director

Phone/fax: +41(0)216932315/4153
Web: http://lms.epfl.ch/

ÉCOLE POLYTECHNIQUE
FÉDÉRALE DE LAUSANNE

CAPROCK:

Experimental assessment of geomechanics of deep carbon dioxide sequestration

FINAL REPORT 2014/16

Prepared by: *Roman Makhnenko, Ph.D.*

For : Office federal de l'énergie (OFEN)
C/o CDS FI DFF
3003 Berne

No commande :810002355

No de contrat : SI/501138-01

No du TP : 81000878

1 Introduction

This report summarizes the activities at the Laboratory of Soil Mechanics - Chair “Gaz Naturel” Petrosvibri at the Swiss Federal Institute of Technology in Lausanne (LMS-EPFL) related to the project “CAPROCK: Experimental assessment of geomechanics of deep carbon dioxide sequestration”. The support for the project was provided by the Swiss Federal Office of Energy and partially covered the activities of a postdoctoral researcher.

The main goal of the project was building the expertise in experimental testing of geomechanical response of materials that possess properties of host and caprocks for geological storage of CO_2. The characterization of changes in thermo-hydro-mechanical behaviour of rock due to high pressure CO_2 injection through triaxial and oedometric compression tests, with microimaging techniques and the chemical analyses, was performed on the equipment developed at the LMS-EPFL or available at other laboratories at the EPFL.

The report is organized in the following way. Personnel that participated to the project is listed in Chapter 2. Chapter 3 gives a brief summary of the postdoc’s research activities related to both laboratory experiments and modelling. Other activities, including published papers, conference presentations, and collaborations with other groups are provided in Chapter 4. Intermediate reports, conference abstracts and posters, and conference and journal papers are contained in the Appendices.

2 Personnel

The following personnel have been contributing to the CAPROCK project from December 2014 to November 2016:

- **Lyesse Laloui,** Ph.D., Professor and Director of LMS-EPFL, manager of the project
- **Roman Makhnenko,** Ph.D., postdoctoral researcher at LMS-EPFL, responsible for running all experimental activities, supervising the involved students, writing reports and papers, and presenting the results at national and international conferences.

- **Danila Mylnikov,** M.Sc., research assistant at LMS-EPFL that was supervised by Prof. Lyesse Laloui and Dr. Roman Makhnenko and was involved in the experimental characterization of reservoir and caprock response in contact with CO_2.

- **Patrick Dubey,** technician assistant at LMS-EPFL, responsible for the help with the experimental equipment and specimen preparation.

3 Scientific content

The objective of the project was to characterize thermo-hydro-mechanical behavior of possible host and cap rocks for geologic carbon dioxide sequestration in contact with brine and supercritical CO_2. Changes in parameters governing the poromechanical and flow properties of Berea sandstone, Indiana limestone, and Opalinus clay (Jurassic shale) due to CO_2 injection were measured in triaxial and oedometric compression tests and with microimaging techniques.

The designated milestones were the following:

1) development of equipment that allows laboratory testing of geomaterials in contact with CO_2;

2) characterization of brine-saturated host and cap rock response;

3) experimental characterization of the effect of CO_2 injection on permeability and mechanical properties;

4) constitutive modelling of carbon dioxide effect on geomechanical response of rock-like materials.

The obtained results are delivered in terms of presentations at national and international scientific conferences and publications in international scientific journals, which are put in the appendices.

To address the milestone #1, high-pressure oedometric cell and advanced triaxial cell allowing separate control of brine and CO_2 pressures upstream and downstream were developed. The devices were put inside the thermostat room, where the temperature can be controlled between 8 – 48 ˚C with the accuracy of ±0.1 ˚C, thus providing the possibility for both liquid and supercritical CO_2 injection. The description of the oedometric system is given in appendices A2, B3, and D2. Short summary on the advanced triaxial cell is provided in appendix D3. A paper on the calibration of the triaxial apparatus and thermo-hydro-mechanical tests on shale performed in it is in preparation.

Milestone #2 was addressed by measuring poroviscoelastic properties of Berea sandstone, Indiana limestone, and remolded and intact Opalinus clay in oedometric and triaxial tests. The results are presented in appendices A2, B3, C1, C2, and D1 – D4.

Work on the milestone #3 included liquid (24 ˚C) and supercritical (40 ˚C) CO_2 injection in sandstone, remolded shale, and intact shale specimens to study its breakthrough and flow through the rock. Additionally, drained oedometric modulus was measured at different stages of injection and no significant change in mechanical properties of both the sandstone and the shale were observed. The results of the tests on CO_2 breakthrough and flow in rock can be found in appendices A2, B3, B4, and D1.

Obtained experimental data was used as the basis for the constitutive modelling of material behavior for rock in contact with high-pressure CO_2 (milestone #4). Analytical model for injection induced caprock cooling is considered in appendix C1. Brine flow tests in shale are believed to cause the chemical effect on the material and the adsorption model was used to interpret the experimental data (Appendix C2). The problem of fault reactivation during CO_2 injection is approached from the numerical modeling point of view (appendices D1 and D4). The deformation of caprock was found to be time-dependent and poroviscoelastic model was used to predict the long-term caprock behavior and possibility of fluid flow instabilities (porosity waves) creation (Appendix D3). A paper that will address the relationship between breakthrough pressure, effective stresses, temperature, and microstructure of the caprock (shale) is in preparation.

4 Outcomes

4.1 Publications

4.1.1 Journal papers

1) Vilarrasa, V., R.Y. Makhnenko, and S. Gheibi. 2016. Geomechanical analysis of the influence of CO_2 injection location on fault stability. *J. Rock Mech. Geotech. Eng.,* doi: 10.1016/j.jrmge.2016.06.006. **(Appendix D1)**
2) Makhnenko, R.Y., V. Vilarrasa, D. Mylnikov, and L. Laloui. 2017. Hydromechanical aspects of CO_2 breakthrough into clay-rich caprock. Accepted at *Energy Procedia*. **(Appendix D2)**
3) Räss, L., R.Y. Makhnenko, Y. Podladchikov, and L. Laloui. 2017. Quantification of viscous creep influence on storage capacity of caprock. Accepted at *Energy Procedia*. **(Appendix D3)**
4) Vilarrasa, V., R.Y. Makhnenko, and L. Laloui. 2017. Potential for fault reactivation due to CO_2 injection in a semi-closed saline aquifer. Accepted at *Energy Procedia.* **(Appendix D4)**

4.1.2 Conference papers

1) Vilarrasa, V., R. Makhnenko, and L. Laloui, 2015. Influence of petrophysical and thermal properties of the caprock on the safety of CO_2 storage. *2nd EAGE Workshop on Geomechanics and Energy*, Celle, Germany, 13-15 October 2015. **(Appendix C1)**
2) Cassini, E., D. Mylnikov, and R. Makhnenko. 2017. Chemical influence of pore pressure on brine flow in clay-rich material. In: L. Laloui, A. Ferrari (eds), *Advances in Laboratory Testing and Modelling of Soils and Shales*. Springer Series in Geomechanics and Geoengineering. **(Appendix C2)**

4.1.3 Conference abstracts and posters

1) Makhnenko, R., D. Mylnikov, and L. Laloui, 2015. Effect of liquid and supercritical CO_2 injection on petrophysical properties of rock. *13th Swiss Geoscience Meeting, Basel*. **(Appendix B1)**
2) Makhnenko, R., D. Mylnikov, V. Vilarrasa, and L. Laloui, 2016. Thermo-hydro-mechanical aspects of caprock – CO_2 interaction for safe geological storage. *14th Swiss Geoscience Meeting, Geneva*. **(Appendix B2)**
3) Makhnenko, R., D. Mylnikov, and L. Laloui, 2016. Impact of liquid and supercritical CO_2 injection on host rock properties. *SCCER Annual Conference 2015*. **(Appendix B3)**
4) Makhnenko, R., D. Mylnikov, V. Vilarrasa, and L. Laloui, 2016. Hydromechanical aspects of CO_2 breakthrough and flow in clay-rich caprock. *SCCER Annual Conference 2016*. **(Appendix B4)**

4.2 Presentations given by Dr. Makhnenko

1) Technical Meeting - 33, Mont Terri, Switzerland, February 2015
Laboratory testing of caprock properties for safe CO_2 *sequestration*
2) 4th Poroelasticity Minisymposium, ETH Zürich, February 2015
Effect of non-connected porosity on poroelastic response of host and cap rock
3) 1st Geomechanical Workshop: EPFL – Masdar Institute, Lausanne, April 2015
Laboratory characterization of reservoir rock
4) World Gas Congress, Paris, June 2015
Geomechanics of deep CO_2 *storage*
5) SCCER-SoE coordination meeting, Lausanne, June 2015
Reservoir modelling and validation
6) SCCER-SoE Annual conference, Neuchatel, September 2015
Impact of liquid and supercritical CO_2 *injection on host rock properties (poster)*
7) 13th Swiss Geoscience Meeting, Basel, November 2015
Effect of liquid and supercritical CO_2 *injection on petrophysical properties of rock*
8) University of Lausanne, Geophysical seminar, November 2015
Effect of cracks on static and dynamic moduli of rock
9) University of Bern, Rock-water interaction seminar, December 2015
Chemo-visco-poromechanical behavior of rock associated with deep CO_2 *storage*
10) EPFL, 80th Anniversary of the Geotechnical Engineering Group, January 2016
Effect of CO_2 *injection on rock properties*
11) Technical Meeting - 34, Mont Terri, Switzerland, February 2016
Laboratory tests on caprock – CO_2 *interaction for the purposes of deep geological storage*
12) SCCER-SoE Annual conference, Sion, September 2016
Hydromechanical aspects of CO_2 *breakthrough and flow in clay-rich caprock (poster)*
13) 13th Int. Conf. on Greenhouse Gas Control Technologies, Lausanne, November 2016
Potential for fault reactivation due to CO_2 *injection in a semi-closed saline aquifer (poster)*
14) 13th Int. Conf. on Greenhouse Gas Control technologies, Lausanne, November 2016
Hydromechanical aspects of CO_2 *breakthrough into clay-rich caprock*
15) 14th Swiss Geoscience Meeting, Geneva, November 2016
Thermo-hydro-mechanical aspects of caprock – CO_2 *interaction for safe geological storage.*

4.3 Scientific collaboration

1) **Visit of Prof. Marcelo Sanchez, Department of Civil Engineering, TEXAS A&M University, USA**

   Prof. Sanchez visited Laboratory of Soil Mechanics in July - August 2015 and participated to the activities of the group, specifically those related to coupled thermo-hydro-mechanical & geochemical analysis in geomechanics.

2) **Visit of Prof. Joseph Labuz, Department of Civil, Environmental, and Geo-Engineering, University of Minnesota – twin Cities, USA**

   Prof. Labuz visited Laboratory of Soil Mechanics in January 2016 and participated to the discussions related to assessment of proper experimental techniques for studying tight rock behavior.

3) **Collaboration with the group of Prof. Yury Podladchikov, Institute of Earth Sciences, University of Lausanne**

   The group has established the collaboration with Prof. Podladchikov. His group is performing the 3D modelling of reservoir and caprock behaviour including visco-elastoplastic effects caused by high-pressure fluid injection.

4) **Collaboration with the group of Prof. Larryn Diamond, Institute of Geology, University of Bern**

   The collaboration with the research group of Prof. Diamond was established during 2015. The group at the University of Bern shares its expertise in geochemistry with applications to $scCO_2$ flow in host and caprock.

5) **Collaboration with the group of Prof. Klaus Holliger, Institute of Earth Sciences, University of Lausanne**

   The collaboration with the research group of Prof. Holliger was established for the purposes of combining geophysical and geomechanical methods in testing and modelling the behavior of low-permeable materials.

4.4 Network and relations with other research institutes and industry

1) **Reservoir modeling and validation for Geoenergies**

   Swiss Competence Center for Energy Research – Supply of Electricity (SCCER-SoE) carries out innovative and sustainable research in the areas of geo-energy and hydropower. Roman Makhnenko contributed to SCCER-SoE Task 1.2 “Reservoir modeling and validation”, which involves the development of numerical and experimental methods to quantify the thermal, hydraulic, rock mechanical, and geochemical processes acting in deep reservoirs. The extended experimental research program on different scales (up to large-scale underground laboratories) allows studying mechanical reservoir creation processes, caprock leakage and chemical fluid-rock interactions.

2) **CS-C Experiment: Experimental assessment of shale properties for safe geological CO_2 storage**

   Roman Makhnenko contributed to the research at underground rock laboratory in Mont Terri, JU, Switzerland. The CS-C is supported by the members of the Mont Terri consortium: Swisstopo (Switzerland) and FANC (Belgium).

3) **Roadmap towards a full-chain pilot test of CCS in Switzerland**

   The LMS-EPFL is participating in the preparation of the integral CCS project in Switzerland in 2013 -2020 along with the other institutions like ETHZ, University of Bern, and PSI, and companies like Geoform Ltd., GeoExplorers, Alstom and Ecosens. The particular contribution the LMS makes is in the field of reservoir modelling and validation. The goal of the project is to perform *in-situ* injection experiments under a fully controlled environment at increasing depths, to provide a testing ground integrating experimental, modeling and monitoring technologies, to develop and test innovative methodologies for reservoir engineering, and to increase public confidence in geo-energy technologies.

Appendices

Appendix A: Intermediate reports on CAPROCK project

A1 - Report #1 (December 2014).

A2 - Report #2 (December 2015).

Appendix B: Conference posters and abstracts

B1 - Effect of liquid and supercritical CO_2 injection on petrophysical properties of rock.

B2 - Thermo-hydro-mechanical aspects of caprock – CO_2 interaction for safe geological storage.

B3 - Impact of liquid and supercritical CO_2 injection on host rock properties.

B4 - Hydromechanical aspects of CO_2 breakthrough and flow in clay-rich caprock.

Appendix C: Conference papers

C1 - Influence of petrophysical and thermal properties of the caprock on the safety of CO_2 storage.

C2 - Chemical influence of pore pressure on brine flow in clay-rich material.

Appendix D: Journal papers

D1 - Geomechanical analysis of the influence of CO_2 injection location on fault stability.

D2 - Hydromechanical aspects of CO_2 breakthrough into clay-rich caprock.

D3 - Quantification of viscous creep influence on storage capacity of caprock.

D4 - Potential for fault reactivation due to CO_2 injection in a semi-closed saline aquifer.

Appendix A

Intermediate reports for CAPROCK project

Experimental assessment of geomechanics of deep carbon dioxide sequestration

Report #1 (December 2014)

Overview

The research group at the Soil Mechanics Laboratory – Chair "Gaz Naturel" Petrosvibri at the EPFL deals with characterization of thermo-hydro-mechanical behavior of possible host and caprocks for geologic carbon dioxide sequestration in contact with brine and supercritical CO_2. This report briefly describes the activities of the group in December 2014.

Scope of the research

CO_2 storage security, especially in the early stages after the start of injection, is largely influenced by the caprock integrity. The lower boundary of the caprock will be in contact with carbon dioxide saturated pore water or pore fluid consisting of pure CO_2. Chemical interaction between the pore fluid and the cap rock may change the material properties of the latter one. Therefore, knowledge of the composition of the seal rock as well as the formation waters is important to gauge geochemical properties and the minerals formed after CO_2 injection. Additionally, the upward movement of carbon dioxide through the pore system is resisted by capillary pressure. Seal capacity then refers to a maximum CO_2 column height that can be retained in the underlying reservoir, before pressure exerted by buoyancy exceeds capillary entry pressure, thus allowing CO_2 to migrate through the caprock (IAEGHG 2011). Understanding the geomechanical properties of the caprock, the change in stress state with carbon dioxide injection, and identification and understanding of changes in material properties as a result of interaction with CO_2-rich fluids are essential for the overall evaluation of its sealing capacity. In this study, Opalinus clay (shaly facies) from Mont Terri is used as a representative of a possible caprock for geological storage of carbon dioxide in Switzerland.

Research achievements

Factors that control capillary entry pressures in the caprock are: size of pore throats, CO_2-water interfacial tension, and wettability of CO_2 to rock in the presence of water. The first one is measured with Mercury Intrusion Porosimetry (MIP) and the result is presented in Figure 1. It appears that the dominant pore radius for Opalinus clay is 13 nm. Additionally, surface electron microscopy analysis was performed on the material and revealed involved pore morphology of the shale with a several pores of a few micrometer size and lots of small voids with a submicron diameter (Figure 1).

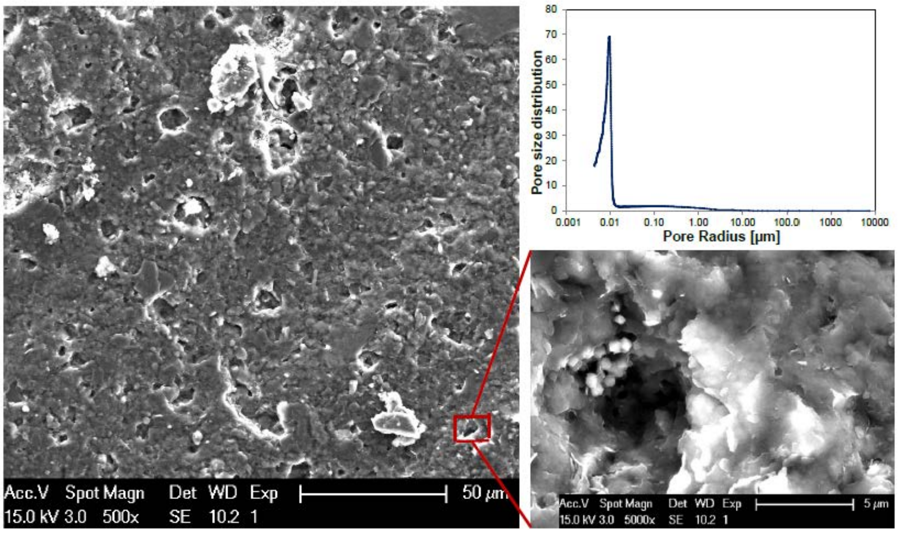

Figure 1: Microphotographs and the result of MIP test on Opalinus clay from Mont Terri.

The measurements of an interfacial tension and contact angle of CO_2-water-shale system require some special instruments, because of the high air and CO_2 entry values of shales. The experimental techniques that allow these measurements are being developed. In the meantime, based on the water retention curve previously obtained for Opalinus clay (Ferrari and Laloui 2012) and the available data on CO_2-water-kaolinite contact angle and interfacial tension (IEAGHG 2011) at room temperature, the prediction on CO_2 retention properties of the caprock was made (Figure 2). Additionally, the remolded shale, which has the same solid density and dominant pore size as the in-situ material, is used to evaluate the wettability of CO_2-water-shale forming minerals system.

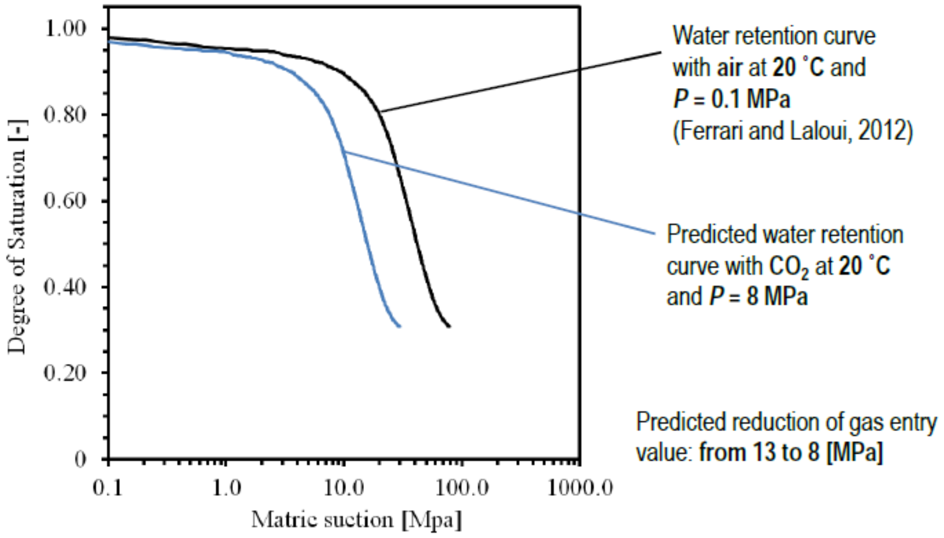

Figure 2: Measured water retention curve (Ferrari and Laloui, 2012) and predicted liquid CO_2 retention behaviour of Opalinus clay from Mont Terri.

Future work on caprock – carbon dioxide interaction.

The proposed research for 2015 deals with the following aspects of CO_2–caprock interaction:

- measuring permeability of the shale with respect to brine-CO_2 mixture and the mineral trapping at in-situ conditions;
- assessment of the poromechanical properties and strength parameters of shale and changes in them due to carbon dioxide injection;
- investigation of the chemical effect of injected CO_2 on the shale: the change of microstructure and porosity of the specimens will be studied with Scanning Electron Microscopy and Mercury Intrusion Porosimetry techniques.

References:

Ferrari, A. and Laloui, L., 2012. Advances in the testing of hydro-mechanical behaviour of shales. In: Multiphysical Testing of Soils and Shales (Ed. by Laloui, L. & Ferrari, A.). Springer Series in Geomechanics and Geoengineering, 57-68.

IAEGHG, May 2011. Caprock systems for CO_2 geological storage.

Experimental assessment of geomechanics of deep carbon dioxide sequestration

Report #2 (January - December 2015)

R.Y. Makhnenko, D. Mylnikov, and L. Laloui

Soil Mechanics Laboratory - Chair "Gaz Naturel" Petrosvibri, École Polytechnique Fédérale de Lausanne

Overview

The research group at the Soil Mechanics Laboratory – Chair “Gaz Naturel” Petrosvibri at the EPFL deals with characterization of thermo-chemo-hydro-mechanical behavior of possible host and caprocks for geologic carbon dioxide sequestration in contact with *in-situ* water and liquid and supercritical CO_2. This report briefly describes the scientific activities of the group in 2015.

Scope of the research

Deep saline aquifers have the greatest potential for geological storage of CO_2 and due to their worldwide occurrence can play a major role in reduction of carbon dioxide emissions. CO_2 is usually injected in liquid state and, in sedimentary basins at depths below 800 meters, it transfers to the supercritical condition ($scCO_2$), which means that its temperature and pressure are above 31.1^o C and 7.4 MPa. Carbon dioxide then can dissolve in the *in-situ* fluids and be trapped stratigraphically under the low permeable cap rock and in pore space of the storage formation (Figure 1), as well as by reacting with minerals that form it (IAEGHG, 2011). Injected CO_2 changes the local effective stresses and temperatures and chemically reacts with the rock-forming minerals and thus can significantly deform the aquifer and the surrounding media. Therefore, for the proper assessment of safe geological storage, thermo-hydro-chemo-mechanical characterization of possible host and caprock material is needed.

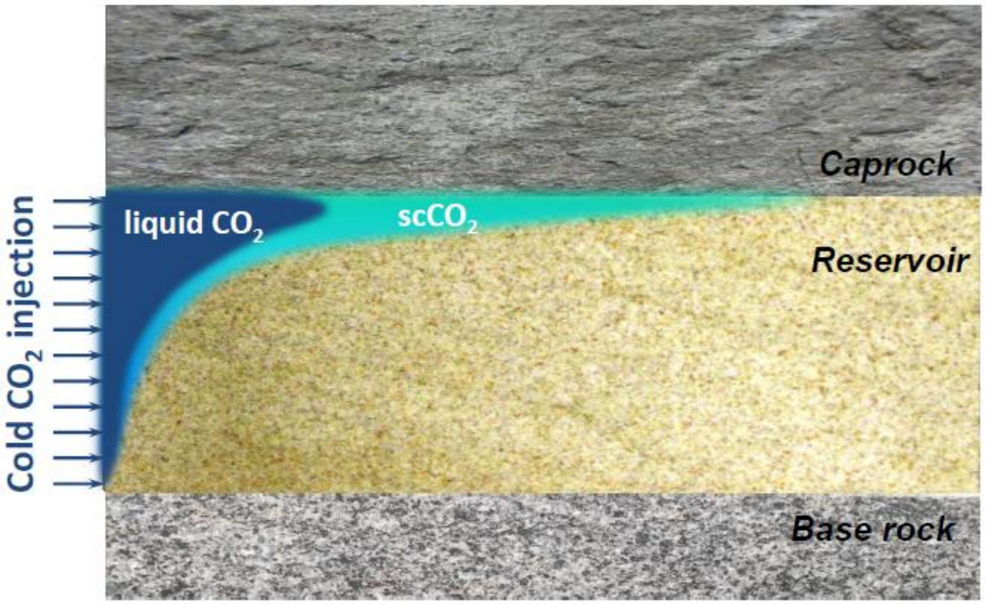

Figure 1: Sketch of CO_2 injection in reservoir rock and its trapping under caprock formation.

This report describes laboratory experiments performed on representatives of high-permeable quartz-rich reservoir material and low-permeable clay-rich caprock. Oedometric mechanical loading representing *in-situ* conditions at 1 km depth was applied and liquid and supercritical CO_2 was injected in water-saturated rocks to study their flow properties.

Experimental methods

Cylindrical specimens (height h = 12.5 mm diameter D = 35 mm) of rock were prepared and loaded in oedometric cell, which imposes zero lateral strain condition (Figure 2). Rock was fully-saturated with distilled or *in-situ* water, respectively in case of high-permeable or low-permeable material. Full saturation was ensured by applying relatively high back pressures (> 8 MPa) and measuring constant values of Skempton's B coefficient while keeping the effective stress unchanged (Makhnenko and Labuz, 2015). Axial stress was the control parameter and it was applied in a way that effective mean stress P' would be approximately equal to 6 MPa in all the experiments. CO_2 and CO_2-rich water injection tests were performed at pressure p^f = 10 MPa and two different temperatures: 20 °C and 39 °C, which correspond to liquid and supercritical carbon dioxide phases, respectively. The effective permeability for i-th phase - k_i^{eff} was calculated from knowledge of fluids viscosity μ_i and measurements of volume outflow ΔV_i as function of time Δt:

$$k_i^{eff} = \frac{4 \cdot \Delta V_i \cdot \mu_i \cdot h}{\pi \cdot \Delta t \cdot D^2 \cdot \Delta p^f} \tag{1}$$

The relative permeability for i-th phase is

$$k_i^{rel} = \frac{k_i^{eff}}{k_{abs}}, \tag{2}$$

where k_{abs} is the absolute kinematic permeability of rock.

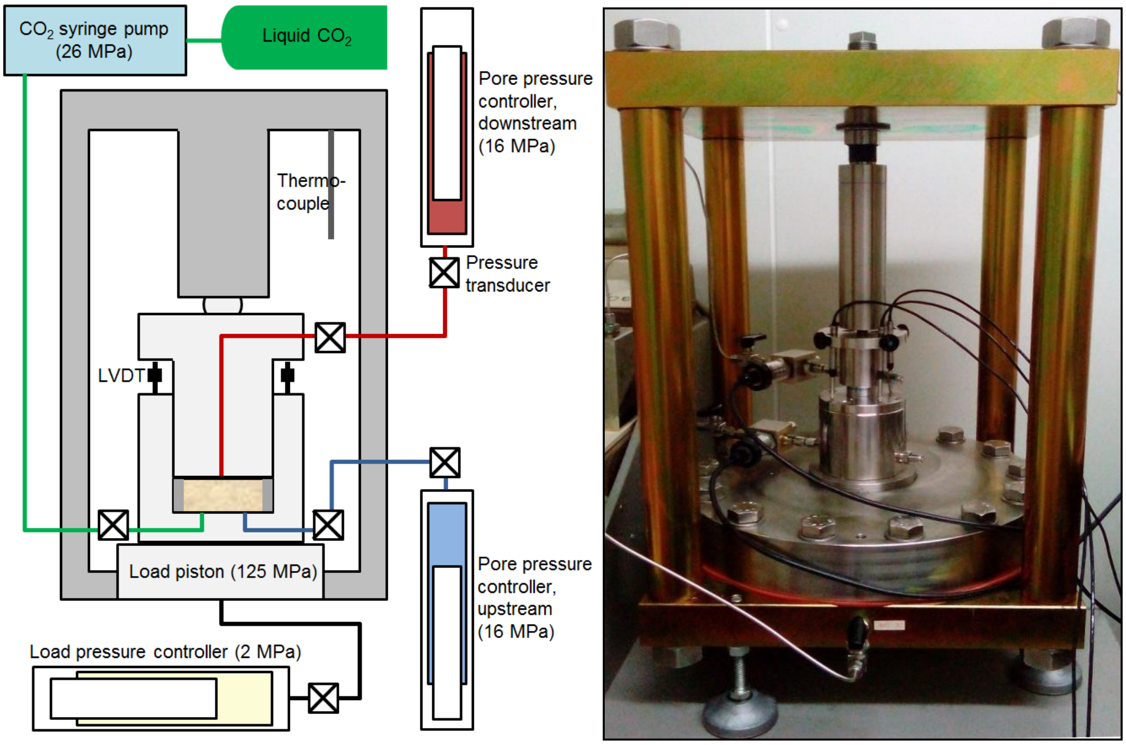

Figure 2: Sketch (a) and (b) photo of the oedometric cell setup at LMS-EPFL, which allows studying flow and mechanical properties of rock saturated with brine and high-pressure CO_2.

Research achievements

1) Host rock

Berea sandstone - quartz-rich rock with 23% porosity, 6 · 10^{-14} m^2 permeability, and 20 µm dominant pore diameter was considered as a representative of high-permeable reservoir material. The relative permeability curves were obtained for liquid (20 °C) and supercritical CO_2 (39 °C). Residual water saturation after CO_2 flow reached the steady-state condition was evaluated from measurements of Skempton's *B* coefficient, which reflects the compressibility of pore fluid. For the case of maximum CO_2 saturation, relative permeability of liquid CO_2 was found to be 20% larger than the one at supercritical state (Figure 3). Measured relative CO_2 permeabilities for liquid and supercritical phases are within the reported ranges for rocks with absolute permeabilities higher than 50 · 10^{-14} m^2 (Burnside and Naylor, 2014):

$$k_{CO_2}^{rel} = 0.05 \div 0.20 \tag{3}$$

Thus far, it was found that CO_2 injection does not affect mechanical properties of the quartz-rich rock. However, this statement has to be tested for longer time periods and at elevated pressures.

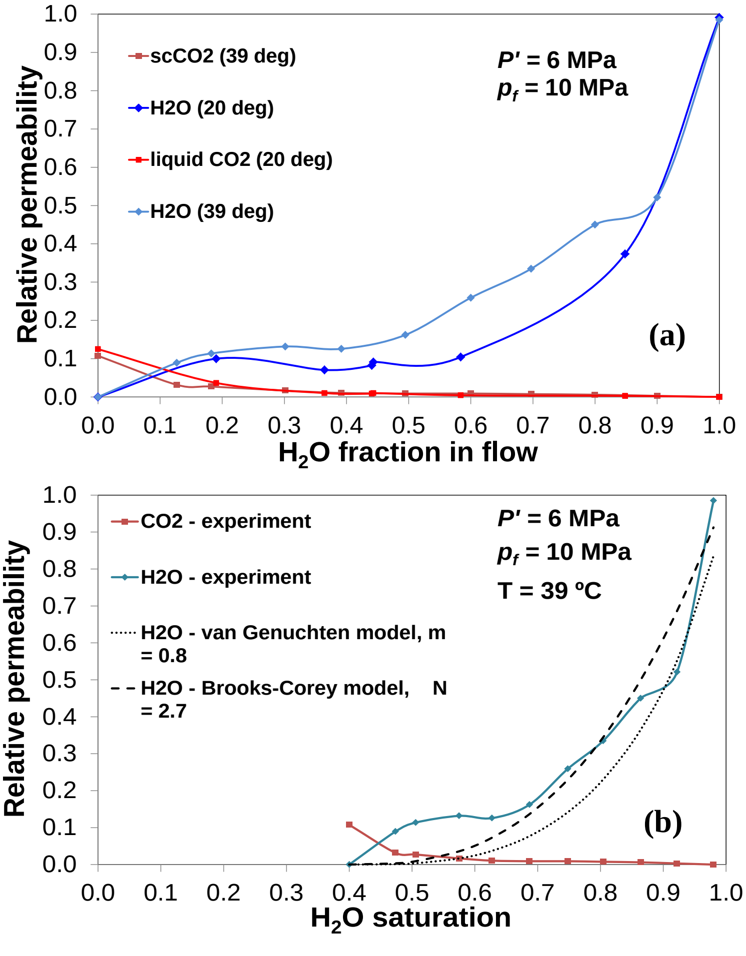

Figure 3: (a) Relative permeability of H_2O and CO_2 at 20˚C and 39˚C vs H_2O fraction in flow and (b) relative permeability of H_2O and $scCO_2$ vs H_2O saturation and fitting with different models.

Slightly different curves were obtained for relative permeability of water at different temperatures and the results are fitted with two different models. Brooks and Corey (1964) predict:

$$k_w^{rel} = \left(S_w^*\right)^{N_w} \tag{4}$$

where saturation parameter S_w*:

$$S_w^* = \frac{S_w - S_w^{res}}{1 - S_w^{res}} \tag{5}$$

Parameter N_w was calculated to be 2.7 at 39 °C and 4.2 at 20 °C.

Van Genuchten (1980) assumes:

$$k_w^{rel} = \sqrt{S_w^*}\left\{1 - \left(1 - \left[S_w^*\right]^{1/m}\right)^m\right\}^2 \tag{6}$$

Van Genuchten *m*-parameter gives the best fit for *m* = 0.80 at 39 °C and *m* = 0.78 at 20 °C. Both models do not capture observed local increase in relative water permeability at S_{H_2O} = 0.6, so it has to be explored further.

2) Caprock

In this study, Opalinus clay (shaly facies) from Mont Terri is used as a representative of a possible caprock for geological storage of carbon dioxide in Switzerland. Absolute permeability of intact Opalinus formation is on the order of 10^{-20} m^2, which imposes difficulties for injecting non-wetting fluid in the sample. Thus, prior to intact rock, a sample of remolded Opalinus clay with permeability equal to $1.5 \cdot 10^{-18}$ m^2 at *in-situ* conditions (σ_1 = 21 MPa, $\sigma_3 \approx$ 14 MPa) was chosen to investigate how injected CO_2 affects caprock properties.

Clay-rich sample was saturated with artificial pore water prepared in accordance with studies of pore fluid geochemistry at the Mont Terri Rock Laboratory (Pearson et al., 2003). Then CO_2 injection in the sample started at pore pressure of 10 MPa and 21 °C and the pore pressure gradient of 125 kPa was applied at the first stage (Figure 4). It was found that effective CO_2 permeability was not constant during the flow process. Moreover, oscillations in permeability were clearly related to changes in ratio of input and outflow. Observed difference in amounts of liquid that was entering and leaving the sample leads to assumption of chemical interactions between sample minerals and pore fluid, which was strongly acidified by CO_2. Chemical reactions inside the pores could lead to changes in sample structure and composition, which resulted in observed permeability oscillations possibly caused by competing processes of mineral dissolution and precipitation.

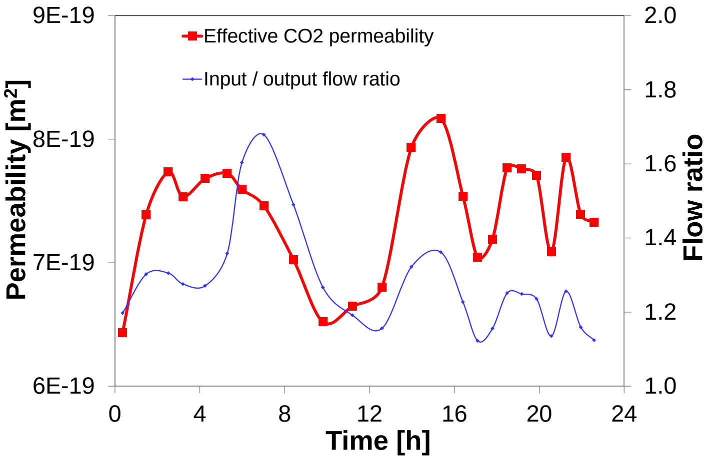

Figure 4. CO_2 flow through the clay sample at 125 kPa pressure difference: permeability and ratio of input and output flow rates.

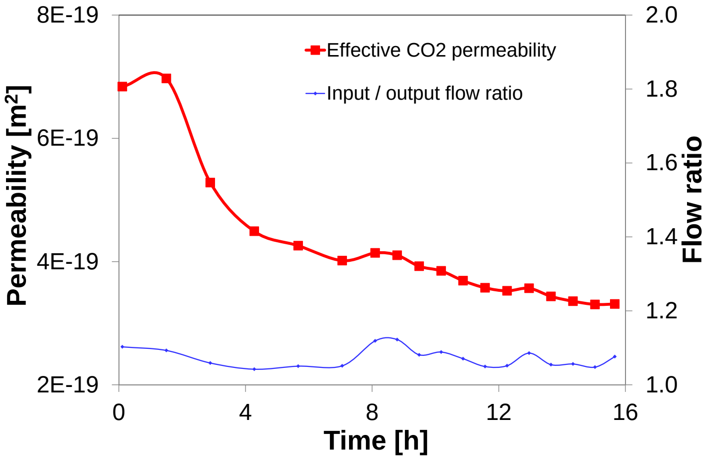

Figure 5. CO_2 flow through the clay sample at 620 kPa pressure difference: permeability and ratio of input and output flow rates.

When the pore pressure difference across the sample was increased to 620 kPa, oscillations of effective CO_2 permeability stopped (Figure 5). Permeability monotonically decreased by factor of two suggesting mineral precipitation in the pore space and reached an approximately constant value. The ratio of input and output flow rates was approximately equal to unity, indicating much lower intensity of chemical interactions between rock matrix and pore fluid.

Stiffness of the sample was estimated through oedometric modulus measurements at different stages of the experiment. After CO_2 flow at 620 kPa pressure gradient, sample demonstrated stiffness two times higher than that after flow at 125 kPa. It is essential now to study structure and composition changes of clay-rich material sample at micro-level. This will lead to an explanation of changes in macro-parameters, such as material's permeability and stiffness.

Future work on host and caprock – carbon dioxide interaction

The proposed research for 2016 deals with the following aspects of CO_2–rock interaction:

- measurements of permeability of reservoir rock including calcite-rich material with respect to brine-CO_2 mixtures at high pressure gradients and different temperatures (below and above 31.1 °C)
- characterization of effect of CO_2 injection on mechanical properties of reservoir rock, both quartz-rich and calcite-rich;
- assessment of the poromechanical properties and strength parameters of clay-rich materials, including shale, before carbon dioxide injection;
- measuring permeability of low-permeable (~ 10^{-18} m^2 and lower) clay-rich material including shale with respect to brine-CO_2 mixtures;
- characterization of changes in hydro-mechanical properties of low-permeable clay-rich formations caused by CO_2 injection at different temperatures;
- investigation of the chemical effect of injected CO_2 on low-permeable caprock representatives, including changes of microstructure, porosity, and chemical composition of the tested specimens studied with Scanning Electron Microscopy, Mercury Intrusion Porosimetry, and Bio-Chemical analysis.

References:

van Genuchten, M.T., 1980. Soil Sci. Soc. Am. J., 44: 892-898

Burnside, N.M. and M. Naylor, 2014. Int. J. of Greenhouse Gas Control, 23: 1-11.

Brooks, R.H. and A.T. Corey, 1964. Civ. Eng. Dep., Colorado State Univ., Fort Collins, Colo.

IAEGHG, May 2011. Caprock systems for CO_2 geological storage.

Makhnenko, R. and J. Labuz, 2015. J. Geophys. Res. Solid Earth, 120: 909-922.

Pearson, F.J. et al, 2003. Bern, Switzerland, SNHGS, Geological Report, No. 5.

Appendix B

Conference abstracts and posters

Effect of liquid and supercritical CO_2 injection on petrophysical properties of rock

Roman Makhnenko*, Danila Mylnikov* & Lyesse Laloui*

* Soil Mechanics Laboratory - Chair "Gaz Naturel" Petrosvibri, École Polytechnique Fédérale de Lausanne, EPFL ENAC IIC LMS, GC – Station 18, CH-1015 Lausanne (roman.makhnenko@epfl.ch)

Deep saline aquifers have the greatest potential for geological storage of CO_2 and due to their worldwide occurrence can play a major role in reduction of carbon dioxide emissions. CO_2 is usually injected in liquid state and, in sedimentary basins at depths below 800 meters, it transfers to the supercritical condition ($scCO_2$), which means that its temperature and pressure are above 31.1^o C and 7.4 MPa. Carbon dioxide then can dissolve in the *in-situ* fluids and be trapped stratigraphically under the low permeable cap rock and in pore space of the storage formation, as well as by reacting with minerals that form it. Injected CO_2 changes the local effective stresses and temperatures and thus can significantly deform the aquifer and the surrounding media. Therefore, for the proper assessment of safe geologic storage, thermo-hydro-mechanical characterization of possible host and caprock material is needed.

Sandstone reservoirs, which mostly are high-permeable single-porosity systems, are usually considered as a host rock material. Berea sandstone - quartz-rich rock with 23% porosity and 60 mD permeability was fully saturated with water and its poroelastic parameters were measured. Then, liquid (20°C) and supercritical CO_2 (40°C) were injected at 10 MPa pressure and their relative permeability curves were obtained. Residual water saturation after CO_2 flow reached the steady-state condition was evaluated from measurements of Skempton's *B* coefficient, which reflects the compressibility of pore fluid. Relative permeability of liquid CO_2 was found to be 20% larger than the one at supercritical state and both of them are within the reported trends for high-permeable rocks. Thus far, it was found that CO_2 injection does not affect mechanical properties of the quartz-rich rock. However, this statement has to be tested for longer time periods and at elevated pressures.

Furthermore, Opalinus clay is considered to be a representative of the clay-rich caprock material for carbon dioxide storage. Analysis of the poromechanical behavior of the low-permeable shale is critical for anticipation and prevention of its failure and calculation of in-situ effective stresses, thus the preliminary characterization of the poroelastic effect was performed. Laboratory experiments indicated that the chemical effect of CO_2 dissolving in pore water of the caprock dominates at the early stages of injection and delays the mechanical effect of high pressure carbon dioxide desaturating the pores of shale and propagating through it. The chemical effect of high pressure CO_2 - pore fluid mixture on the mechanical properties of caprock is currently under consideration.

Thermo-hydro-mechanical aspects of caprock – CO_2 interaction for safe geological storage

Roman Makhnenko*, Danila Mylnikov*, Victor Vilarrasa*,** & Lyesse Laloui*

* Soil Mechanics Laboratory - Chair "Gaz Naturel" Petrosvibri, École Polytechnique Fédérale de Lausanne, EPFL ENAC IIC LMS, GC – Station 18, CH-1015 Lausanne (roman.makhnenko@epfl.ch)
** Institute of Environmental Assessment and Water Research, Spanish National Research Council (IDAEA-CSIC), Jordi Girona 18-26, 08034 Barcelona, Spain

Security of carbon dioxide (CO_2) geological storage largely depends on the caprock integrity, especially at the early stages after the start of injection when the maximum overpressure is reached. The lower boundary of the caprock is in contact with CO_2 saturated pore water or pore fluid that consists almost of pure CO_2. Thermal and chemical interactions between the pore fluid and the caprock may change the material properties of the latter. Geomechanical stability is also crucial to maintain the caprock sealing capacity, since failure could lead to permeability increase and potentially induced microseismicity. Considering clay-rich materials (e.g., shales) as potential caprock has several advantages, including thermal, chemical, and inelastic deformations of the clay-rich (ductile) formation minimizing the affection on the sealing integrity as the upward movement of CO_2 through their pore system should be resisted by high capillary pressure.

Opalinus clay (Swiss shale) is studied as a representative caprock material because of its high (~ 60%) clay content and very small dominant pore size (~ 30 nm). Poromechanical properties of the shale are analysed by performing drained, undrained, and unjacketed conventional triaxial tests. Thermo-mechanical response is studied in drained and undrained heating and cooling experiments. It is shown that a potential shallow (~ 1 km) storage case with cold CO_2 injection leading to caprock cooling by 15 ˚C (from 40 ˚C to 25 ˚C) neither compromises shale intergrity nor deteriorates its mechanical properties.

The breakthrough pressure values and effective permeability of liquid and supercritical CO_2 are measured for intact and reconstituted shale brought to in situ conditions in the oedometric cell. Breakthrough pressure is found to be effective stress-dependent and smaller for the intact material rather than for the reconstituted one (1.5 MPa and 4 MPa, respectively, at 18 MPa effective stress). This non-intuitive observation is explained by a non-uniform structure of the undisturbed material where CO_2 can find a path with larger than dominant pore sizes to flow through. CO_2 effective permeability of brine-saturated shale is an order of magnitude smaller than the one for brine and is on the order of 10^{-21} m^2 for the intact and reconstituted material loaded to in situ conditions.

Shales show interesting self-sealing features and their ductile-type failure allows often times to retain very small permeability. Since creep may become significant when assessing the long-term caprock integrity, viscous (time-dependent) deformation should be considered. The effective viscosity of Opalinus clay was found to be on the order of 10^{15} Pa•s, decreasing with temperature, and droping to 10^{13} Pa•s in region where the pore fluid pressure gets closer to the total stress, which increases the probability of porosity waves creation.

SCCER SoE
SWISS COMPETENCE CENTER for ENERGY RESEARCH
SUPPLY of ELECTRICITY

Swiss Competence Center on Supply of Electricity
Annual Conference 2015

In cooperation with the CTI
Energy
Swiss Competence Centers for Energy Research
Schweizerische Eidgenossenschaft
Confédération suisse
Confederazione Svizzera
Confederaziun svizra

Swiss Confederation

Commission for Technology and Innovation CTI

Impact of liquid and supercritical CO_2 injection on host rock properties

Roman Makhnenko, Danila Mylnikov, and Lyesse Laloui
Soil Mechanics Laboratory – chair «Gaz Naturel» Petrosvibri, École Polytechnique Fédérale de Lausanne

1. Introduction

Research of the chair "Gaz Naturel" – Petrosvibri at the EPFL contributes to SCCER-SoE task 1.2: "Reservoir modelling and validation". Both numerical modeling and experimental investigation of geomechanical processes involved in deep geological storage of CO_2 are performed in cooperation with government agencies: SFOE and Swisstopo. Proper assessment of carbon dioxide storage procedure allows to significantly reduce its concentration in the atmosphere and thus directly contributes to Swiss energy strategy 2050.

Deep saline aquifers have the greatest potential for geological storage of carbon dioxide and due to their worldwide occurrence can play a major role in reduction of carbon dioxide emissions. Injected CO_2 changes the local effective stresses and temperatures and thus can significantly deform the aquifer and the surrounding media. Sandstone reservoirs, which mostly are high-permeable single-porosity systems, are usually considered as a host rock material. The ongoing experimental investigations involve conventional triaxial and oedometric tests, where carbon dioxide is injected in water-saturated host rock material at different temperatures and pressures. This poster presents the current findings on CO_2 saturation and flow in sandstone.

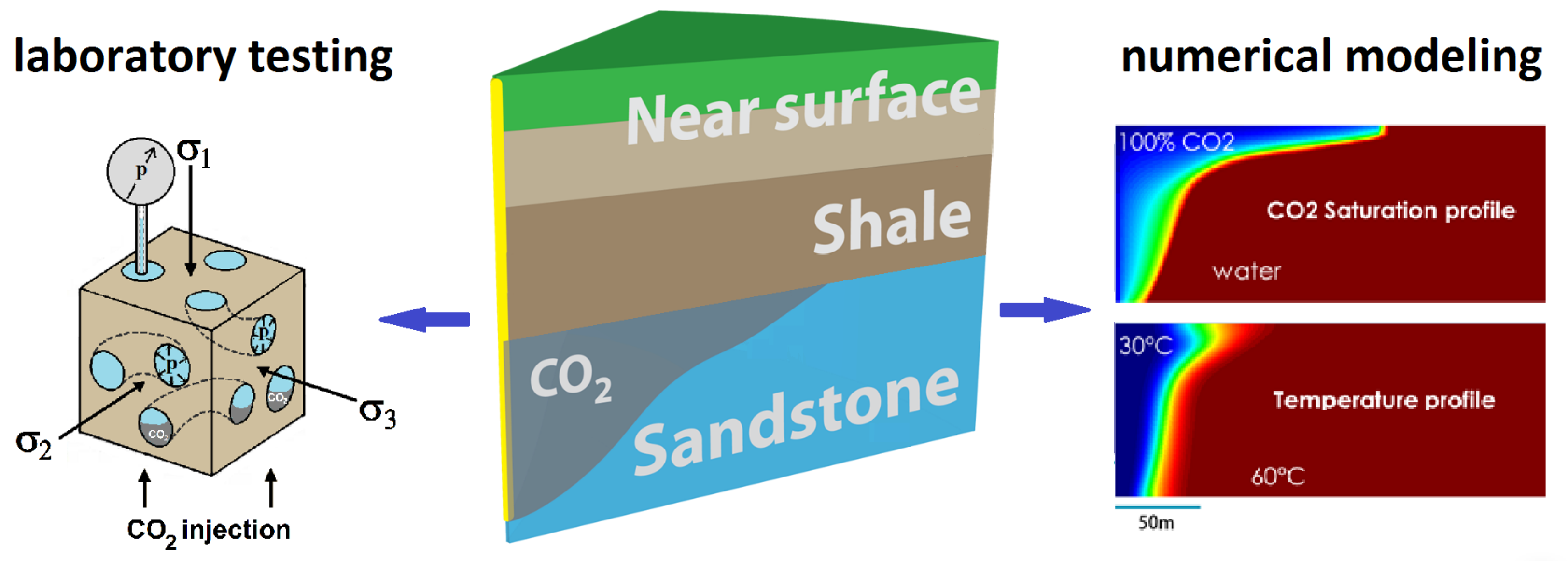

Fig. 1: Sketch of the research activities on geologic CO_2 sequestration.

2. Background and methods

CO_2 is usually injected in liquid state and, in sedimentary basins at depths below 800 meters, it changes its phase to supercritical fluid ($scCO_2$), which means that its temperature and pressure are above 31.1º C and 7.4 MPa. Carbon dioxide then can dissolve in the *in-situ* fluids and be trapped stratigraphically under the low permeable cap rock and in pore space of the storage formation, as well as by reacting with minerals that form it.

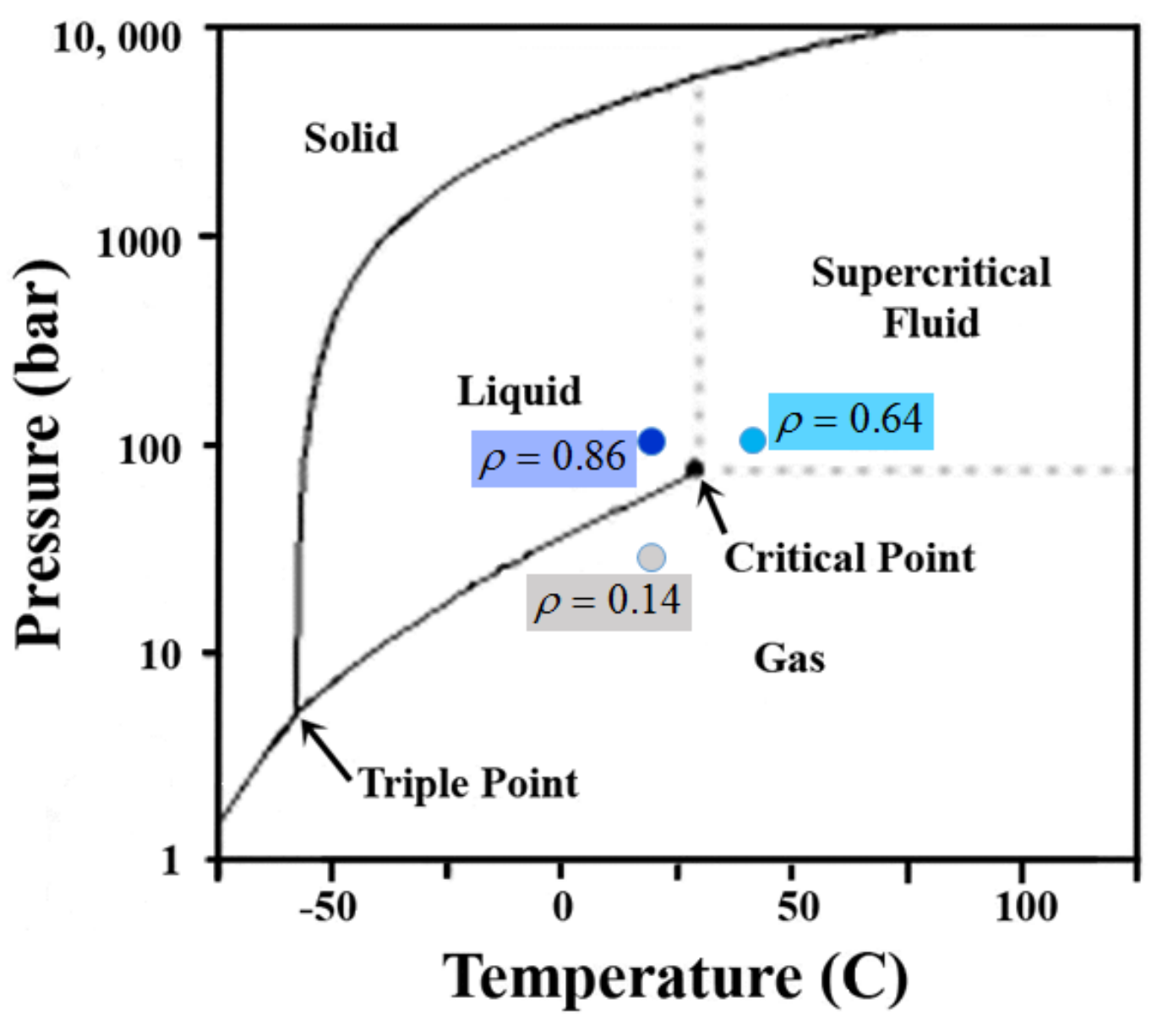

Fig. 2: CO_2 phase diagram.

CO_2 and CO_2-rich water injection tests were performed on cylindrical specimens (height h = 12.5 mm diameter D = 35 mm) loaded in oedometric cell (zero lateral strain). Liquid (20°C) and supercritical CO_2 (39°C) were injected at pressure p_f = 10 MPa and effective mean stress P' = 6 MPa. The effective permeability for i-th phase was calculated from knowledge of fluids viscosity μ_i and measurements of volume outflow ΔV_i per time Δt:

$$k_i^{eff} = \frac{4 \cdot \Delta V_i \cdot \mu_i \cdot h}{\pi \cdot \Delta t \cdot D^2 \cdot \Delta p_f}$$

The relative permeability for i-th phase is

$$k_i^{rel} = \frac{k_i^{eff}}{k_{abs}},$$

where k_{abs} is the absolute kinematic permeability of rock.

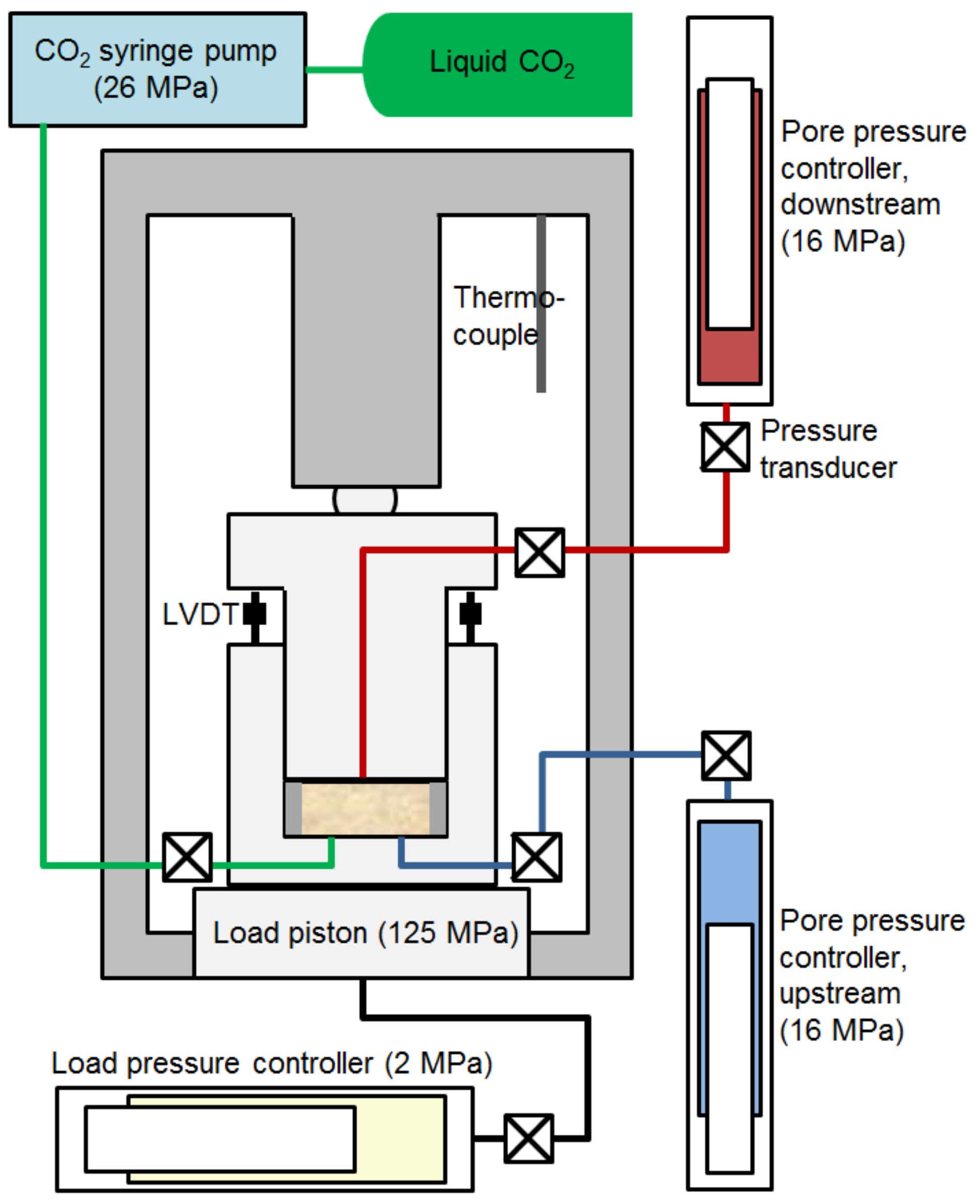

Fig. 3: Experimental setup: oedometric cell.

3. Results and Discussion

Berea sandstone is quartz-rich rock with 23% porosity, 60 mD permeability, and 20 mm dominant pore diameter. The rock was fully saturated with water at p_f = 10 MPa and its poroelastic parameters (Makhnenko and Labuz, 2015) and permeability at different temperatures (Figure 5) were measured.

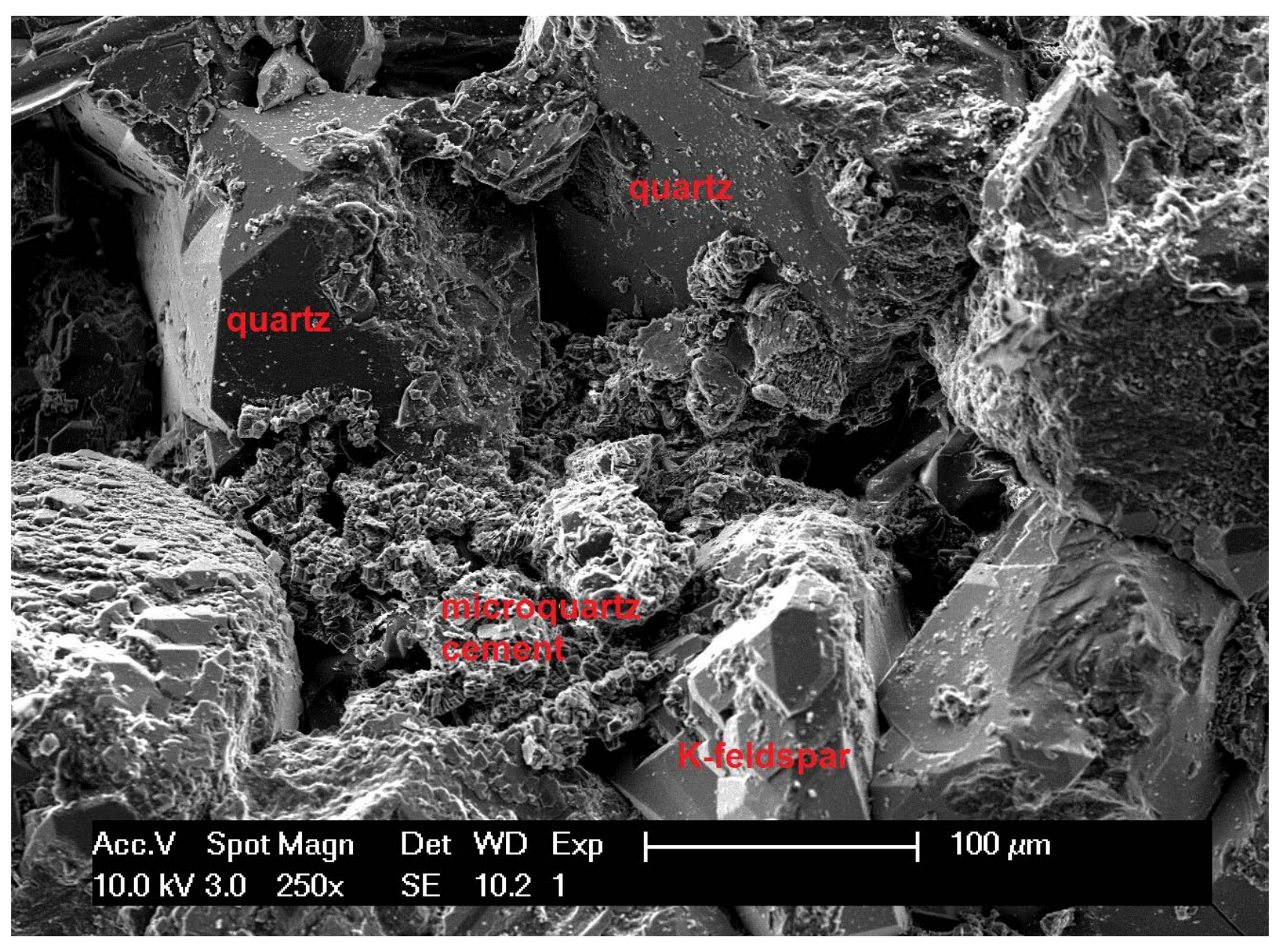

Fig. 4: Microphotograph of Berea sandstone.

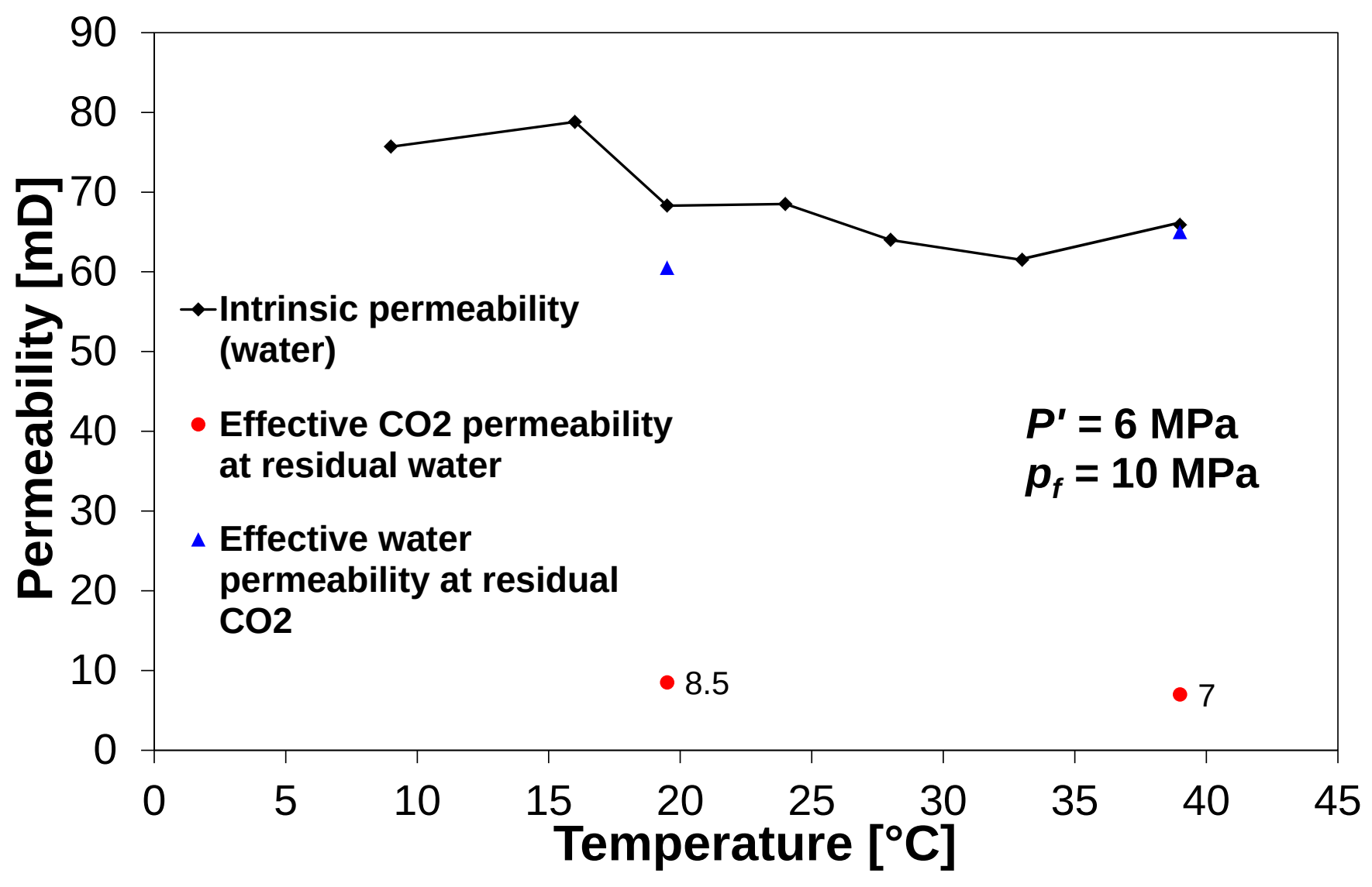

Fig. 5: Water and CO_2 permeability of water-saturated sandstone at different temperatures.

Then CO_2 and CO_2-rich water were injected and residual water saturation after CO_2 flow reached the steady-state condition was evaluated from measurements of Skempton's B coefficient, which reflects the compressibility of pore fluid. Relative permeability of liquid CO_2 was found to be 20% larger than the one at supercritical state and both of them are within the reported trends for high-permeable rocks. Slightly different curves were obtained for relative permeability of water at different temperatures and the results are fitted with two different models.

Brooks and Corey (1964) predict:

$$k_w^{rel} = \left(S_w^*\right)^{N_w}$$

where saturation parameter S_w*:

$$S_w^* = \frac{S_w - S_w^{res}}{1 - S_w^{res}}$$

Van Genuchten (1980) assumes:

$$k_w^{rel} = \sqrt{S_w^*}\left\{1-\left(1-\left[S_w^*\right]^{1/m}\right)^m\right\}^2$$

Parameter N_w was calculated to be 2.7 at 39°C and 4.2 at 20°C. Van Genuchten m-parameter gives the best fit for m = 0.80 at 39°C and m = 0.78 at 20°C. Both models do not capture observed local increase in relative water permeability at S_{H_2O} = 0.6, so it has to be explored further.

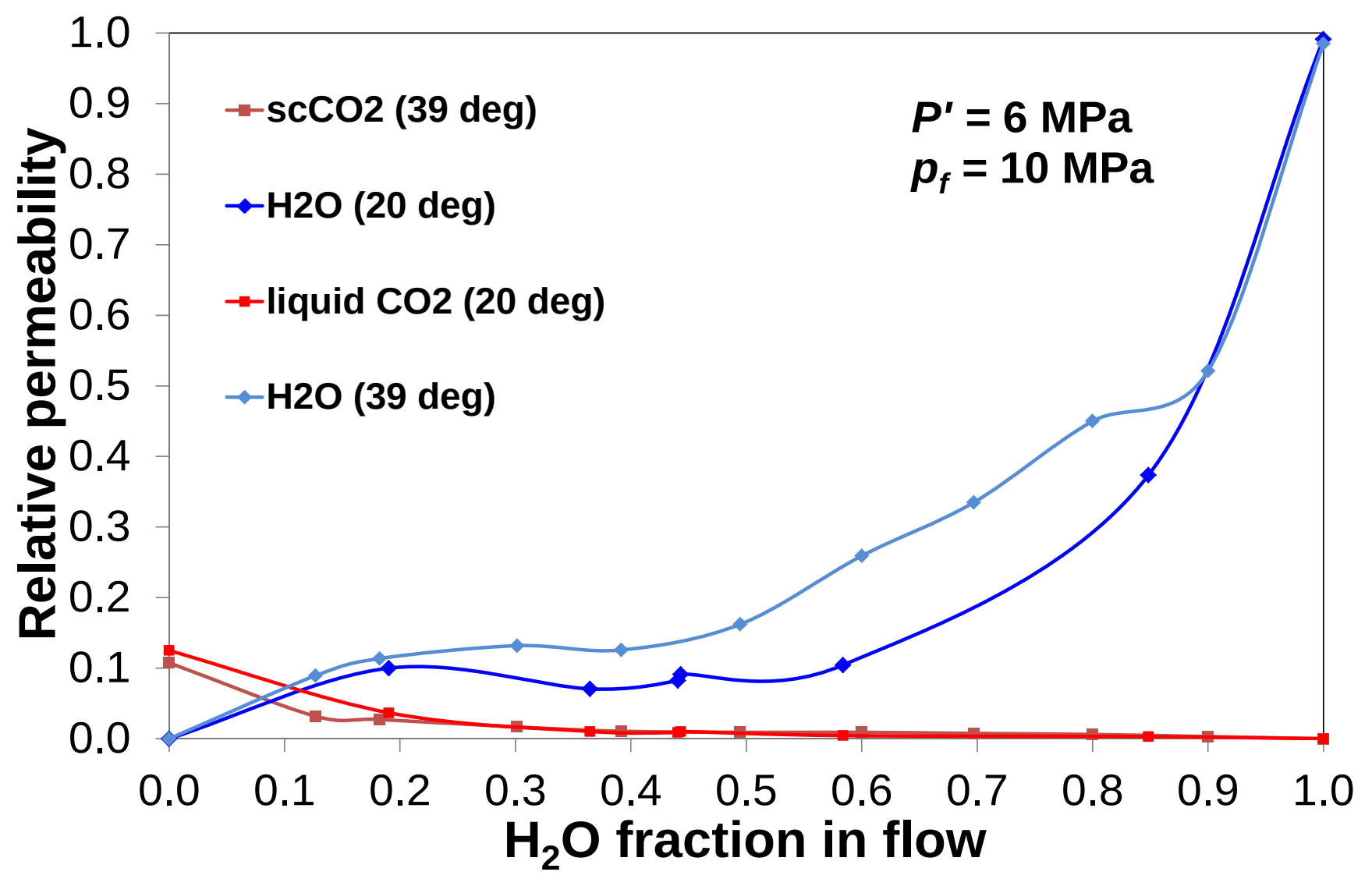

Fig. 6: Relative permeability of H_2O and CO_2 at 20˚C and 39˚C vs H_2O fraction in flow.

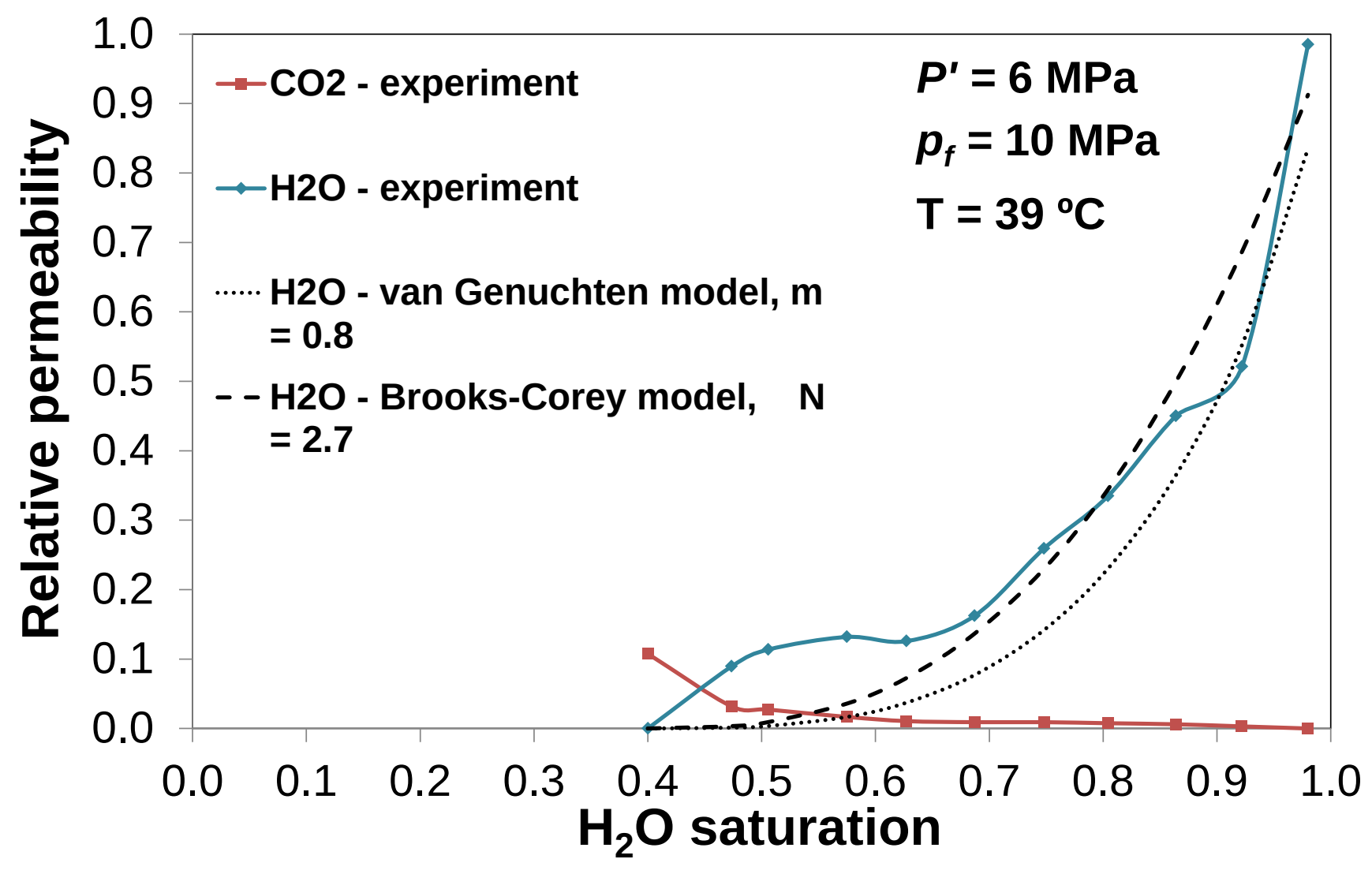

Fig. 7: Relative permeability of H_2O and $scCO_2$ and fitting with different models.

4. Conclusions

In order to study the host rock behavior during deep geological carbon dioxide storage, CO_2 and CO_2-rich water were pressurized to 10 Mpa and injected in water-saturated sandstone at 20°C and 39°C. Relative permeability of liquid CO_2 (20°C) was found to be 20% larger than the one at supercritical state (39°C) and both of them are within the reported trends for high-permeable rocks. Changes in mechanical properties of rock due to CO_2 injection are currently under consideration.

Acknowledgements

R. Makhnenko activities are sponsored by SCCER-SoE (Switzerland) grant and Swiss Federal Office of Energy (SFOE) project CAPROCK #810008154. D. Terzis performed microimaging analysis.

References

Brooks, R.H. and A.T. Corey, 1964. Civ. Eng. Dep., Colorado State Univ., Foort Collins, Colo.
Makhnenko, R. and J. Labuz, 2015. J. Geophys. Res. Solid Earth, 120: 909-922.
van Genuchten, M.T., 1980. Soil Sci. Soc. Am. J., 44: 892-898.

SCCER-SoE Annual Conference 2016

SCCER SoE
SWISS COMPETENCE CENTER for ENERGY RESEARCH
SUPPLY of ELECTRICITY

In cooperation with the CTI
Energy
Swiss Competence Centers for Energy Research
Schweizerische Eidgenossenschaft
Confédération suisse
Confederazione Svizzera
Confederaziun svizra
Swiss Confederation
Commission for Technology and Innovation CTI

Hydromechanical aspects of CO_2 breakthrough and flow in clay-rich caprock

Roman Makhnenko, Danila Mylnikov, Victor Vilarrasa, and Lyesse Laloui
Soil Mechanics Laboratory – chair «Gaz Naturel» Petrosvibri, École Polytechnique Fédérale de Lausanne

1. Introduction

Research of the chair “Gaz Naturel” – Petrosvibri at the EPFL contributes to SCCER-SoE task 1.2: “Reservoir modelling and validation“. Both numerical modeling and experimental investigation of geomechanical processes involved in deep geological storage of CO_2 are performed in cooperation with government agencies: SFOE and Swisstopo. Proper assessment of carbon dioxide storage procedure allows to significantly reduce its concentration in the atmosphere and thus directly contributes to Swiss energy strategy 2050.

Deep saline aquifers have the greatest potential for geological storage of carbon dioxide and due to their worldwide occurrence can play a major role in reduction of carbon dioxide emissions. Injected CO_2 changes the local effective stresses and temperatures and thus can significantly deform the involved rock. One of the issues is the caprock integrity or possible CO_2 propagation through the rock layers overlying the reservoir formation. The ongoing experimental investigations involve oedometric tests, where carbon dioxide is injected in brine-saturated clay-rich caprock-like materials at different temperatures and pressures.

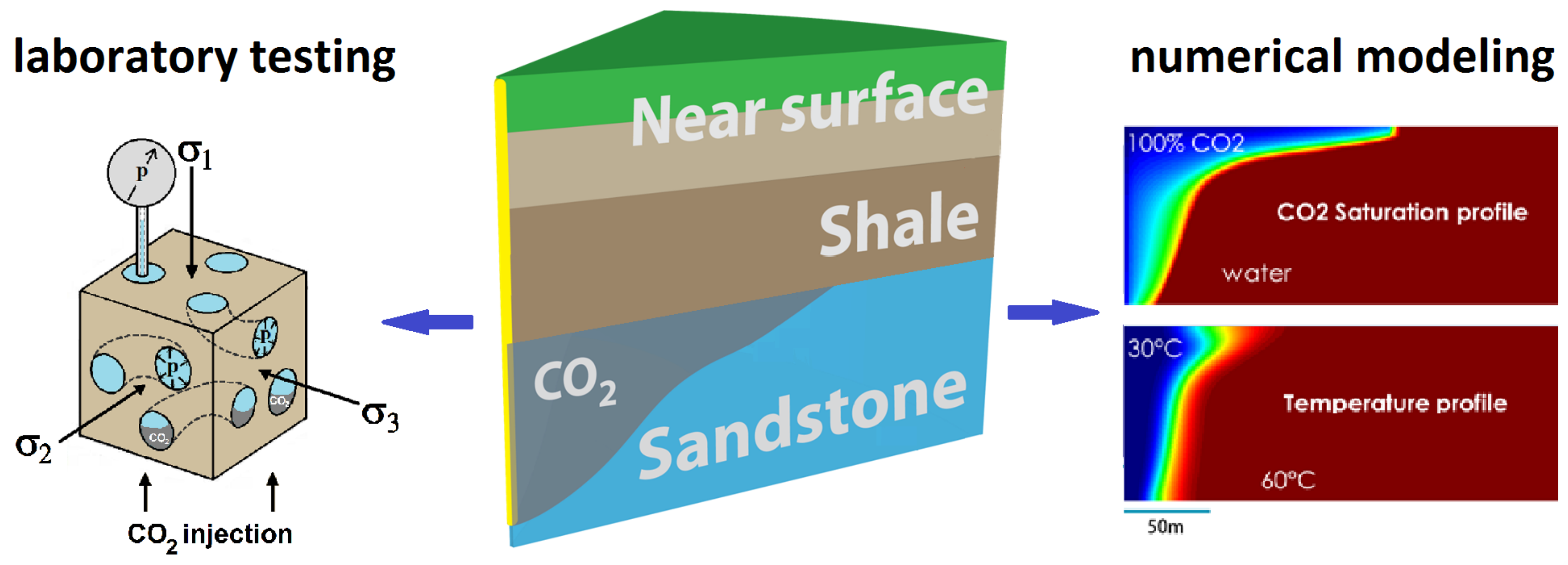

Fig. 1: Sketch of the LMS-EPFL research activities on geologic CO_2 sequestration.

2. Background and methods

CO_2 is usually injected in liquid state and, in sedimentary basins at depths below 800 meters, it changes its phase to supercritical fluid ($scCO_2$) with temperature above 31.1° C and pressure exceeding 7.4 MPa. Threshold capillary pressure p_c (Fig. 2) is an intrinsic property of each particular pore throat and for a cylinder of diameter d, γ - surface tension at the brine-CO_2 boundary and θ - contact angle of brine-CO_2 surface with respect to solid phase,

$$p_c = \max(p_{CO_2} - p_{brine}) = \frac{4\gamma\cos\theta}{d}$$

Breakthrough pressure is determined as the differential fluid pressure at which constant flow of CO_2 through the specimen was established, i.e., when CO_2 started to displace brine within the pore space.

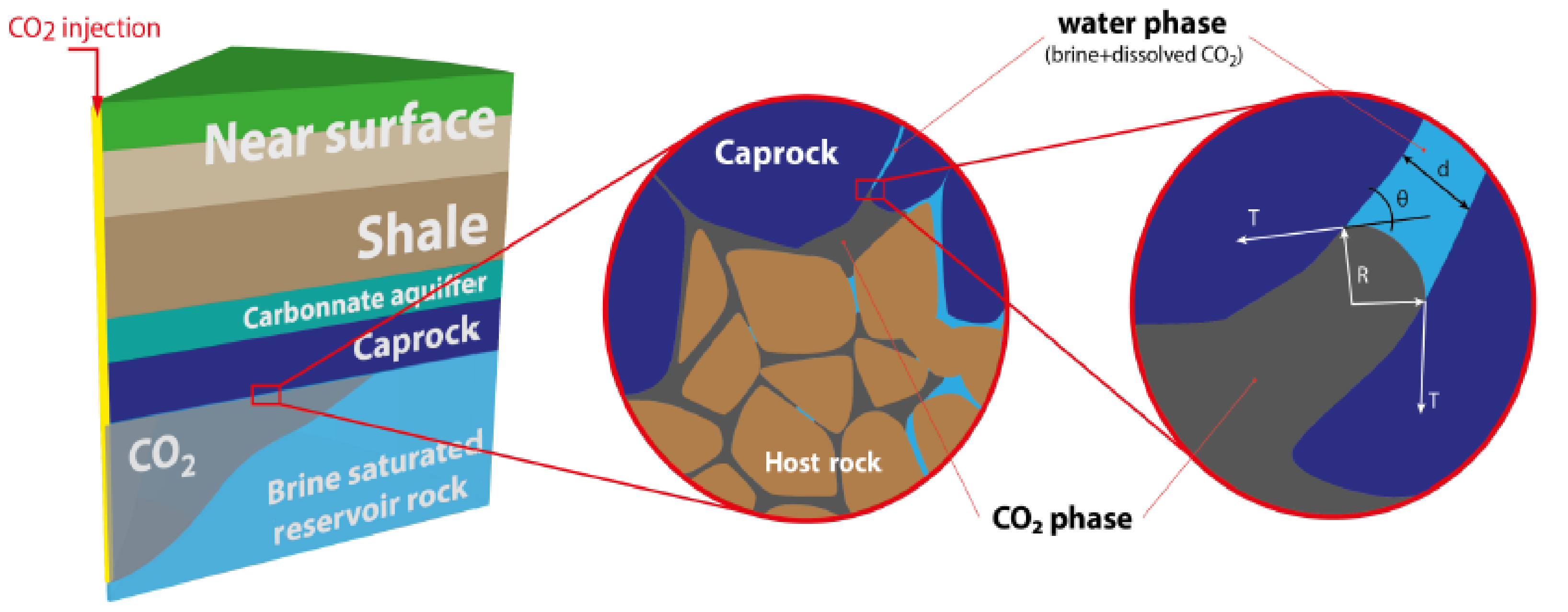

Fig. 2: Capillary effects at the reservoir-caprock interface.

CO_2 injection tests are performed on cylindrical specimens (height h = 12.5 mm diameter D = 35 mm) loaded in oedometric cell (Fig. 3). Liquid (24°C) and supercritical CO_2 (42°C) breakthrough and flow are studied in rock specimens fully saturated with brine with constant (8 MPa) downstream pressure.

After breakthrough occurs, viscous steady-state vertical Darcy flow of CO_2 through the material is assumed and effective CO_2 permeability is

$$k_{CO_2}^{eff} = \frac{4\Delta V_{CO_2}\eta_{CO_2} h}{\pi D^2 \Delta p_{diff}\Delta t}$$

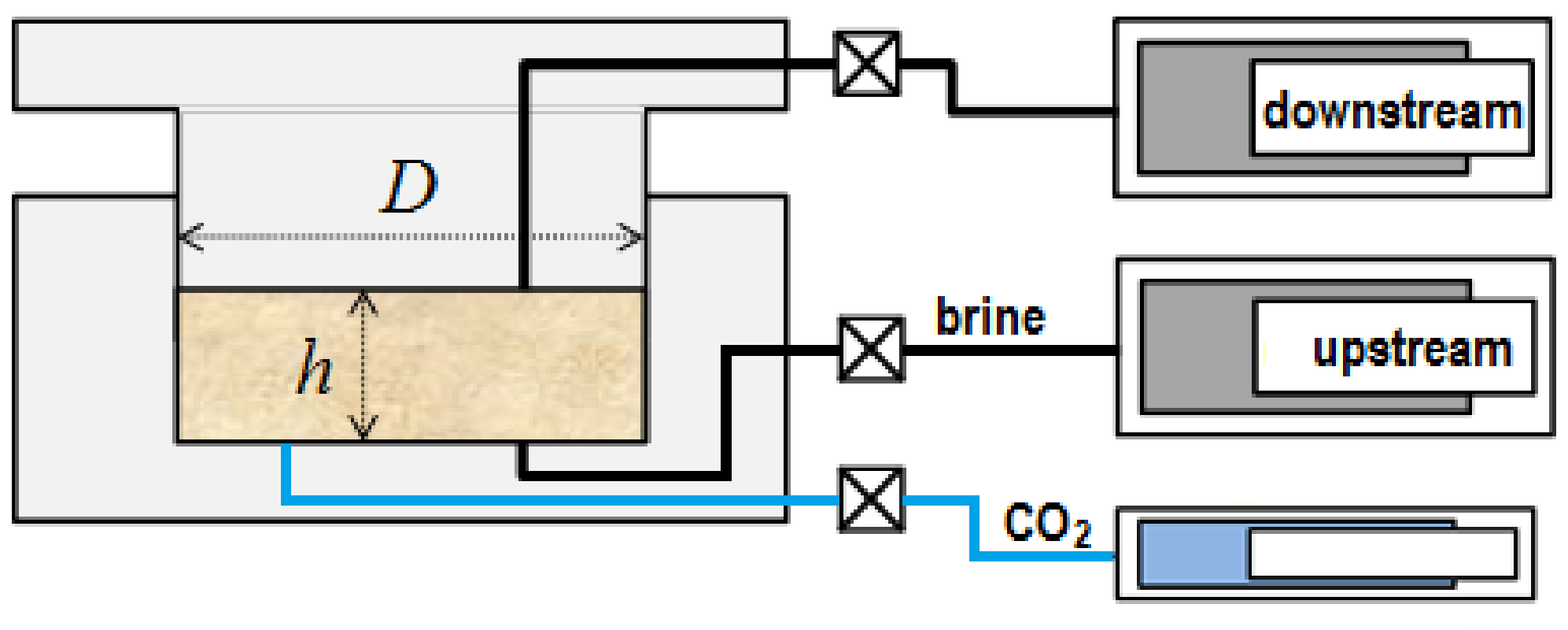

Fig. 3: Sketch of experimental setup.

3. Results and Discussion

Remolded (i. e., reconstituted) Opalinus clay specimens saturated with natural brine are tested. Loading to 35 MPa vertical stress and 8 MPa pore pressure provides full saturation and porosity of 0.13 with dominant pore throat diameter of 40 nm (Fig. 4).

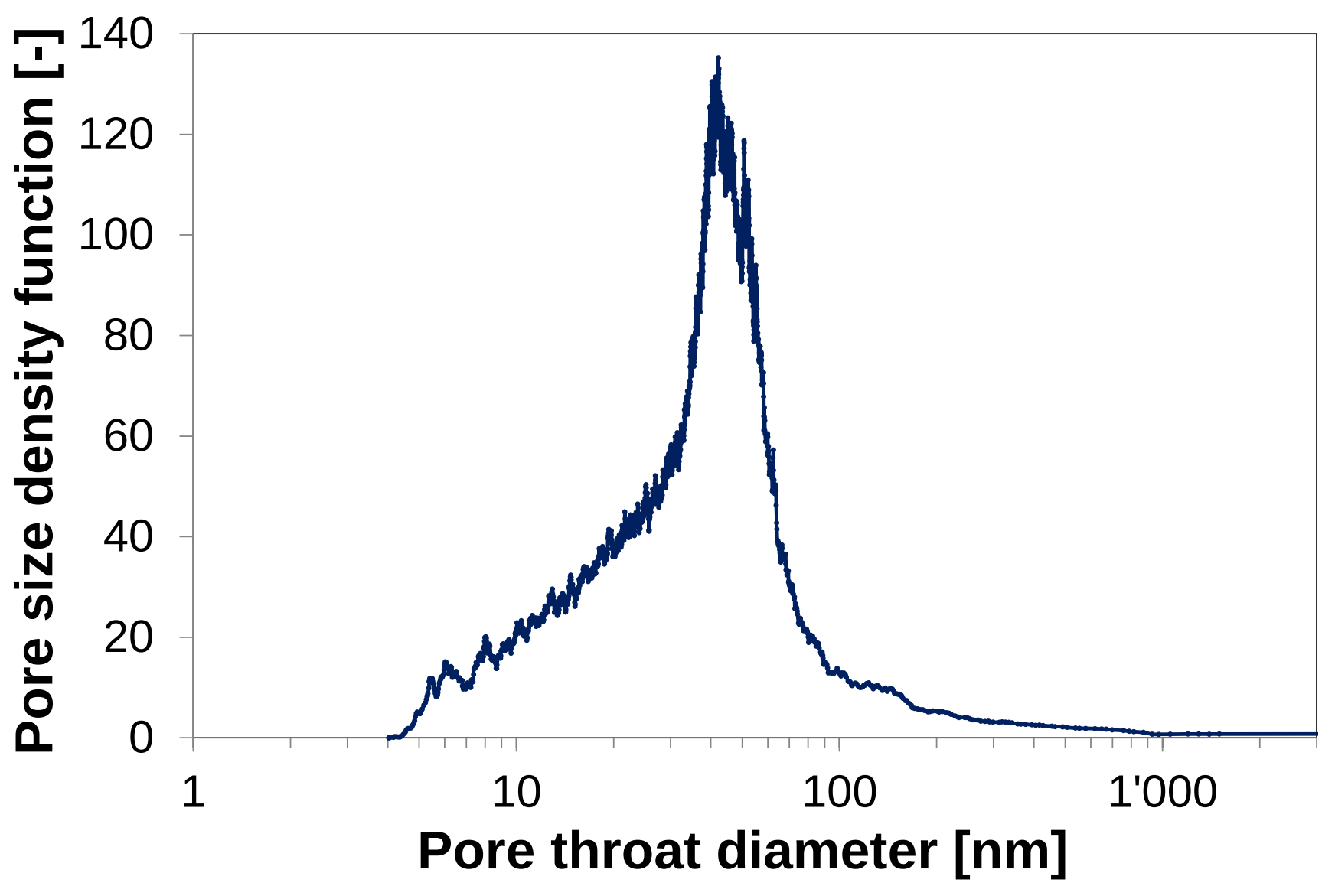

Fig. 4: Pore throat diameter distribution in remolded shale loaded to 35 MPa.

The breakthrough pressure is measured using the direct method (Fig. 5), where excess CO_2 pressure is slowly and gradually increased until continuous CO_2 flow is observed (Thomas *et al.*, 1968). At every new level of differential pressure, more CO_2 dissolves in the pore fluid, but eventual decrease of CO_2 flow rate indicates that viscous flow is not actually established. After differential pressure increases to 4.2 MPa (at 35 MPa vertical stress), CO_2 flow rate reaches a constant level of approximately 5 mm^3/ hour, hence breakthrough is reported. Also, an indirect experimental technique (Hildenbrand *et al.*, 2002) is implemented: a capillary threshold pressure is measured as the differential fluid pressure (2.8 MPa at 35 MPa vertical stress in Fig. 6) when CO_2 stops flowing through the specimen after its injection is finished. CO_2 breakthrough pressure increases with effective mean stress, which is related to compression of the pores and reduction in pore throat diameters. Relationship between direct and indirect methods is to be analyzed further since the latter one usually provides smaller p_c values.

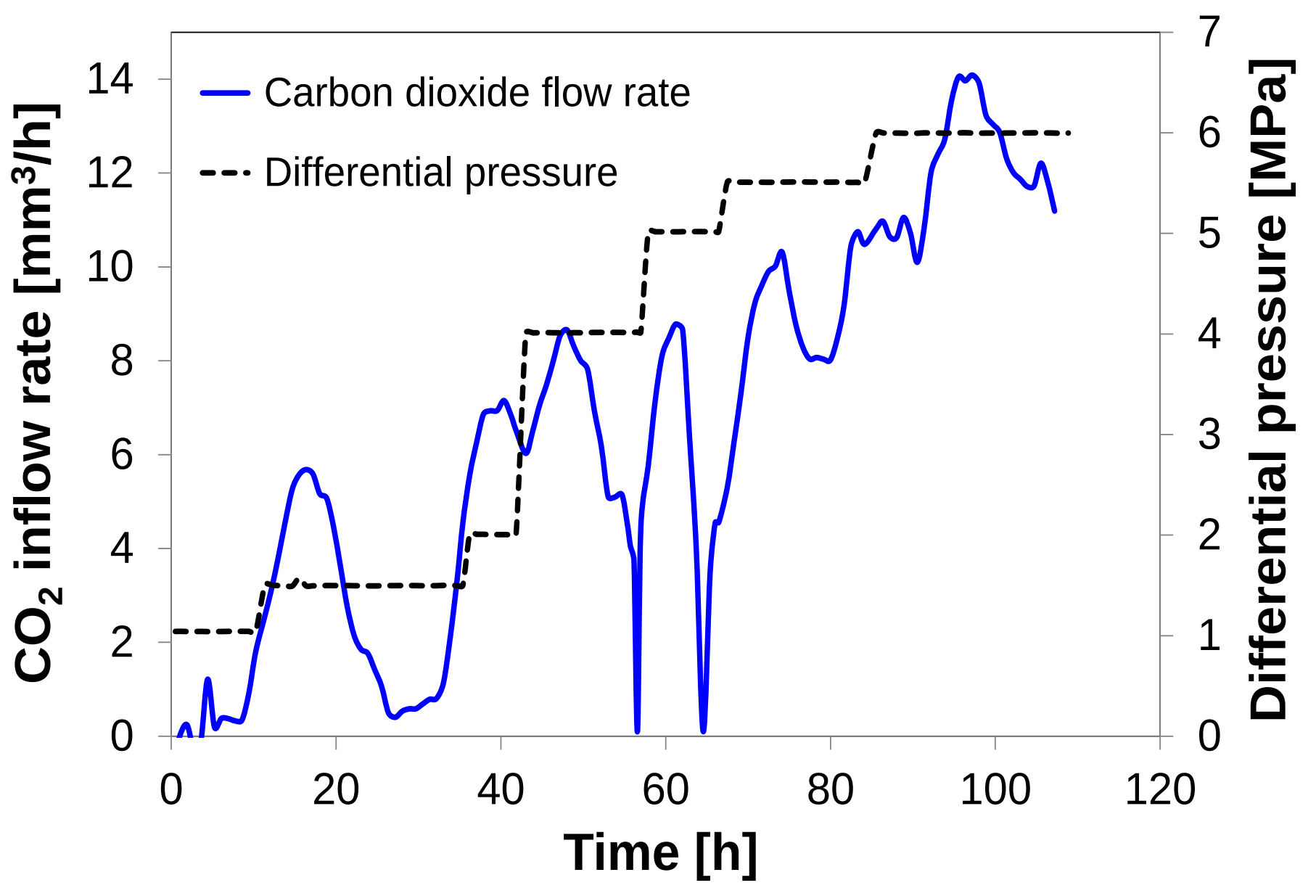

Fig. 5: CO_2 breakthrough pressure measurements using the direct method.

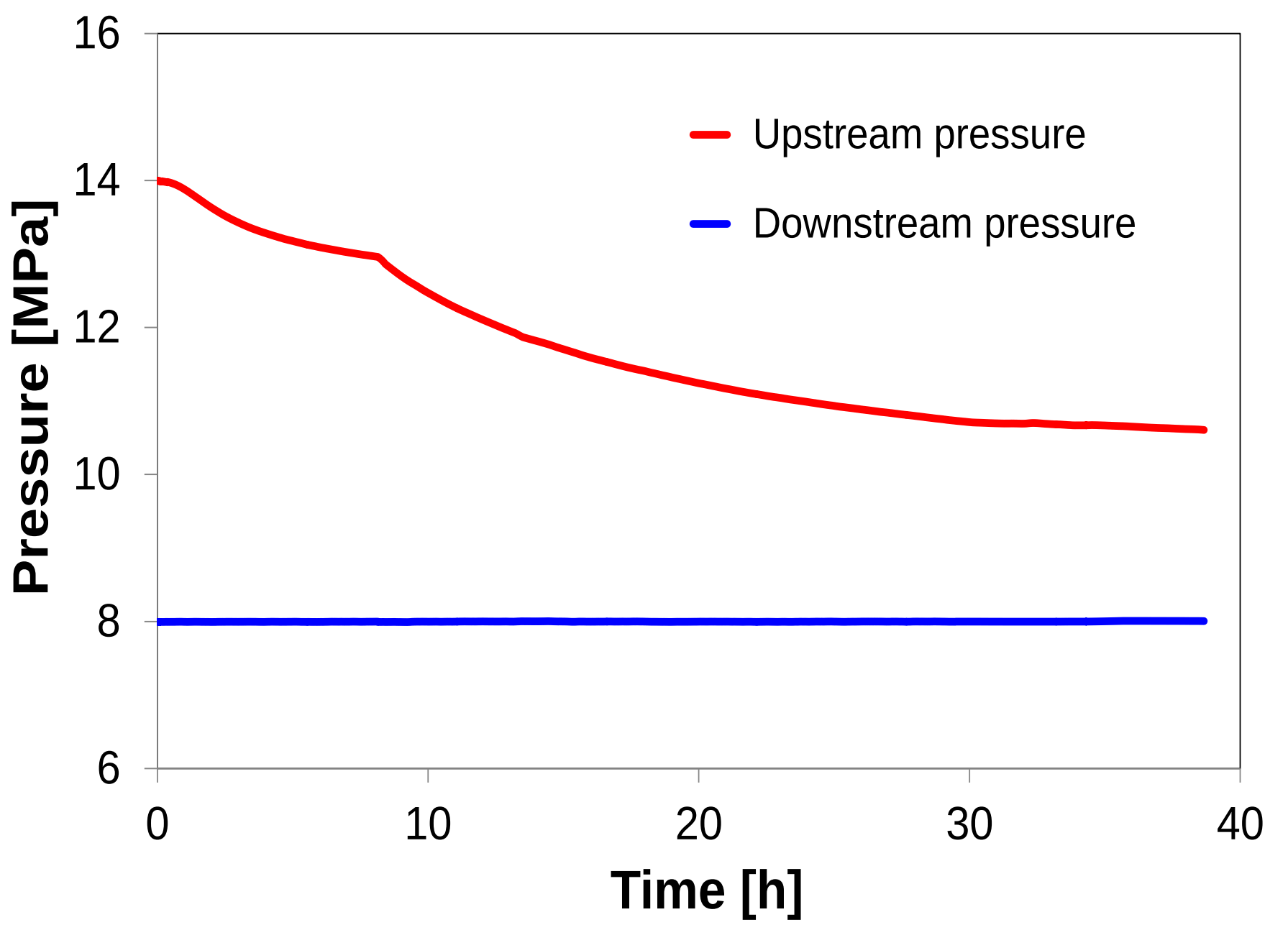

Fig. 6: Results of CO_2 breakthrough pressure measurements by the indirect method.

CO_2 effective permeability decreases with effective mean stress (Fig. 7) and increases with differential pressure because of the capillary effects: the higher the pressure – the larger is the amount of pores that participate to non-wetting fluid flow.

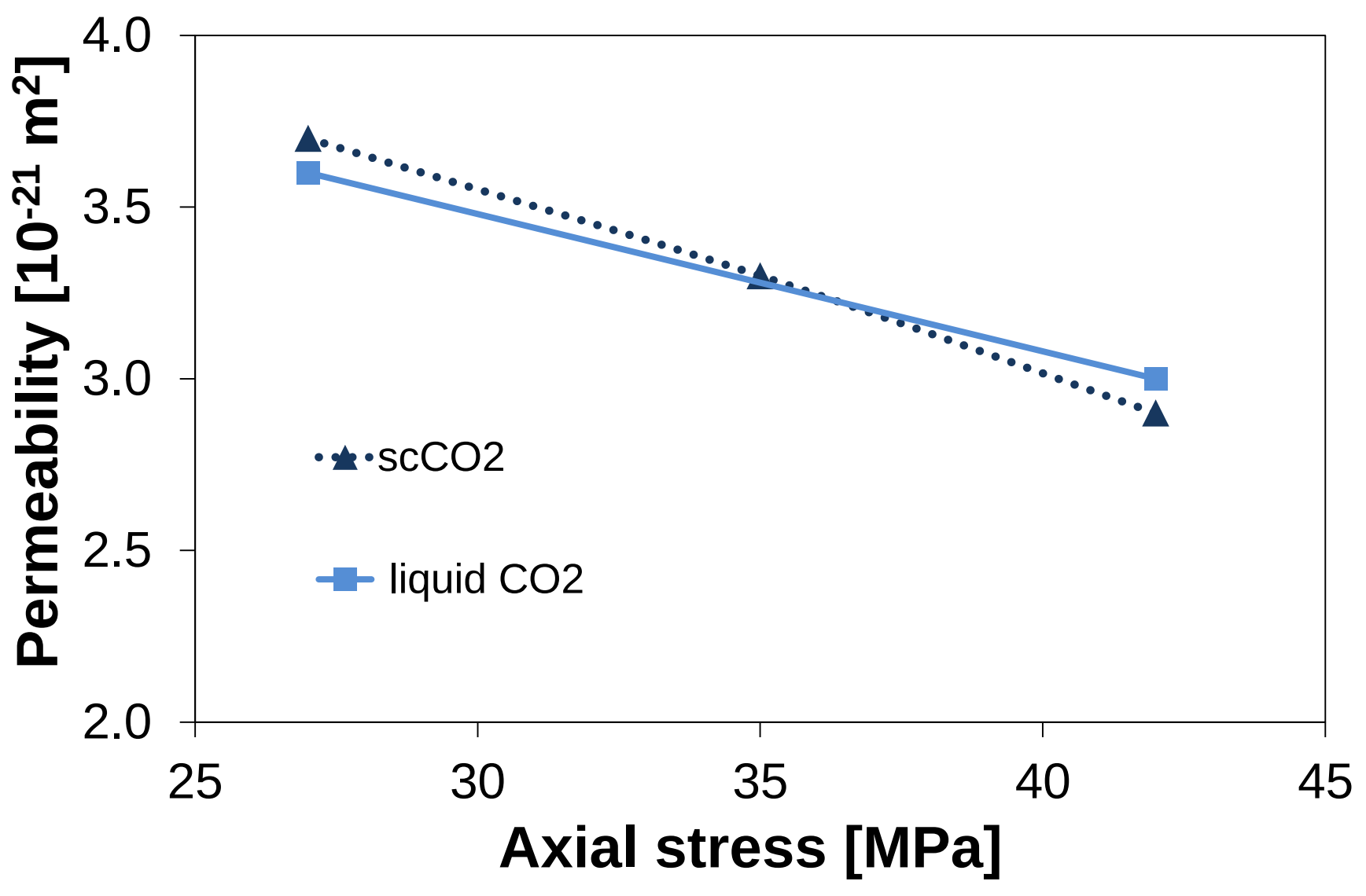

Fig. 7: Liquid and $scCO_2$ permeabilities of remolded shale vs applied axial stress.

4. Conclusions

In order to study the caprock behavior during deep geological carbon dioxide storage, liquid and supercritical CO_2 were injected in brine-saturated clay-rich material at 24°C and 42°C. CO_2 breakthrough pressure was determined to be increasing with effective mean stress and CO_2 effective permeability was observed to increase with differential fluid pressure. Preliminary studies on capillary threshold pressure show that it is usually smaller than the breakthrough pressure. The proper calculation of the latter one is of particular importance for evaluating maximum injection rates for CO_2 storage projects.

Acknowledgements

R. Makhnenko is an SCCER-SoE postdoctoral researcher. Tested shale is provided by Swisstopo and the conducted experiments are a part of SFOE sponsored project CAPROCK #810008154.

References

Hildenbrand, A., S. Schlömer, B.M Kroos, 2002. Geofluids, 2:3-23.
Thomas, L.K., D. L. Katz, M.R. Tek, 1968. SPE Journal, 243:174–184.

Appendix C

Conference papers

Tu Gme 07

Influence of Poromechanical and Thermal Properties of the Caprock on the Safety of CO2 Storage

V. Vilarrasa (Swiss Federal Institute of Technology), R.Y. Makhnenko* (Swiss Federal Institute of Technology) & L. Laloui (Swiss Federal Institute of Technology)

SUMMARY

Geologic carbon sequestration is a promising option to reduce carbon dioxide emissions to the atmosphere and mitigate climate change. The injected CO2 will reach the storage formation at a colder temperature than that of the host rock. This cold CO2 will cool down the caprock by conduction, which will induce thermal stress reduction and pressure changes that will affect caprock stability. We analyzed thermoporomechanical response of Swiss shale and found that the effective stress changes induced by cooling do not have, in general, the potential to jeopardize the caprock sealing capacity.

Introduction

Geologic carbon sequestration is considered to have enough storage capacity to safely contribute in one fifth of the total reduction in carbon dioxide (CO_2) emissions that we should carry out in the following decades to mitigate climate change (IEA, 2010). The huge amounts of CO_2 that will be injected will induce overpressure and temperature decrease. Overpressure propagates fast over long distances, thus having the potential to affect faults that may be located several kilometers away from the injection well (Birkholzer and Zhou, 2009). Furthermore, CO_2 will generally reach the storage formation at a colder temperature than that corresponding to the geothermal gradient, because CO_2 does not have enough time to thermally equilibrate with the surrounding rock as it flows downwards along the injection well (Paterson et al., 2008).

The colder CO_2 will form a cooled region around the injection well (Figure 1) that advances much behind than the desaturation front (Gor et al., 2013; Vilarrasa et al., 2014). Though CO_2 will not penetrate into the caprock due to its high entry pressure, cooling will propagate into the lower portion of the caprock by conduction. This cooling of the caprock will induce thermal stresses and may also induce pressure changes. Thus, effective stresses will change, modifying caprock stability. Maintaining the caprock integrity is important to avoid CO_2 leakage and justifies the concern that cooling could cause fracture opening and shearing in the lower portion of the caprock (Goodarzi et al., 2012; Vilarrasa et al., 2015). Here, we focus on the effective stress changes in the lower portion of the caprock induced by cooling and analyze the subsequent caprock stability.

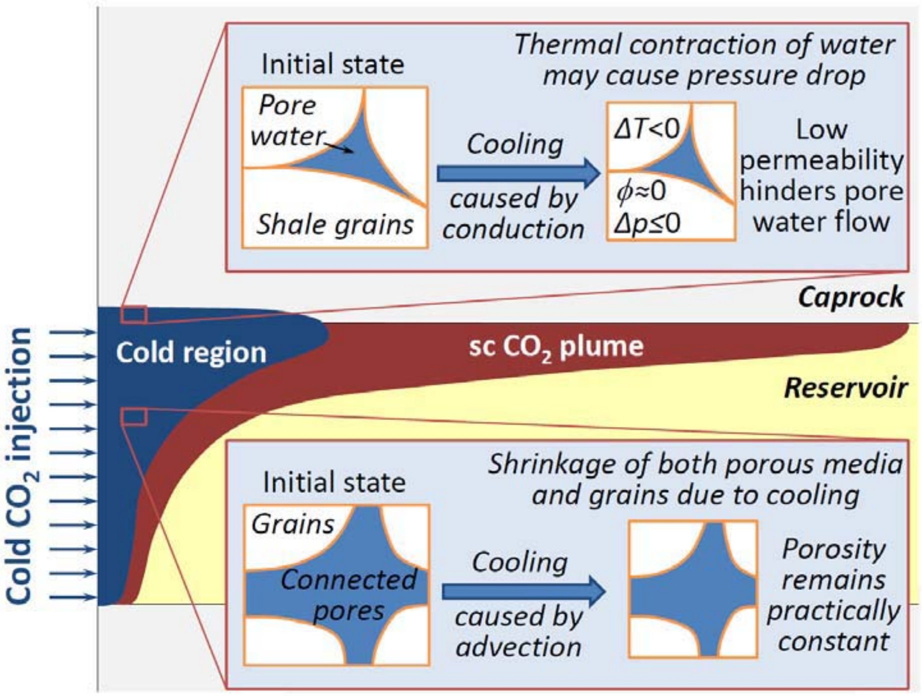

Figure 1 *Sketch of the considered geometry. Cold* CO_2 *region reaches the caprock, where contraction might cause fracturing due to effective stress changes.*

Theory

Caprock is assumed to be deforming under undrained conditions when the cold CO_2 front reaches its surface in the short-term, because the drainage processes for low-permeable formations are much longer than thermal conduction. Furthermore, pressure of CO_2 should be significantly higher (> 10 MPa) than the pore pressure in the caprock to start entering its pores. Thus, no CO_2 will be present into the caprock, so just the thermal effect on pore pressure p and vertical and horizontal stresses changes induced by the temperature difference ($d\sigma_v$ and $d\sigma_h$) acting on the caprock will be considered. Then, for an isotropic, linearly elastic material, which thermal and poroelastic parameters are assumed to be constant at the considered mean stress $P = (\sigma_v + 2\sigma_h)/3$ and temperature T ranges, the change in fluid pressure is given by

$$\frac{\beta}{BK} dp = \left(\alpha_f - \alpha_s\right) dT + \frac{\beta}{\phi K} dP \,, \tag{1}$$

where B is Skempton coefficient, K is the drained bulk modulus, and β is Biot coefficient, which are the parameters governing the poroelastic response of the caprock. The volumetric thermal expansion coefficients of the pore fluid and solid constituents of caprock are α_f and α_s, respectively (Coussy, 2004) and ϕ is the interconnected porosity. The approximate estimates for the variation of horizontal stress $d\sigma_h$ and vertical stress $d\sigma_v$ are based on the assumption that stresses vary isotropically with temperature changes and no horizontal strain is allowed at the outer boundary as a result of lateral confinement (Vilarrasa et al., 2013)

$$d\sigma_v = \alpha_d K dT \,, \tag{2}$$

$$d\sigma_h = \frac{1-2\nu}{1-\nu} dp + \alpha_d K dT \,, \tag{3}$$

where α_d is the volumetric thermal expansion coefficient of rock under drained conditions and ν is the Poisson's ratio. The decrease of temperature produces the contraction of the porous media and causes a decrease of vertical stress. The horizontal stress might increase or decrease depending on the change in pore pressure in the rock and its Poisson's ratio. Pore pressure variation though does not affect much the vertical stress, which remains largely lithostatic for the considered setup. Combining equations (2) and (3) with (1), one gets the following relationship for the undrained change in pore pressure p in the caprock as a function of the temperature change dT induced by cold CO_2 injection

$$\frac{\beta}{\phi K}\left[\frac{1}{B} - \frac{2(1-2\nu)}{3(1-\nu)}\right] dp = \left(\alpha_f - \alpha_s + \beta\frac{\alpha_d}{\phi}\right) dT \,. \tag{4}$$

Results

Swiss shale (Opalinus clay) was considered as the caprock representative for CO_2 storage. The material parameters used in this study (for P > 4 MPa) are reported in Table 1. Unjacketed bulk modulus K_s' was measured by the method proposed in Makhnenko and Labuz (2013) and drained bulk modulus was calculated by taking $B = 0.8$ as reported for effective mean stresses larger than 4 MPa by Wild et al. (2015). That allowed calculation of $\beta = 1 - K/K_s'$.

parameter	symbol	value	source
Unjacketed bulk modulus	K_s'	9 GPa	measured
Interconnected porosity	ϕ	0.12	measured
Skempton B coefficient	B	0.8	Wild et al. (2015)
Drained bulk modulus	K	2.7 GPa	calculated
Biot coefficient	β	0.7	calculated
Poisson's ratio (isotropic)	ν	0.29±0.09	Bock (2009)
Poisson's ratio (parallel to bedding planes)	ν_{II}	0.25±0.09	Bock (2009)
Volumetric thermal expansion of pore fluid	α_f	$6 \mathrm{x} 10^{-4}$ °C	Monfared et al. (2011)
Volum. thermal expansion of solid constituents	α_s	$0.3 \mathrm{x} 10^{-4}$ °C	Monfared et al. (2011)
Drained volumetric thermal expansion	α_d	$0.6 \mathrm{x} 10^{-4}$ °C	Monfared et al. (2011)

***Table 1** Material parameters of Opalinus clay.*

Due to the very limited data on the material parameters, only isotropic response is considered. However, for the case of horizontal stress (applied parallel to the bedding), Poisson's ratio for this direction – ν_{II} can be taken into account. Since the pore pressure and vertical and horizontal stresses

are changing monotonically with the Poisson's ratio, we investigate only two limiting cases for ν_{II} = (0.16, 0.34). The lower boundary of Opalinus clay that can be taken as a representative caprock lies at a depth of 950 meters and the approximate in-situ conditions are the following (Vietor et al., 2012)
σ_v = 25 MPa, σ_h = 20 MPa, p = 10 MPa, and T = 40 °C
So, σ_v can be considered as the major principal stress and σ_h is the minor principal stress.

Assuming cooling of the caprock down to 20 °C due to cold CO_2 injection, the following changes in pore pressure and horizontal and vertical stresses are predicted
1) ν_{II} = 0.16, dT = -20 °C leads to dp = -1.1 MPa, $d\sigma_v$ = -3.2 MPa, and $d\sigma_h$ = -4.3 MPa;
2) ν_{II} = 0.34, dT = -20 °C leads to dp = -0.87 MPa, $d\sigma_v$ = -3.2 MPa, and $d\sigma_h$ = -3.6 MPa.

Failure envelope for Opalinus clay at 60 °C (less conservative case in Gräsle and Plischke, 2010) and the Mohr circles for initial state and case 1 are shown in Figure 2, where $\tau = (\sigma_h - \sigma_v)/2$ and $\sigma' = -p + (\sigma_h + \sigma_v)/2$. As it can be seen, the caprock integrity is not questioned for the considered cases.

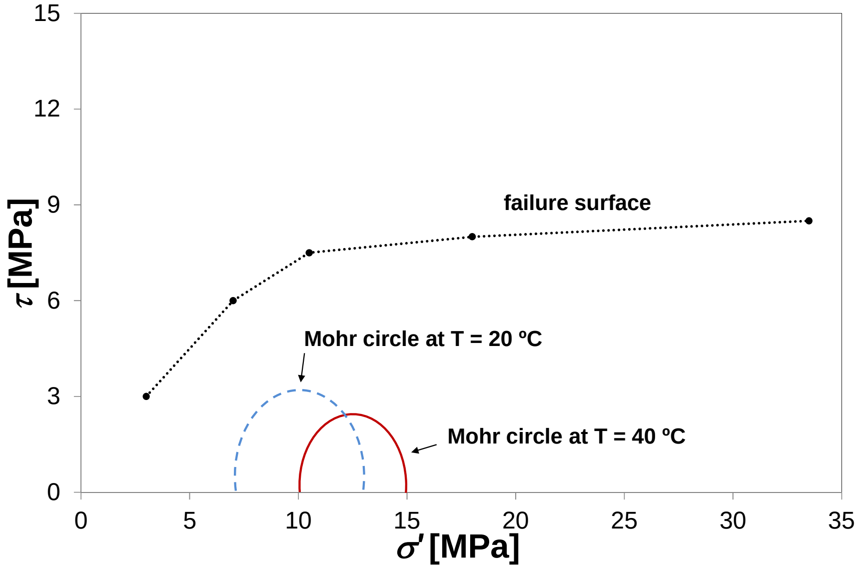

Figure 2 *Failure envelope for Opalinus clay (from Gräsle and Plischke, 2010) and Mohr circles for caprock at the initial state (40 °C, solid red circle) and after cooling to 20 °C (dashed blue circle).*

Also, for the undrained deformation, the change in caprock porosity can be calculated (Coussy, 2004)

$$d\phi = -\phi \frac{dp}{K_f} + \alpha_f \phi dT , \qquad (5)$$

where K_f is the bulk modulus of pore fluid and it can be taken as the one of pure water: K_f = 2.2 GPa. Then, for the maximum porosity change for the two cases considered above will be $d\phi = 0.4\text{x}10^{-3}$, which makes only 0.3% of the total ϕ. Clay-rich materials, like Opalinus clay might also experience poroelastoplastic deformation even for small thermally induced stresses. The contribution of plastic component will only reduce the pore pressure even more in the caprock, so the safety of the caprock is not compromised. Moreover, for undrained inelastic deformation the material might experience dilatant hardening (Makhnenko and Labuz, 2015), which will also move the Mohr circle further away from the failure surface.

Conclusions

We have analyzed the thermal effects on the caprock stability induced by cold CO_2 injection in deep saline aquifers. Cooling induces both thermal stress reduction in all directions and pressure changes induced by differences in the thermal expansion coefficient between the porous media and the pore fluid. Since the thermal expansion coefficient of the grains and that of the porous media are similar, porosity remains practically constant. Furthermore, pressure drops as a result of cooling, because the thermal expansion coefficient of the pore fluid is higher than that of the porous media. This pressure decrease improves the caprock stability, moving the stress state further away from the failure envelope. Overall, caprock stability is not compromised by cooling.

Acknowledgements

V.V. acknowledges support from the ‘EPFL Fellows’ fellowship programme co-funded by Marie Curie, FP7 Grant agreement no. 291771. R.M. would like to thank the Swiss Competence Center for Energy Research - Supply of Electricity (SCCER-SoE, grant KTI.2013.288) and Swiss Federal Office of Energy (SFOE) for the partial support.

References

Birkholzer, J. T. and Q. Zhou [2009] Basin-scale hydrogeologic impacts of CO_2 storage: Capacity and regulatory implications. *International Journal of Greenhouse Gas Control*, **3**, 745-756.

Bock, H. [2009] RA experiment - updated review of the rock mechanics properties of the Opalinus clay of the Mont Terri URL based on laboratory and field testing. *Mont Terri Tech. Report 2008-04*.

Coussy, O. [2004] *Poromechanics*. Wiley, New Jersey.

Goodarzi, S., A. Settari, and D. Keith [2012] Geomechanical modeling for CO_2 storage in Nisku aquifer in Wabamun lake area in Canada. *International Journal of Greenhouse Gas Control*, **10**, 113-122.

Gor, Y.G., T.R. Elliot, and J.H. Prévost [2013] Effects of thermal stresses on caprock integrity during CO_2 storage. *International Journal of Greenhouse Gas Control,* **12**, 300-309.

IEA [2010] *Energy technology perspectives. Scenarios & strategies to 2050. Executive summary.* International Energy Agency.

Gräsle, W. and I. Plischke [2010] LT Experiment: Mechanical Behavior of Opalinus Clay, Final report from Phases 6–14. *Mont Terri Tech. Report TR 2009-07.*

Makhnenko, R. and J. Labuz [2013] Unjacketed bulk compressibility of sandstone in laboratory experiments. *Poromechanics V - Proceedings of the 5th Biot Conference on Poromechanics*, 481-488.

Makhnenko, R.Y. and J.F. Labuz [2015] Dilatant hardening of fluid-saturated sandstone. *J. Geophys. Res. Solid Earth*, **120**, 909-922.

Monfared, M., J. Sulem, P. Delage, and M. Mohajerani [2011] A laboratory investigation on thermal properties of the Opalinus claystone. *Rock Mechanics Rock Engineering*, **44**(6), 735-747.

Paterson, L., Lu, M., Connell, L.D. and Ennis-King, J. [2008] Numerical modeling of pressure and temperature profiles including phase transitions in carbon dioxide wells. *SPE Annual Technical Conference and Exhibition,* Denver, USA, 21-24 September 2008.

Vietor, T., H. Müller, B. Frieg, and G. Klee [2012] Stress measurements in the geothermal well Schlattingen, Northern Switzerland. *Geomechanik-Kolloquium*, Freiberg, 16 November 2012.

Vilarrasa, V., O. Silva, J. Carrera, and S. Olivella [2013] Liquid CO_2 injection for geological storage in deep saline aquifers. *International Journal of Greenhouse Gas Control*, **14**, 84-96.

Vilarrasa, V., Olivella, S., Carrera, J. and J. Rutqvist [2014] Long term impacts of cold CO_2 injection on the caprock integrity. *International Journal of Greenhouse Gas Control,* **24**, 1-13.

Vilarrasa, V., J. Rutqvist, and A.P. Rinaldi [2015] Thermal and capillary effects on the caprock mechanical stability at In Salah, Algeria. *Greenhouse Gases: Science and Technology*, doi: 10.1002/ghg.1486.

Wild, K.M., F. Amann, C.D. Martin, J. Wassermann, and C. David [2015] Dilatancy of clay shales and its impact on pore pressure evolution and effective stress for different triaxial stress paths. *49th US Rock Mechanics/ Geomechanics Symposium*, San Francisco, 28 June - 1 July 2015, ARMA 15-0496.

Chemical influence of pore pressure on brine flow in clay-rich material

Etienne Cassini[1], Danila Mylnikov[1], Roman Makhnenko[1,2]

[1] Laboratory of Soil Mechanics – Chair “Gaz Naturel” Petrosvibri, Swiss Federal Institute of Technology (EPFL), Lausanne, Switzerland

[2] Department of Civil and Environmental Engineering, University of Illinois at Urbana-Champaign, USA

Hydromechanical properties of shales are complex due to the involved material structure, with the solid matrix being mainly formed by swelling clays and porosity dominated by nanometer scale tortuous voids with large aspect ratios. Intrinsic permeability of restructured Opalinus Clay (Swiss shale) brought to shallow geological storage conditions was measured with *in situ* brine. Under constant temperature, vertical stress, and downstream fluid pressure, steady-state flow experiments show a significant trend of permeability decrease with increasing differential (upstream minus downstream) fluid pressure, thus contradicting the conventional Darcy’s description. To interpret these experimental measurements, brine permeability is derived using a one-step self-consistent homogenization scheme based on the knowledge of material’s pore structure. While mechanical and thermal effects cannot explain the permeability decrease, the trend is reproduced with the correct order of magnitude by considering a chemical effect: a pore size reduction in the sample due to water adsorption at mineral surface.

Introduction

Shales are fissile rock formations composed of inert mineral inclusions embedded in a clay matrix (Weaver 1988). The amount of clay is usually very high, e.g. around 60% in Opalinus Clay - a Swiss shale (Bossart 2012), and as a consequence shales exhibit certain particular features, such as high level of anisotropy, self-healing capacity, and very low permeability. Because of the high specific surface area of the clay minerals and their *mille-feuille* structure, shale’s behavior is also very sensitive to water saturation and its chemical composition. Shales now are broadly considered as seals for nuclear waste and CO_2 storage and in petroleum industry for unconventional gas exploitation. Therefore, fluid and gas permeability, including permeability to *in situ* water or brine, are the key parameters to study for the safety, the efficiency, and the scientific comprehensiveness of the material.

Permeability of a geomaterial is a macro-parameter, which is influenced by the structure of its pore system and eventual chemical phenomenon leading to pore size reduction or pore closure. Permeability measurements provide important information on the material's microstructure, especially in a case where direct investigations at the micro-scale are impossible. To conclude on material behavior at micro-level, permeability measurements should demonstrate high level of accuracy and confidence, which can be achieved by the steady-state flow technique. In this paper we discuss the results on permeability measurements for clay-rich material during steady-state flow of brine and interpret them considering water adsorption, with a one-step self-consistent homogenization scheme.

Experimental methods

Remolded (i.e., reconstituted) shale – Opalinus Clay – saturated with natural brine (Pearson 2002) is studied in the current work. Remolded specimens are prepared by crushing the intact material in a grinder, sieving the particles with a size smaller than 0.5 mm, mixing with brine corresponding to approximately 1.5 times the liquid limit (or 60%), and consolidating at 350 kPa vertical stress for at least 72 hours in one-dimensional conditions. Obtained cylindrical specimens have porosity of 0.33 and the degree of saturation is 0.85 – 0.90. Crushing of shale preserves the flake-like structure of an intact material and eliminates structural anisotropy.

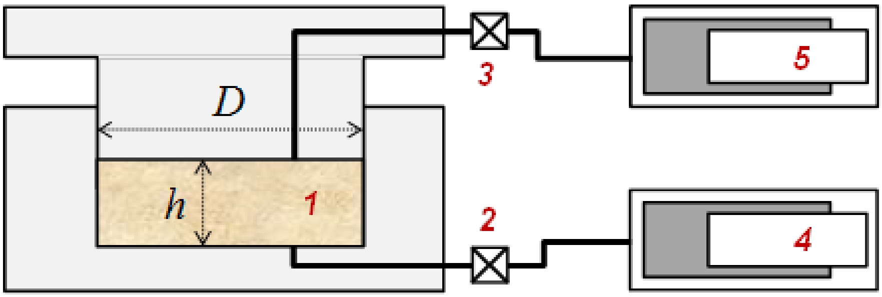

Fig. 1: Scheme of the experimental setup. 1 – rock specimen inside the oedometric cell; 2 and 3 – upstream and downstream pressure transducers respectively; 4 and 5 – upstream and downstream pressure/volume controllers respectively.

Tested specimen (height *h* = 12.5 mm and diameter *D* = 35 mm) is then gradually brought to *in situ* conditions in the oedometric cell: 27 MPa axial total stress (σ_v) and 8 MPa pore pressure (p), which results in the porosity reduction to 0.15. Back pressure saturation method is implemented for 7 days with graduate increase of upstream and downstream pressures and promoting the flow through the specimen. It allows achieving full saturation (at $p > 7$ MPa) that is confirmed by measurements of constant Skempton's *B* coefficient values while the effective mean stress (P') is preserved to be the same (ASTM D4767-11) and equal to 9 MPa. Recorded undrained pore pressure increments are corrected for the influence of "dead" volume (Makhnenko and Labuz 2016) and provide $B = 0.85$, while *B* is measured to be isotropic and equal to 0.99 in conventional triaxial cell at $P' = 0.2$ MPa. Effective mean stress and bulk modulus are calculated from applied vertical stress and vertical deformation by taking drained Poisson's ratio $\nu = 0.3$ (measured in conventional triaxial test at $P' = 0.2 – 0.7$ MPa). Biot coefficient α is calculated from measured unjacketed bulk modulus $K_s' = 8.9$ GPa and the bulk modulus of the brine at pressures above 3 MPa is found to be $K_{br} = 2.0$ GPa – slightly lower than the one of pure water. Summary of the material parameters of investigated remolded shale is given in Table 1.

Table 1: Material properties of remolded shale at $\sigma_v = 27$ MPa, $p = 8$ MPa.

Porosity n, [-]	Bulk modulus K, [GPa]	Skempton's coef. B, [-]	Biot coef. α, [-]	Poisson's ratio ν, [-]
0.15	2.5	0.85	0.72	0.3

Results

Brine permeability of shale is reported as an intrinsic permeability k_{int} that is determined from Darcy's law after achieving steady-state flow conditions:

$$k_{int} = \frac{4\eta_{br} h \Delta V}{\pi D^2 \Delta p_{diff} \Delta t} \tag{1}$$

Here η_{br} is brine viscosity equal to 0.001 Pa·s, Δp_{diff} is the differential fluid pressure, and ΔV is the fluid volume that passed through the specimen during the time period Δt. The differential fluid pressure is determined as the difference in readings of the upstream and the downstream pressure transducers (Fig. 1). Upstream and downstream pressure/volume controllers provide measurements of brine volume that enters and exits the specimen respectively.

Considering all the contributing factors, permeability is reported with the accuracy of 2.5% when the duration of steady-state flow exceeds 12 hours. Steady-state condition and the consistence of the measurements are ensured by obtaining constant permeability values with standard deviation of 2.5% for several consecutive flow cycles at a fixed differential fluid pressure.

Permeability of the material is measured at several differential pressure values after the steady-state flow of brine is established through the specimen. Downstream fluid pressure is kept at constant value of 8 MPa, while upstream pressure is increased several times. The results demonstrate consistent nonlinear decreasing trend of brine permeability with increasing differential fluid pressure (Table 2).

Table 2: Values of brine permeability for the remolded shale as a function of differential fluid pressure.

Differential pressure, MPa	1.5	3.0	6.0	8.0
Intrinsic permeability, m²	1.3e-20	1.2e-20	9.0e-21	8.5e-21

Measured values of remolded shale (Opalinus Clay) permeability are ~ 10^{-20} m^2, while reported intrinsic permeability of the intact material ranges from 10^{-21} to 10^{-19} m^2 (Romero et. al, 2013). Mercury intrusion porosimetry (MIP) measurements performed on the tested sample show a mono-modal pore size repartition with a peak at 21 nm inter-platelet distance (Fig. 2). Pores of this size are supposed to be flat (crack-like) and localized in the clay matrix.

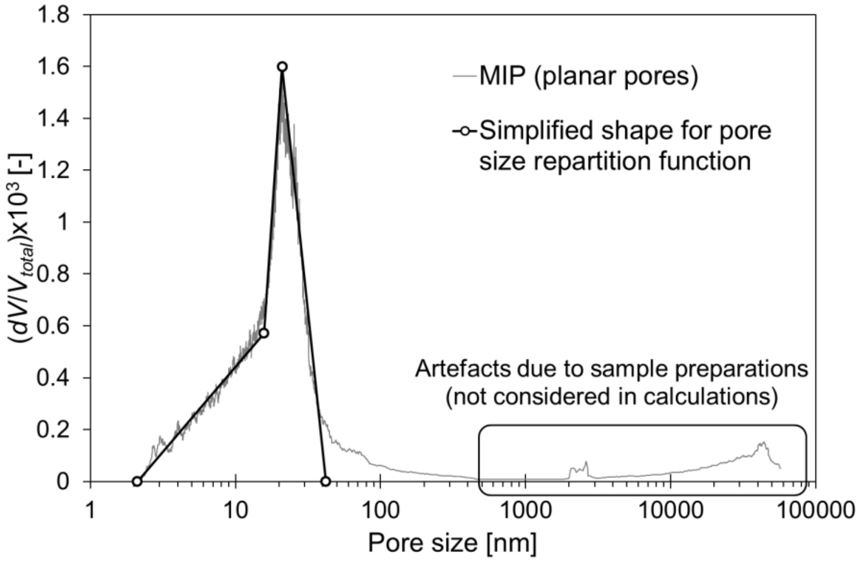

Fig. 2: MIP measurements of pore size distribution in tested remolded shale with hypotheses of planar pores (*V* - volume of intruded mercury).

Discussion

Observed decreasing trend of intrinsic brine permeability of remolded shale, with increasing fluid differential pressure at constant downstream pressure, cannot be explained using only the poromechanical considerations. An increase in brine pressure upstream with constant downstream pressure should lead to increase in both porosity and pores size upstream and preserve the microstructure downstream, leading to a global increase of the permeability. Moreover, this increase in porosity and permeability is evaluated using poroelastic relationships to be on the order of a few percent, whereas the decrease in permeability observed here is of 35%. Also, the observed trend cannot be explained by a thermal effect, e.g., for a conservative calculation that considers unidirectional flow between two adiabatic platelets. Using Stokes equations for non-isotherm viscous flow and brine thermal conduction at 24°C of 0.6 $\mathrm{W \cdot m^{-1} \cdot K^{-1}}$, the elevation of temperature along the flow can be shown to be much lower than 1°C.

Suggested explanation of the experimental observations deals with chemistry and a reduction of the brine accessible porosity in the upstream section of the sample where brine pressure is higher. Due to the characteristic structure of shale, with very small pores and high specific surface area, brine adsorption at the clay surface, which increases with fluid pressure, should be considered. The thickness of a single layer of water is of 0.3 nm, so the adsorption of multiple water layers at the surface of clay minerals in the shale sample can lead to the closure of the smallest pores (~ nm) and cause a reduction of the effective pore size of the larger pores.

In this work, a numerical derivation of the sample permeability, assumed to be isotropic, is performed based on continuum fluid mechanics and homogenization theory (Dormieux et al. 2006). The goal of the modeling is to investigate if water adsorption is a good candidate for explaining the experimental data, both in terms of the trend and the order of magnitude. The simulation is based on a decomposition of the sample in 20 vertical layers where pressure is supposed to be constant. The permeability of each layer is calculated iteratively from upstream to downstream to determine the brine pressure in the next layer and then deduce its permeability. Flow is constant between the different layers and the convergence criterion is on the downstream pressure. Calculations are performed in MatLab©.

Based on continuum fluid mechanics considerations at the nanoscale and a slipping boundary condition between brine and mineral surface (Klinkenberg effect), the local tangential permeability k_t in a planar pore is

$$k_t = \left(h - 2\Delta h\right)^2 \left(\frac{1}{3} + \frac{\beta}{h - 2\Delta h}\right) \tag{2}$$

Here h is the interplatelet distance, Δh is the thickness of the adsorbed layer of water, and β is a slipping parameter for the flow boundary condition. From molecular dynamics simulations (Botan et al. 2011), β value is fixed at 0.21 nm. The term (h - 2Δh) represents the effective accessible pore size. Formally, this relationship holds for planar pores with an opening larger than the thickness of a few water layers (e.g., 10) and continuum mechanics is no longer valid in smaller pores, where the discreteness of water molecules should be considered. However, here we accept continuum mechanics considerations for pore openings larger than one water layer, i.e. 0.3 nm, and smaller pores are assumed to be impermeable.

Equation (2) is considered to be a fair approximation for oblate pores with high aspect ratios and the local permeability is used in a one-step self-consistent scheme similar to the one proposed by Cariou (2010). Although in the present work the mineral solid matrix is not spherical, but oblate with the aspect ratio $\gamma_s <$ 1. In this case, a small variation of the aspect ratio can lead to an order of magnitude difference in the homogenized permeability (Fig. 3). The localization tensor in the case of oblate pores, or mineral inclusions, is calculated from equations provided by Giraud et al. (2015). This is a first order approach to derive shale properties, as a true homogenization scheme for shales should be two stepped: one step for the clay matrix and another one for the inert mineral inclusions.

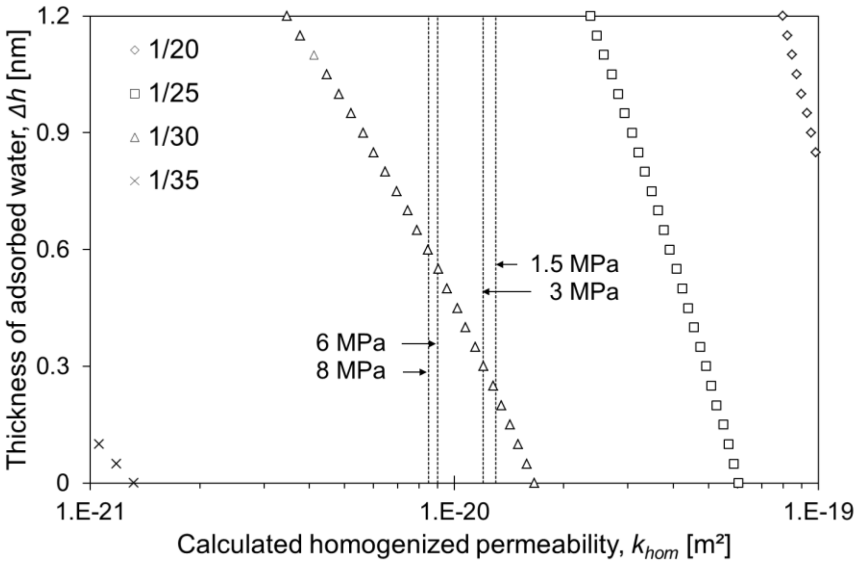

Fig. 3: Calculated homogenized permeability for different values of the thickness of the adsorbed water layer and different aspect ratio of the solid particles. The dashed vertical lines indicate the experimental results dependence on the differential fluid pressures.

The homogenization scheme is applied for different values of γ_s and Δh to investigate the influence of these parameters. Results are displayed in Fig. 3 and demonstrate the strong dependence on the solid aspect ratio, small variation of which can lead to an order of magnitude change in permeability. For a well-chosen solid aspect ratio, here 1/30, experimentally observed permeability decrease trend can be linked to the passage from one adsorbed water layer ($\Delta h \approx 0.3$ nm) to two layers ($\Delta h \approx 0.6$ nm). Adsorption of brine is then related to its pressure with a Toth (1971) adsorption isotherm:

$$\Delta h = \Delta h_m \frac{\left(p/p_{ref}\right)^t}{1+\left(p/p_{ref}\right)^t} \tag{3}$$

where Δh_m is the maximum thickness of adsorbed water, chosen as a multiple of 0.3 nm, and p_{ref} and t are fitting parameters. Two examples of numerical simulations of sample permeability with this model are shown in Fig. 4, reproducing the decreasing permeability trend within the order of magnitude. Proper measurements of the adsorption parameters should be based on independent brine injection tests, while the intrinsic material permeability could be measured with an inert gas, providing further insight into the nature of complicated hydro-mechanical behavior of clays and shales.

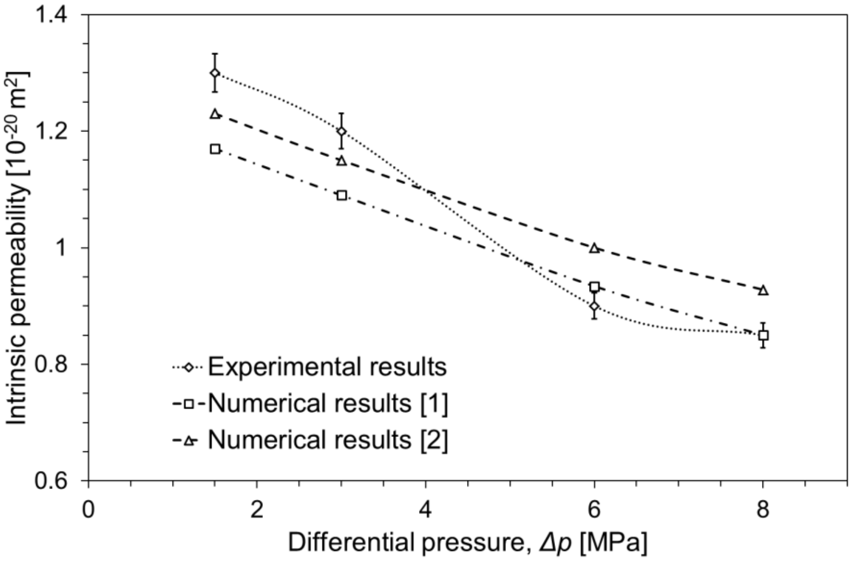

Fig. 4: Brine permeability evolution of remolded shale specimen with differential fluid pressure, experimental results (diamonds with error bars) and numerical simulations. Adsorption model parameters are Δh_m = 1.2 nm, p_{ref} = 13 MPa, and t = 3.5 in simulation [1] (squares), and Δh_m = 0.9 nm, p_{ref} = 12 MPa, and t = 4 in simulation [2] (triangles).

Conclusions

Flow measurements performed on a sample of remolded shale (Opalinus clay) show a significant decrease of brine permeability with increasing brine pressure. Influence of mechanical and thermal effects on this trend are negligible, while brine adsorption in the sample leading to a modification in the fluid accessible porosity has been considered as a possible option to explain the observed permeability decrease. Though numerical results are very sensitive to the hypothesis made for the pore structure (e.g., value of the solid particles aspect ratio) and the choice of parameters for the adsorption isotherm, they predict the decreasing permeability trend within the order of magnitude. For the better understanding of material behavior, permeability is suggested to be independently measured with an inert gas. Then, brine injection and flow tests could be used to determine the adsorption parameters and explain the complicated nature of hydro-mechanical behavior of clay-rich and shaley materials.

Acknowledgements

Opalinus clay cores were provided by Swisstopo in the framework of Mont Terri project, CS-C experiment. R. Makhnenko acknowledges the support from SCCER-SoE (Switzerland) grant KTI.2013.288 and Swiss Federal Office of Energy (SFOE) project CAPROCK #810008154.

References

ASTM D4767 (2011). Standard Test Method for Consolidated Undrained Triaxial Compression Test for Cohesive Soils.

Bossart P (2012) Characteristics of the Opalinus Clay at Mont Terri. http://www.mont-terri.ch/internet/montterri/de/home/geology/key_characteristics.html.

Botan A, Rotenberg B, Marry V, Turq P, Noetinger B (2011). Hydrodynamics in clay nanopores. J Phys Chem C 115(32):16109-16115.

Cariou, S (2010). Couplage hydro-mécanique et transfert dans l'argilite de Meuse/Haute-Marne: approches expérimentale et multi-échelle (Doctoral dissertation, Ecole des Ponts ParisTech).

Dormieux L, Kondo D, Ulm FJ (2006). Microporomechanics. John Wiley & Sons, Chichester, UK, 327 pp.

Romero E, Senger R, Marschall P, Gomez R (2013). Air tests on low-permeability claystone formations. Experimental results and simulations. In: Laloui L, Ferrari A (eds.) Multiphysical Testing of Soils and Shales, pp. 69–83, Springer, Berlin.

Giraud A, Sevostianov I, Chen F, Grgic D (2015). Effective thermal conductivity of oolitic rocks using the Maxwell homogenization method. Int J Rock Mech & Mining Sci 80:379-87.

Makhnenko RY, Labuz JF (2016). Elastic and inelastic deformation of fluid-saturated rock. Phil Trans R Soc A. 374:20150422, doi: 10.1098/rsta.2015.0422.

Pearson FJ (2002). PC experiment: recipe for artificial pore water. Mont Terri Project, Technical Note 2002–17.

Toth J (1971). State equations of the solid-gas interface layers. Acta Chim Acad Sci Hungar. 69(3):311-28.

Weaver CE (1988). Clays, muds, and shales. Elsevier, Amsterdam, 819 pp.

Appendix D

Journal papers

ARTICLE IN PRESS

Journal of Rock Mechanics and Geotechnical Engineering xxx (2016) 1–14

Contents lists available at ScienceDirect

Journal of Rock Mechanics and Geotechnical Engineering

journal homepage: www.rockgeotech.org

Full Length Article

Geomechanical analysis of the influence of CO_2 injection location on fault stability

Victor Vilarrasa [a,b,c,*], Roman Makhnenko [a,d], Sohrab Gheibi [e]

[a] École Polytechnique Fédérale de Lausanne, Lausanne, Switzerland
[b] Institute of Environmental Assessment and Water Research (IDAEA-CSIC), Barcelona, Spain
[c] Associated Unit: Hydrogeology Group (UPC-CSIC), Barcelona, Spain
[d] Department of Civil & Environmental Engineering, University of Illinois at Urbana-Champaign, USA
[e] Norwegian University of Science and Technology, Trondheim, Norway

ARTICLE INFO

Article history:
Received 22 March 2016
Received in revised form
29 May 2016
Accepted 6 June 2016
Available online xxx

Keywords:
Carbon dioxide (CO_2) injection
Geomechanics
Fault stability
Induced seismicity
Fault permeability

ABSTRACT

Large amounts of carbon dioxide (CO_2) should be injected in deep saline formations to mitigate climate change, implying geomechanical challenges that require further understanding. Pressure build-up induced by CO_2 injection will decrease the effective stresses and may affect fault stability. Geomechanical effects of overpressure induced by CO_2 injection either in the hanging wall or in the foot wall on fault stability are investigated. CO_2 injection in the presence of a low-permeable fault induces pressurization of the storage formation between the injection well and the fault. The low permeability of the fault hinders fluid flow across it and leads to smaller overpressure on the other side of the fault. This variability in the fluid pressure distribution gives rise to differential total stress changes around the fault that reduce its stability. Despite a significant pressure build-up induced by the fault, caprock stability around the injection well is not compromised and thus, CO_2 leakage across the caprock is unlikely to happen. The decrease in fault stability is similar regardless of the side of the fault where CO_2 is injected. Simulation results show that fault core permeability has a significant effect on fault stability, becoming less affected for high-permeable faults. An appropriate pressure management will allow storing large quantities of CO_2 without inducing fault reactivation.

1. Introduction

Carbon dioxide (CO_2) emissions to the atmosphere should be significantly reduced to mitigate climate change. This imperative necessity has recently reached an international consensus at the COP21 meeting in Paris in December 2015. The objective is to limit the temperature increase caused by anthropogenic CO_2 emissions in 2 °C. To achieve this objective, CO_2 emissions should drop by a factor of 2 by 2050 with respect to the current emissions (Fuss et al., 2014). According to the International Energy Agency (IEA), geologic carbon storage has the potential to contribute to one fifth of the total CO_2 emissions reduction (IEA, 2010). This percentage represents storing 8 Gt/yr of CO_2 in deep geologic formations by 2050. This huge amount of CO_2 would be injected in multiple industrial-scale projects that would capture CO_2 from industrial point sources, implying a continuous mass flow rate in the order of millions of tons per year in each injection well during several decades (Szulczewski et al., 2012).

Maintaining CO_2 injection over years will cause the pressurization of large areas within the storage formation (Birkholzer et al., 2015). Even though the radius of the CO_2 plume may be of a few kilometers, the radius of the pressure perturbation cone with an overpressure higher than 0.1 MPa can exceed hundreds of kilometers for an injection of several decades (Birkholzer et al., 2009). Higher pressure cutoffs that may induce fault stability issues in critically stressed faults, such as 1 MPa, can extend tens of kilometers (Birkholzer et al., 2009; Verdon, 2014). Furthermore, once large-scale geologic carbon storage projects will be fully deployed, superposition of overpressure from different injection wells in the same sedimentary basin is expectable, leading to an even larger pressurized region (Zhou and Birkholzer, 2011). Thus, in spite of the fact that injection wells will most likely be placed far away from identified faults to minimize the risk of fault reactivation,

---

[*] Corresponding author.
E-mail address: victor.vilarrasa@upc.edu (V. Vilarrasa).

Peer review under responsibility of Institute of Rock and Soil Mechanics, Chinese Academy of Sciences.

http://dx.doi.org/10.1016/j.jrmge.2016.06.006

Please cite this article in press as: Vilarrasa V, et al., Geomechanical analysis of the influence of CO_2 injection location on fault stability, Journal of Rock Mechanics and Geotechnical Engineering (2016), http://dx.doi.org/10.1016/j.jrmge.2016.06.006

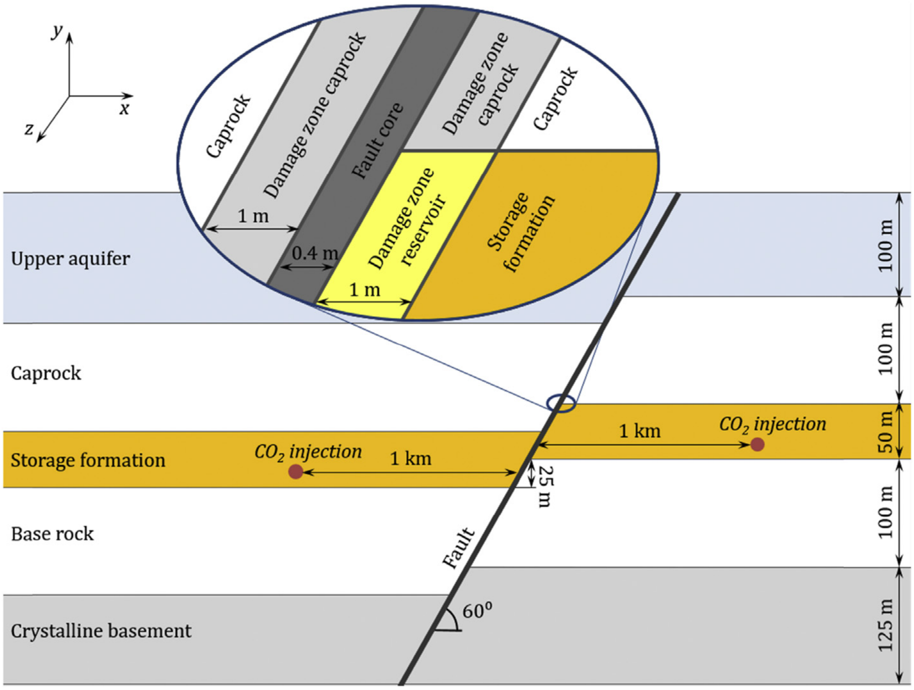

Fig. 1. Schematic representation of the model geometry. CO_2 is injected either in the hanging wall or in the foot wall 1 km away from the fault, which has an offset of 25 m. The fault is composed of a fault core, which extends all along the fault, and damage zones on both sides of the core. The damage zones vary for each rock type, as indicated in the inset.

overpressure will eventually reach faults in the far field, affecting their stability (Streit and Hillis, 2004).

Fault stability analysis associated with CO_2 injection is usually modeled in reservoirs of limited size (Vidal-Gilbert et al., 2010). CO_2 injection in closed storage formations bounded by low-permeable faults may lead to fault reactivation if no pressure management is performed (Cappa and Rutqvist, 2011a; Mazzoldi et al., 2012). One concern related to fault reactivation is the potential of shear slip to open up migration paths through which CO_2 could leak (Zoback and Gorelick, 2012). However, CO_2 leakage is unlikely to happen because (1) fault reactivation usually occurs in the crystalline basement, below the storage formation (Verdon, 2014); (2) the caprock sealing capacity is likely to remain unaffected (Pan et al., 2013, 2014; Vilarrasa et al., 2014); and (3) the heterogeneity of faults hinders CO_2 upwards migration (Rinaldi et al., 2014). More importantly, fault reactivation is accompanied by a seismic event. CO_2 injection has the potential to induce seismicity of magnitude three that could be felt on the ground surface (Cappa and Rutqvist, 2012). Felt induced seismic events should be avoided because they generate nuisances and fear in the local population, which may lead to the closure of geologic carbon storage projects (Oldenburg, 2012). There are already several examples of fluid injection projects that have been halted because of felt induced seismicity, like the geothermal project at Basel in Switzerland (Häring et al., 2008), the seasonal natural gas storage project of Castor in Spain (Cesca et al., 2014), and wastewater disposal wells at Guy-Greenbrier, Arkansas (Horton, 2012) and Youngstown, Ohio in the USA (Ellsworth, 2013).

The studies that model fault reactivation induced by CO_2 injection usually consider injection in the hanging wall of the fault (Cappa and Rutqvist, 2011b; Rinaldi et al., 2015), though, in fact, it may occur on either side of the fault (Pereira et al., 2014). Furthermore, these studies have focused on predicting the magnitude of the induced earthquakes resulting from the fault slip caused during fault reactivation, but not on the changes in effective stresses induced by overpressure and stress redistribution that occur around the fault and that trigger fault instability.

The aim of this paper is to investigate how CO_2 injection, either in the hanging wall or in the foot wall, affects fault stability. We first present the geometry of the considered problem, justify the material properties for each rock and explain the numerical solution to the problem. Then, we show the numerical results for fault stability when injecting CO_2 in the hanging wall and in the foot wall of an extensional fault. Finally, we discuss the implications of this study and draw the conclusions.

2. Methods

2.1. Geometry

We model the lower portion of a sedimentary basin (Fig. 1). The main feature of the model is a normal fault with an inclination of 60°. This fault becomes critically oriented in a normal faulting stress regime, like the one of the model, if its friction angle equals 30° (Vilarrasa et al., 2013a). The fault is formed by a fault core and damage zones on both sides of the core (Caine et al., 1996). The fault core is assumed to have the same properties all along the fault. However, the damage zones have different properties depending on the rock types that they are in contact with. We distinguish three types of damage zones: one for clastic rocks typical of reservoirs, one for shaly materials that act as confinement layers, and another one for the crystalline basement.

Plane strain conditions are assumed due to the geometry of the problem, which is extensive in the out-of-plane direction. CO_2 is injected through a horizontal well either in the hanging wall (left of the fault in Fig. 1) or in the foot wall (right of the fault in Fig. 1) in a 50 m-thick storage formation. The injection wells are placed 1 km away from the fault. The offset of the fault is 25 m, so half of the storage formation overlaps on both sides of the fault. The storage formation is overlaid and underlain by low-permeable and high entry pressure formations. The confinement layers have a thickness of 100 m. Below the base rock, the model includes the upper 100 m and 125 m of the crystalline basement on the hanging wall and the

Please cite this article in press as: Vilarrasa V, et al., Geomechanical analysis of the influence of CO_2 injection location on fault stability, Journal of Rock Mechanics and Geotechnical Engineering (2016), http://dx.doi.org/10.1016/j.jrmge.2016.06.006

foot wall of the fault, respectively. Above the caprock, a secondary aquifer is modeled. The thickness of this aquifer is 125 m and 100 m on the hanging wall and the foot wall, respectively. The top of the secondary aquifer is placed at a depth of 1275 m. The geologic medium on the top of the secondary aquifer is not included in the model, but an overburden of equivalent weight is applied on the top of the model. The model extends laterally 15 km on both sides of the fault.

2.2. Governing equations

To simulate CO_2 injection in a deep saline aquifer, mass conservation and momentum conservation of both CO_2 and water have to be solved. Mass conservation of these two fluids can be written as (Bear, 1972):

$$\frac{\partial(\varphi S_\alpha \rho_\alpha)}{\partial t} + \nabla\cdot(\rho_\alpha \boldsymbol{q}_\alpha) = r_\alpha \quad (\alpha = \mathrm{c},\mathrm{w}) \tag{1}$$

where φ is the porosity; S_α is the saturation degree of α-phase; ρ_α is the density of α-phase; t is the time; $\boldsymbol{q}_\alpha$ is the volumetric flux of α-phase; r_α is the phase change term, i.e. CO_2 dissolution into water and water evaporation into CO_2; and α is either the CO_2-rich phase (c) or the aqueous phase (w). We neglect evaporation of water into CO_2, i.e. $r_\mathrm{w} = 0$.

The volumetric flux in Eq. (1) is given by momentum conservation of the fluid phases, which for slow laminar flow in permeable porous media is described by Darcy's law:

$$\boldsymbol{q}_\alpha = -\frac{k k_{\mathrm{r}\alpha}}{\mu_\alpha}(\nabla p_\alpha + \rho_\alpha g \nabla z) \quad (\alpha = \mathrm{c},\mathrm{w}) \tag{2}$$

where k is the intrinsic permeability, $k_{\mathrm{r}\alpha}$ is the relative permeability of α-phase, μ_α is the viscosity of α-phase, p_α is the pressure of α-phase, g is the gravity acceleration, and z is the vertical coordinate.

The overpressure resulting from CO_2 injection will induce deformation and modify the stress state in the geologic media. The momentum balance of the solid phase needs to be solved to take into account the mechanical effects, and if inertial terms are neglected, the momentum balance reduces to the equilibrium of stresses:

$$\nabla\cdot\boldsymbol{\sigma} + \boldsymbol{b} = \boldsymbol{0} \tag{3}$$

where $\boldsymbol{\sigma}$ is the stress tensor with σ_x, σ_y, and σ_z being the diagonal elements and τ_{xy}, τ_{yz}, and τ_{zx} being the off-diagonal elements; and $\boldsymbol{b}$ is the body forces vector.

We assume that the geologic media remain elastic throughout the whole simulation and that the stress–strain relationship is given by the generalized Hooke's law:

$$\boldsymbol{\varepsilon} = \frac{\sigma'_\mathrm{m}}{3K}\boldsymbol{I} + \frac{1}{2G}(\boldsymbol{\sigma}' - \sigma'_\mathrm{m}\boldsymbol{I}) \tag{4}$$

where $\boldsymbol{\varepsilon}$ is the elastic strain tensor; $\boldsymbol{I}$ is the identity matrix; $\boldsymbol{\sigma}'$ is the effective stress tensor defined as $\boldsymbol{\sigma}' = \boldsymbol{\sigma} - p\boldsymbol{I}$, where p is the maximum between water and CO_2 pressures; $\sigma'_\mathrm{m} = \mathrm{tr}(\boldsymbol{\sigma}')/3$ is the mean effective stress; $K = E/[3(1-2\nu)]$ is the bulk modulus, $G = E/[2(1+\nu)]$ is the shear modulus, where E is the Young's modulus, and ν is the Poisson's ratio. We assume that stress and strain are positive in compression and negative in extension.

To evaluate fracture stability, we conservatively assume that a cohesionless critically oriented fracture could exist at every point, meaning that a standard Mohr–Coulomb failure criterion can be used. Adopting Mohr–Coulomb failure criterion, the mobilized friction angle can be calculated as

$$\phi_\mathrm{mob} = \arctan\left(\frac{\tau}{\sigma'_\mathrm{n}}\right) \tag{5}$$

where τ is the tangential stress, and σ'_n is the normal effective stress acting on the cohesionless critically oriented fracture. The mobilized friction angle gives an idea of how close the stress state is to failure conditions. The higher the mobilized friction angle, the higher the potential for slip reactivation. If the mobilized friction angle equals the actual friction angle, shear failure conditions are reached and the fracture or fault would undergo shear slip, which could induce seismicity. In general, the actual friction angle of geomaterials can be considered as 30° (Byerlee, 1978).

2.3. Material properties

Berea sandstone with permeability of $\sim 10^{-14}$ m^2 is considered to form the storage formation. Swiss shale – Opalinus clay – is taken as a ductile clay-rich (>55% of clay) low-permeable (with the k value of $\sim 10^{-20}$ m^2) caprock and base rock representative. The upper aquifer consists of Indiana limestone (with the k value of $\sim 10^{-14}$ m^2) and the crystalline basement is formed by Charcoal granite (with the k value of $\sim 10^{-20}$ m^2). The material properties were measured in conventional triaxial experiments and reported at corresponding effective mean stresses (Table 1) (e.g. Makhnenko and Labuz, 2016). Gas entry values and porosities are obtained from mercury intrusion porosimetry tests. The reported values of porosity for the confining layers, crystalline basement, and the fault core are the effective porosities, i.e. those contributing to flow. Relative CO_2 and water permeabilities are taken as power functions of saturation, with a power of 3 for the sandstone and the limestone and 6 for the shale and the granite (Bennion and Bachu, 2008).

Properties of the fault (Table 2) are reported as those of the crushed (remolded) shale and damaged sandstone for the fault core and damage zone reservoirs, respectively. Damage zone confinement layers and damage zone basement properties are those of the damaged shale and granite, respectively.

The elastic parameters for the storage formation, upper aquifer, and damage zone reservoir are taken as those related to the drained (long-term) regime of deformation, because the characteristic diffusion time (Detournay and Cheng, 1993) for these rocks is in the order of 1–10 min. Conversely, the undrained (short-term) elastic parameters are reported for the intact and damaged zone confining layers and intact and damaged crystalline basement due to their characteristic time scale of the diffusion processes, which is in the order of 5–500 years. The characteristic pressure diffusion time across the fault core is about two days, which is two orders of magnitude smaller than the considered injection time (1 year), hence the drained response is assumed.

2.4. Numerical solution

We first solve the equilibration of fluid pressure and stresses. Water pressure is hydrostatic and the partial pressure of CO_2 equals 0.01 MPa, which corresponds to an initial concentration of dissolved CO_2 of 2.44×10^{-5} kg/kg of water. We consider that the model is isothermal, with a temperature equal to 60°. This temperature is representative of the temperature of the storage formation (at depth of 1.5 km) assuming a geothermal gradient of 33 °C/km and a surface temperature of 10 °C. The initial stress state corresponds to a normal faulting stress regime, i.e. the vertical

Please cite this article in press as: Vilarrasa V, et al., Geomechanical analysis of the influence of CO_2 injection location on fault stability, Journal of Rock Mechanics and Geotechnical Engineering (2016), http://dx.doi.org/10.1016/j.jrmge.2016.06.006

Table 1
Material properties of the rock types included in the model.

Material	Permeability, k (m^2)	Relative water permeability, k_{rw}	Relative CO$_2$ permeability, k_{rc}	Gas entry pressure, p_0 (MPa)	Van Genuchten shape parameter, m	Porosity	Young's modulus, E (GPa)	Poisson's ratio, ν
Storage formation	4×10^{-14}	S_w^3	S_c^3	0.02	0.8	0.23	14	0.31
Caprock	8×10^{-20}	S_w^6	S_c^6	10	0.3	0.05	2.8	0.4
Base rock	5×10^{-20}	S_w^6	S_c^6	10	0.3	0.05	3	0.39
Upper aquifer	1×10^{-14}	S_w^3	S_c^3	0.2	0.8	0.13	28	0.21
Crystalline basement	4×10^{-20}	S_w^6	S_c^6	12	0.3	0.01	84	0.18

Table 2
Properties of the materials forming the fault.

Material	Permeability, k (m^2)	Relative water permeability, k_{rw}	Relative CO$_2$ permeability, k_{rc}	Gas entry pressure, p_0 (MPa)	Van Genuchten shape parameter, m	Porosity	Young's modulus, E (GPa)	Poisson's ratio, ν
Fault core	1×10^{-19}	S_w^6	S_c^6	4	0.3	0.1	1	0.3
Damage zone reservoirs	2×10^{-13}	S_w^3	S_c^3	0.02	0.8	0.25	7	0.35
Damage zone confinement layers	1.5×10^{-19}	S_w^6	S_c^6	5	0.3	0.09	1.4	0.42
Damage zone basement	1×10^{-16}	S_w^4	S_c^4	1	0.5	0.07	42	0.3

stress, σ_v, is the maximum principal stress and is given by an average density of the geologic media of 23 MPa/km. The initial horizontal stress is obtained from $\sigma_h = 0.69\sigma_v$, which provides a mobilized friction angle of 22.2°, typical of sedimentary basins (Vilarrasa and Carrera, 2015).

CO$_2$ is injected for 1 year at a rate of 2×10^{-3} kg/s per meter in the direction normal to the model plane in the well placed either in the hanging wall or in the foot wall. The horizontal wells are modeled by a vertical line of 1 m, placed 5 m above the bottom of the storage formation. If the horizontal wells were 2 km in length, a total amount of 4 kg/s would be injected, which represents injecting 0.126 Mt/yr of CO$_2$. This injection rate is within the range of those at In Salah, Algeria, where the storage formation has a similar permeability to the one considered in this study (Rutqvist, 2012). We impose constant pressure on the outer boundaries, placed 15 km away from the fault on both sides of the model. No flow is considered at the top and bottom boundaries. The mechanical boundary conditions are a constant stress equal to the weight of the overburden on the top boundary and no displacement perpendicular to the other boundaries.

The two-phase flow problem in deformable porous media is solved in a fully coupled way using the finite element code CODE_BRIGHT (Olivella et al., 1994, 1996), which has been extended for CO$_2$ injection (Vilarrasa et al., 2013b). The mesh is made of 5775 quadrilateral elements, with a higher refinement around the fault and the injection wells. Vertically, the elements have a size of 4 m in the storage formation and the lower portion of the caprock, progressively increasing up to 35 m at the top and bottom boundaries. Horizontally, the elements are of tens of centimeters around the fault and of metric scale around the wells, and progressively increase to a size of 2 km at the outer boundaries. The fault core thickness is discretized in two elements and the damage zones on each side of the core in three elements. We have ensured that a further refinement of the mesh does not affect the results.

3. Results

3.1. CO$_2$ injection in the hanging wall

CO$_2$ injection in the proximity of a low-permeable fault (1 km in this case) causes the pressurization of the region between the injection well and the fault (Fig. 2). If the fault core is low-permeable, it acts as a flow barrier reducing the flow rate across the fault to a negligible quantity and preventing pressure build-up on the other side of the fault, i.e. the foot wall when CO$_2$ is injected in the hanging wall (Fig. 2). Unlike the region between the injection well and the fault, overpressure dissipates significantly with distance to the injection well on the side that is open. This pressure distribution has a direct effect on CO$_2$ dynamics.

Fig. 3 illustrates how the presence of a low-permeable fault affects the shape of the CO$_2$ plume. Since fluid pressure around the plume is higher on one side of the fault than that on the other side, CO$_2$ is pushed away from the fault, resulting in an asymmetry of the plume. This CO$_2$ plume shape can give information on the presence of low-permeable faults that affect the pressure distribution.

Fig. 4 displays the stress changes (Fig. 4b–e) caused by the overpressure (Fig. 4a) and the induced changes in rock stability (Fig. 4f). The horizontal total stress increases proportionally to overpressure in the out-of-plane direction, i.e. parallel to the fault (Fig. 4d). Thus, the horizontal total stress increases in the hanging wall of the fault, but not in the foot wall. In the direction

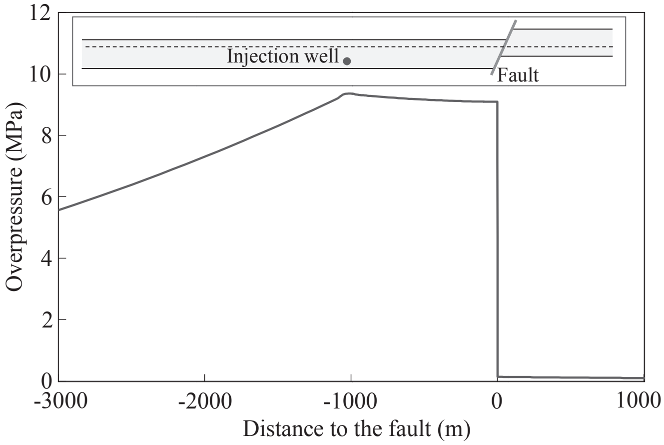

Fig. 2. Overpressure distribution after one year of CO$_2$ injection in the hanging wall of a low-permeable fault. Overpressure is measured at a horizontal section that coincides with the middle of the portion of the storage formation that overlaps on both sides of the fault, as indicated by the dashed line in the inset.

Please cite this article in press as: Vilarrasa V, et al., Geomechanical analysis of the influence of CO$_2$ injection location on fault stability, Journal of Rock Mechanics and Geotechnical Engineering (2016), http://dx.doi.org/10.1016/j.jrmge.2016.06.006

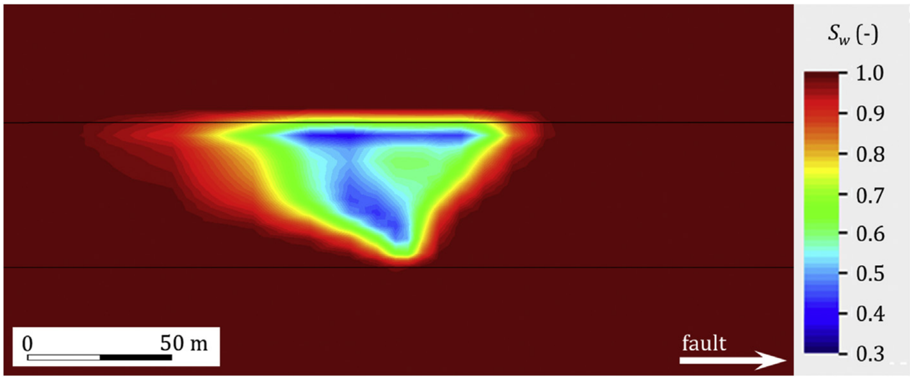

Fig. 3. CO_2 plume after one year of injection in the hanging wall, 1 km away from the fault. Note that the plume is asymmetric due to the higher overpressure on the side closer to the fault, which pushes the injected CO_2 away from the fault. The side where the fault is located is indicated with an arrow.

perpendicular to the fault, the horizontal total stress change presents a similar distribution to that in the out-of-plane direction, but the presence of the fault alters the total stress changes around it (Fig. 4b). This anomaly in the stress change extends on both sides of the fault for a distance that is approximately equal to the thickness of the storage formation. The region not affected by the presence of the fault has a similar increase in the horizontal total stresses in all directions. This increase is very similar to the analytical estimation that can be done according to the total stress increment induced by overpressure in a laterally extensive aquifer, which equals $\Delta\sigma_{\rm h} = \Delta p(1-2\nu)/(1-\nu)$ (Rutqvist, 2012).

Around the fault, the horizontal total stress increases in the direction perpendicular to the fault in the foot wall in the lower half of the storage formation, which overlaps with the upper part of the storage formation in the hanging wall (Fig. 4b). Furthermore, the horizontal total stress increases by a lower magnitude than that in the rest of the hanging wall in the lower portion of the storage formation, which coincides with the base rock on the other side of the fault. These stress changes are due to the fact that overpressure causes an expansion of the storage formation, which compresses the rock around it. Thus, the lower portion of the storage formation in the foot wall of the fault and the upper portion of the caprock below it undergo compression. The storage formation accumulates more stress because it is one order of magnitude stiffer than the confining layers. Interestingly, the base rock causes a lower increase in the horizontal total stress in the direction perpendicular to the fault in the lower half of the storage formation in the hanging wall, presenting a minimum with almost no horizontal total stress increment close to the fault (Fig. 4b).

Stress redistribution around the fault also affects the vertical total stress (Fig. 4c), which increases in the fault core. Additionally, it also increases at the position close to the fault in the upper half of the storage formation in the hanging wall and in the upper part of the caprock in the foot wall. In contrast, the relative increase is small at the position close to the fault in the lower half of the storage formation in the hanging wall and the vertical total stress decreases in the lower half of the storage formation in the foot wall.

The total stress changes in the vertical and horizontal directions lead to a non-trivial shear stress distribution around the fault (Fig. 4e). Below the storage formation, shear stress changes correspond to those typical of a fault in a normal faulting stress regime, with the hanging wall pointing downwards and the foot wall pointing upwards. Above the storage formation, the opposite shear stress changes are induced, with the hanging wall pointing upwards and the foot wall pointing downwards. This is due to the fact that CO_2 injection causes an expansion of the storage formation on the side where it is injected, i.e. the hanging wall in this case. This expansion pushes the rock upwards above the storage formation and downwards below the storage formation. Additionally, the stress redistribution around the fault induces shear stress changes that point upwards on both sides of the fault in the region where the storage formation overlaps on both sides of the fault (Fig. 4e). In contrast, the shear stress changes point downwards on both sides of the fault in the lower half of the storage formation in the hanging wall and the upper portion of the base rock in the foot wall.

Fig. 4f shows the change in the mobilized friction angle caused by CO_2 injection. While a positive change in the mobilized friction angle means that the rock becomes more unstable because the stress state approaches failure conditions, a negative change leads to a more stable situation. The most critical region is that close to the fault in the lower half of the storage formation in the hanging wall. In contrast, stability improves in the storage formation in the foot wall. Interestingly, the caprock stability experiences a very small change, which suggests that the caprock sealing capacity is not compromised.

Fig. 5 displays the mobilized friction angle around the fault at three horizontal planes. Stability remains unaltered in the plane that crosses the caprock in the hanging wall and the upper portion of the storage formation in the foot wall (green dotted line). In the intermediate plane (blue line), i.e. the one that crosses the fault through the middle of the section in which the storage formation overlaps on both sides of the fault, stability decreases in the hanging wall (the side of the fault where CO_2 is injected) and improves in the foot wall. Stability decreases even more in the lower half of the storage formation in the hanging wall (dashed red line). The least stable conditions occur outside the fault: the most critical zone is placed inside the storage formation around 0.5 m away from the damage zone. On the other side of the fault, stability also decreases in the base rock, but within the first 5 m from the fault, the mobilized friction angle is approximately equal to the initial one.

Fig. 6 depicts the time evolution of the mobilized friction angle at several points. In the zone where the storage formation overlaps on both sides of the fault, the mobilized friction angle increases, meaning that stability decreases in the damage zone of the hanging wall (point *A*), but slightly decreases (stability improves) in the damage zone of the foot wall (point *B*). The stability increase in the foot wall (point *B*) is caused by a decrease in the vertical total stress (Fig. 4c) and an increase in the horizontal total stress (Fig. 4b) combined with an almost constant fluid pressure. The resulting effective stresses lead to shrinkage of the Mohr circle (Fig. 7), thus stability improves. On the other hand, point *A* undergoes a similar change in the total stress in horizontal and vertical directions, which leads to a shift of the Mohr circle towards the failure envelope due to the build-up in fluid pressure occurring in the hanging wall (Fig. 7).

Please cite this article in press as: Vilarrasa V, et al., Geomechanical analysis of the influence of CO_2 injection location on fault stability, Journal of Rock Mechanics and Geotechnical Engineering (2016), http://dx.doi.org/10.1016/j.jrmge.2016.06.006

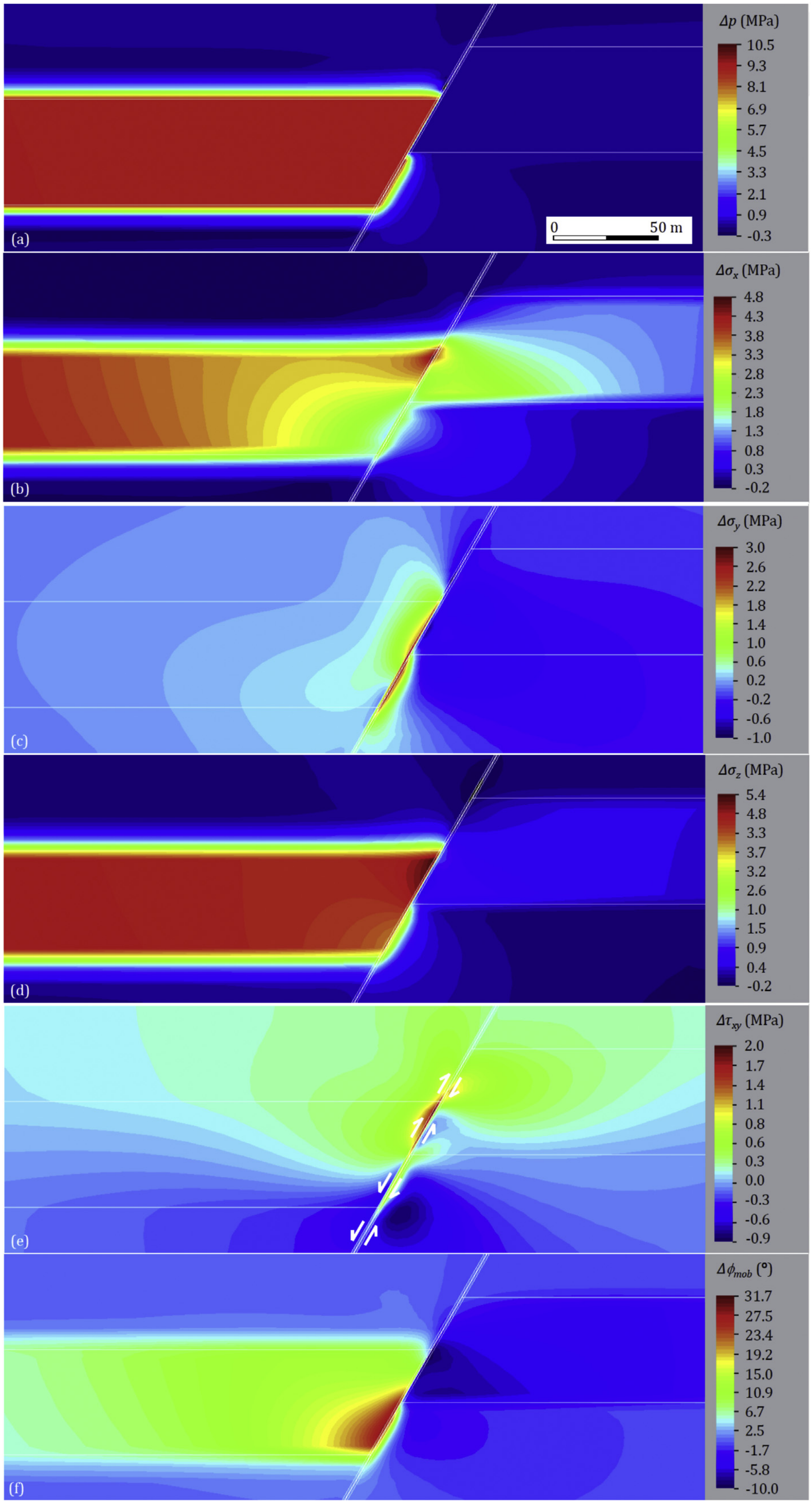

Fig. 4. Distribution of changes in (a) fluid pressure, (b) minimum horizontal total stress (in-plane), (c) vertical total stress, (d) maximum horizontal total stress (out-of-plane), (e) shear stress, and (f) mobilized friction angle after one year of injecting CO_2 in the hanging wall.

Please cite this article in press as: Vilarrasa V, et al., Geomechanical analysis of the influence of CO_2 injection location on fault stability, Journal of Rock Mechanics and Geotechnical Engineering (2016), http://dx.doi.org/10.1016/j.jrmge.2016.06.006

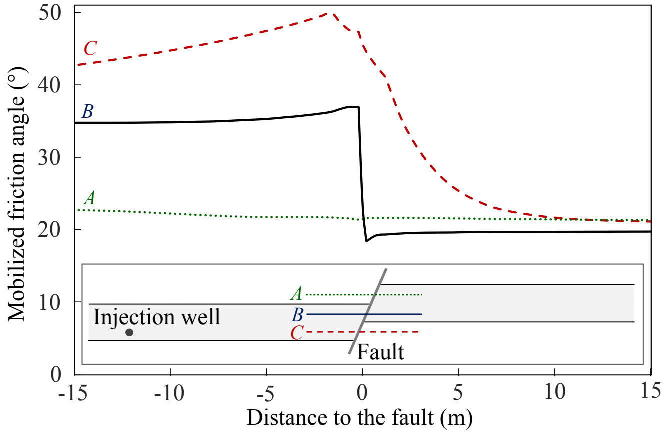

Fig. 5. Mobilized friction angle at three sections crossing the fault (see inset) after one year of injecting CO_2 in the hanging wall.

In the lower half of the storage formation in the hanging wall, the mobilized friction angle increases more rapidly than that in the section where the storage formation overlaps on both sides of the fault (Fig. 6a). This higher rate is caused by the lower increase in the horizontal total stress that occurs in this lower portion of the storage formation, which leads to an increase in the size of the Mohr circle (Fig. 7). The most critical point (point *C*) is placed around 0.5 m away from the damage zone. Even though a lower increase in the vertical total stress in point *C* with respect to point *D* leads to a smaller Mohr circle, the lower horizontal total stress increment leads to a Mohr circle that is closer to the yield surface.

Fig. 6b shows three additional points: a point in the fault core below the storage formation (point *E*), a point in the upper portion of the storage formation in the foot wall (point *F*), and a point in the fault core above the storage formation (point *G*). Two of these points (*F* and *G*) present almost no change in the mobilized friction angle. In point *E*, placed below the storage formation, the mobilized friction angle decreases initially, but it subsequently increases. This trend in the mobilized friction angle follows the same evolution as liquid pressure. Liquid pressure initially drops due to the reverse-water level fluctuation or Noordbergum effect (Hsieh, 1996; Vilarrasa et al., 2013a), but after some time, pressure diffuses through the low-permeable fault core and eventually causes pressure build-up, which is significantly lower than that occurring in the storage formation. The reverse-water level fluctuation is caused by deformation-induced pressure changes occurring in layers that overlay and underlay the formation where fluid is injected.

Fig. 8 displays the mobilized friction angle on a horizontal section that coincides with the middle of the portion of the storage formation that overlaps on both sides of the fault. The dotted line indicates the initial mobilized friction angle. Interestingly, despite the large overpressure induced by the presence of the low-permeable fault, increase in the mobilized friction angle is small around the injection well. Thus, caprock stability is maintained and its sealing capacity is not compromised. However, the mobilized friction angle varies significantly in the vicinity of the fault. Even though stability improves in the foot wall, the high mobilized friction angles in the hanging wall of the fault (higher than typical values of friction angle of geomaterials that are around 30°) suggest that shear failure is likely to occur in the fault.

3.2. CO_2 injection in the foot wall

When CO_2 is injected in the foot wall, overpressure and the induced total stress changes are very similar compared with those in the case of injection in the hanging wall, but occurring on the other side of the fault (Fig. 9). Since the fault has a 25 m-offset, the results are not exactly symmetric, though overpressure and total stress changes, both in vertical and horizontal directions, have similar magnitudes and distributions compared to those in the case of CO_2 injection in the hanging wall. The shear stress change has the same sign as in a normal faulting stress regime above the storage formation because now the rock above the storage formation in the foot wall is pushed upwards (Fig. 9e). Below the storage formation in the foot wall, which is pushed downwards, the shear stress changes have the opposite sign. In the upper half of the storage formation in the foot wall and in the portion of the caprock that is on the opposite side of the fault in the hanging wall, shear stress changes point upwards on both sides of the fault. In contrast, in the section of the storage formation that overlaps on both sides of the fault, shear stress changes point downwards on both sides of the fault.

The most critical region, when CO_2 is injected in the foot wall, takes place in the upper half of the storage formation in the foot wall close to the fault (Fig. 9f). Similarly to CO_2 injection in the hanging wall, stability also improves on the other side of the fault where CO_2 is injected. In this case, the maximum mobilized friction angle is slightly higher than that when CO_2 is injected in the hanging wall.

3.3. Effect of fault permeability on fault stability

To evaluate the effect of fault core permeability on fault stability, we also present the results of CO_2 injection in the hanging wall with the core permeability equal to 10^{-17} m^2, i.e. two orders of magnitude higher than that in the previous case, but still three orders of magnitude lower than that of the storage formation. A higher permeability of the fault core has a significant effect on pressure distribution (Fig. 10). First, the injection pressure for a constant mass injection rate becomes smaller than that for the less permeable fault. Second, the pressure gradient in the region between the injection well and the fault becomes higher for a more permeable fault core. This pressure distribution leads to a lower pressure on the fault in the hanging wall. Finally, the liquid flow across the fault core is non-negligible and causes pressure build-up on the foot wall (Fig. 11a).

The liquid pressure increase in the storage formation in the foot wall induces an increase in the horizontal total stresses there (Fig. 11b and d). Similar to the case with a less permeable fault core, the horizontal total stress in the direction perpendicular to the fault has a higher increase at the position close to the fault in the section of the storage formation that overlaps on both sides of the fault than that in the part coinciding with the base rock. Since the overpressure is lower than that in the case with a less permeable fault, the changes in the total stresses are also smaller. In this case, the shear stress changes are small, but present a clear pattern: the pressurized region of the fault, which mainly coincides with the storage formation on both sides of the fault, has a shear stress change that points upwards in the hanging wall and downwards in the foot wall (Fig. 11e). This change in the shear stress is caused by the expansion of the storage formation induced by CO_2 injection in the hanging wall and has opposite sign to the shear stress acting on a fault in a normal faulting stress regime.

Fig. 11f shows that the most critical zone is, like in the case of a fault core with lower permeability, the lower half of the storage formation in the hanging wall close to the fault. However, the increase in the mobilized friction angle is moderate in this case, which suggests that shear failure conditions may not be reached, at least for the time scale of this simulation. In spite of the pressure build-up in the foot wall, the mobilized friction angle decreases in

Please cite this article in press as: Vilarrasa V, et al., Geomechanical analysis of the influence of CO_2 injection location on fault stability, Journal of Rock Mechanics and Geotechnical Engineering (2016), http://dx.doi.org/10.1016/j.jrmge.2016.06.006

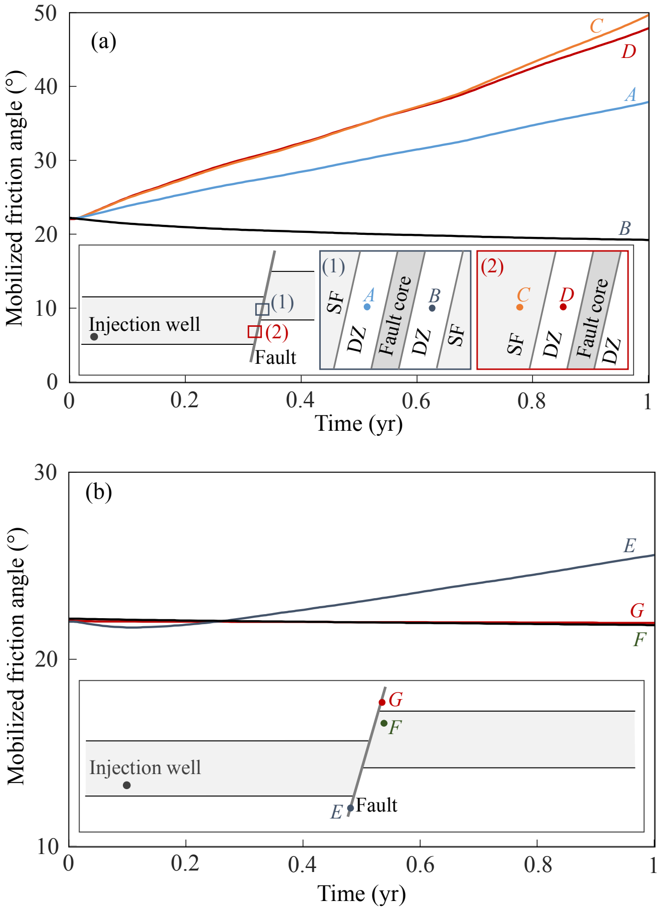

Fig. 6. Evolution of the mobilized friction angle at several points when injecting CO_2 in the hanging wall (a) in and close to the fault in the pressurized part of the storage formation and (b) below and above the storage formation and in the upper portion of the storage formation that is not pressurized. SF and DZ stand for storage formation and damage zone, respectively.

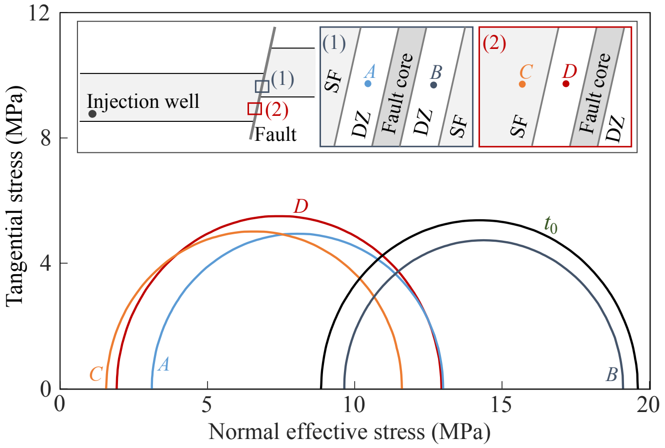

Fig. 7. Mohr circles before injection and after one year of injecting CO_2 in the hanging wall at several points. t_0 represents the initial stress state.

the section of the storage formation that overlaps on both sides of the fault. This is due to the mechanical effect that causes an increase in the horizontal total stress in the direction perpendicular to the fault in this region (Fig. 11b) that is higher than the decrease in effective stresses induced by overpressure (Fig. 11a). In contrast, the upper portion of the storage formation in the foot wall close to the fault experiences an increase in the mobilized friction angle. This decrease in stability is a result of the reduction in the effective stresses due to the overpressure and the negligible increase in the horizontal total stress in the direction perpendicular to the fault.

Fig. 12 compares the evolution of the mobilized friction angle resulting from a fault core of relatively high permeability (10^{-17} m^2) and one with lower permeability (10^{-19} m^2) at the same points as in Fig. 6. In the most critical zone, i.e. in the lower half of the storage formation in the hanging wall close to the fault (points *C* and *D*), the mobilized friction angle increases regardless of the fault core permeability. Nevertheless, the increase rate is higher for the case of a lower fault core permeability because the pressure builds up faster. In the section where the storage formation overlaps on both sides of the fault (points *A* and *B*), a more permeable fault core leads to a lower mobilized friction angle increase in the hanging wall (point *A*), for the same reason as in points *C* and *D*. On the other side of the fault, a lower decrease occurs in the foot wall (point *B*) because of the higher overpressure caused by the higher flow across the more permeable fault. The higher overpressure on the foot wall that occurs in the presence of a relatively permeable fault core leads to an increase in the mobilized friction angle in points *F* and *G*, which were not affected in the case with a lower permeability. Finally, in the fault core below the storage formation (point *E*), a similar trend as in the case of a lower permeability fault core occurs, but with a faster pressure diffusion. The faster pressurization of the fault core limits the reverse-water level fluctuation to a very limited time (a few days) and pore pressure increases rapidly, leading to a faster increase in the mobilized friction angle.

4. Discussion

Simulation results show that there are only small differences between injecting in the hanging wall and in the foot wall. The maximum mobilized friction angle is slightly higher when injecting in the foot wall than that in the hanging wall, which suggests that CO_2 injection in the former one is more critical than that in the latter one. Nevertheless, the differences are relatively small, so fault stability can be equally compromised if CO_2 is injected either in the hanging wall or in the foot wall. Therefore, the location of the injection well, either in the hanging wall or in the foot wall, should not be a critical factor in the design of fluid injection projects.

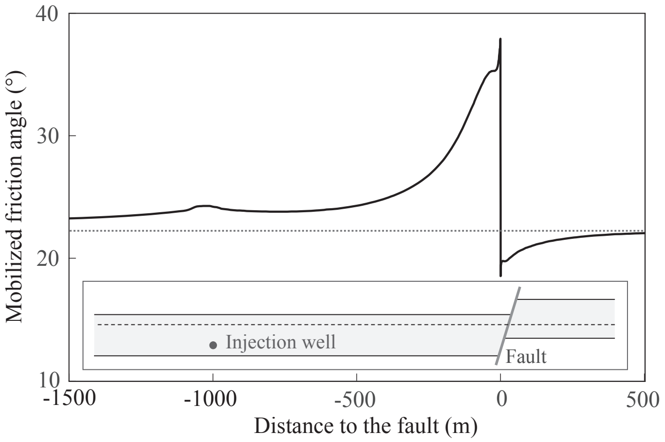

Fig. 8. Distribution of the mobilized friction angle after one year of CO_2 injection in the hanging wall, computed at a horizontal section that coincides with the middle portion of the storage formation that overlaps on both sides of the fault, as indicated by the dashed line in the inset.

Please cite this article in press as: Vilarrasa V, et al., Geomechanical analysis of the influence of CO_2 injection location on fault stability, Journal of Rock Mechanics and Geotechnical Engineering (2016), http://dx.doi.org/10.1016/j.jrmge.2016.06.006

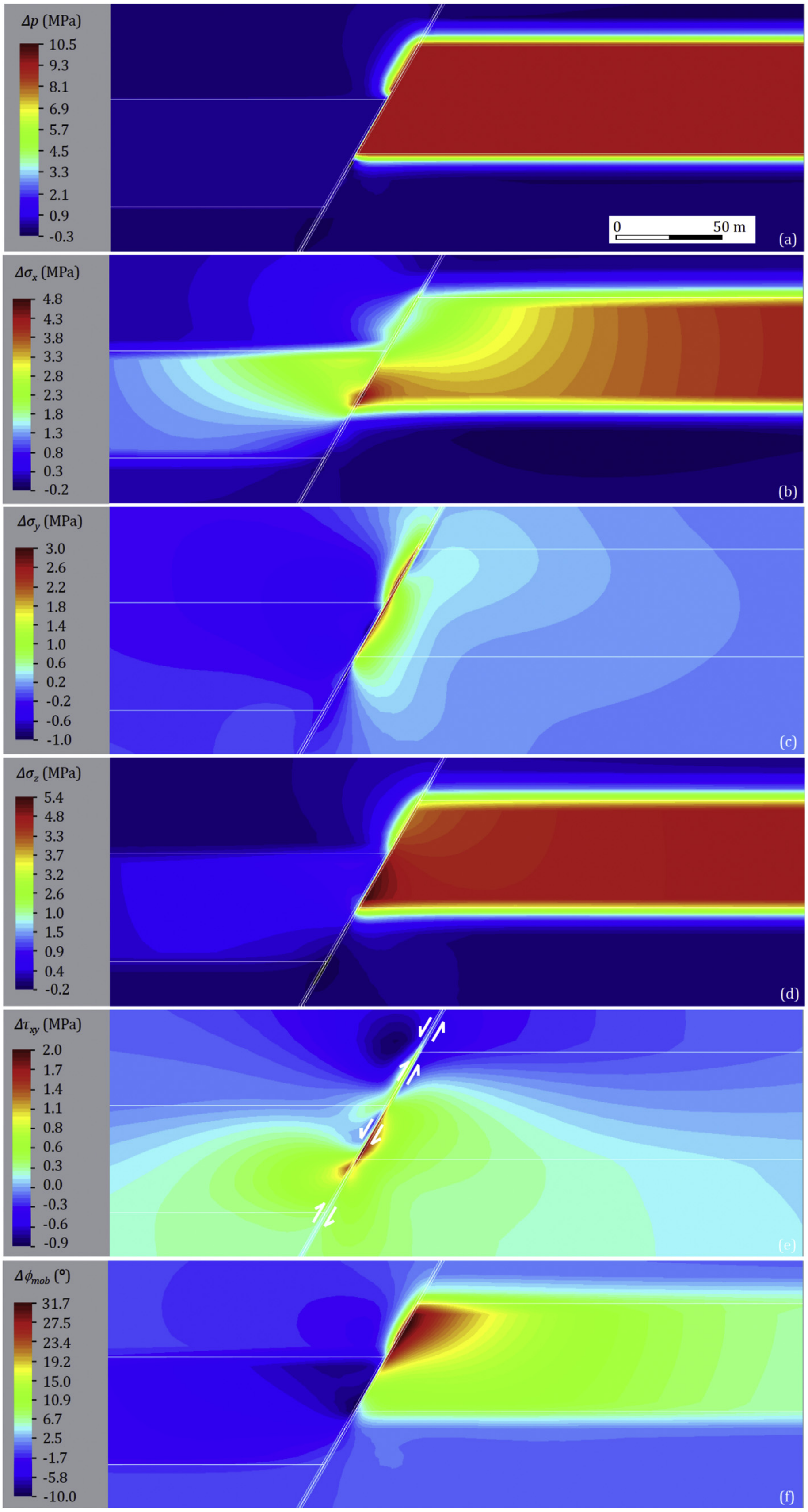

Fig. 9. Distribution of changes in (a) fluid pressure, (b) minimum horizontal total stress (in-plane), (c) vertical total stress, (d) maximum horizontal total stress (out-of-plane), (e) shear stress, and (f) mobilized friction angle after one year of injecting CO_2 in the foot wall.

Please cite this article in press as: Vilarrasa V, et al., Geomechanical analysis of the influence of CO_2 injection location on fault stability, Journal of Rock Mechanics and Geotechnical Engineering (2016), http://dx.doi.org/10.1016/j.jrmge.2016.06.006

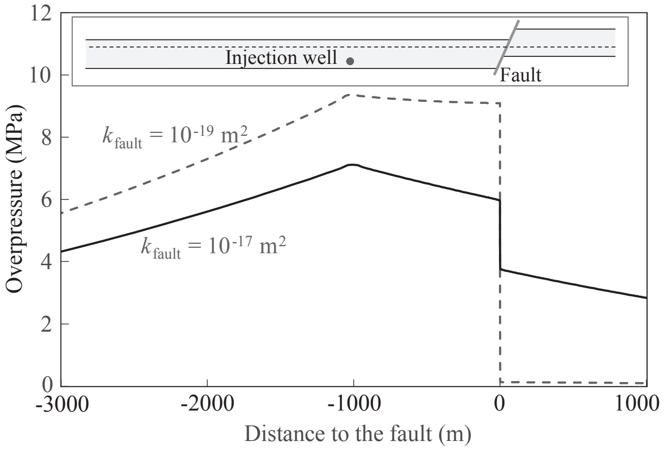

Fig. 10. Overpressure distribution after one year of CO_2 injection in the hanging wall of a fault with a fault core permeability of 10^{-17} m^2. For comparison, the induced overpressure for the case of the fault with a core permeability of 10^{-19} m^2 is shown. Overpressure is measured at the horizontal section coinciding with the middle portion of the storage formation that overlaps on both sides of the fault, as indicated by the dashed line in the inset.

However, identifying faults is crucial because their stability can be seriously affected (Fig. 8).

Faults cannot be avoided in compartmentalized reservoirs (Castelletto et al., 2013). Thus, they can be a limiting factor that can shorten the injection period, as reported in Snøhvit, Norway, where CO_2 injection had to be stopped after a few months due to an excessive overpressure induced by low-permeable faults (Hansen et al., 2013). As a result, injection wells should be located as far as possible from faults to minimize fault stability issues and avoid posing limitations on the injection rate. Nevertheless, the pressure perturbation cone will advance tens to hundreds of kilometers for the injection time scales expected in geologic carbon storage projects (Birkholzer et al., 2015). Hence, a proper pressure management will be required to minimize the risk of inducing felt seismic events (Vilarrasa and Carrera, 2015).

Unlike fault stability, which decreases as a result of CO_2 injection, caprock and storage formation stability away from the fault is not compromised (Fig. 8). In particular, the caprock remains stable around the injection well despite the large pressure build-up induced in the storage formation by the low-permeable fault. Hence, the caprock sealing capacity will be maintained and thus, no CO_2 leakage will occur. The injection rate and overpressure (close to 10 MPa) of our simulation are similar to those at In Salah in Algeria, where no CO_2 leakage across the caprock has been detected (Rutqvist, 2012). Furthermore, CO_2 is pushed away from the fault due to the higher overpressure between the fault and the injection well compared to the other side of the injection well where no fault is present. This trajectory of the CO_2 plume has been observed in the field at Ketzin, Germany (Chen et al., 2014). Thus, the CO_2 plume may not reach low-permeable faults, which could be the only potential migration path for CO_2 if a fault was reactivated. Still, this possibility is remote, because clay-rich materials, like a fault that crosses a clay-rich rock, tend to maintain low-permeability and high entry pressure despite shear slip accumulation (Laurich et al., 2014). In the eventual case of the CO_2 plume reaching the fault, the pore pressure in the fault will be almost equal to CO_2 pressure. Thus, the CO_2-rich phase will not easily flow through extensional faults due to their multi-phase flow properties (Fisher and Knipe, 2001).

The fault considered in this study corresponds to a conduit-barrier fault in the section crossing the reservoir (Caine et al., 1996). However, the conduit does not have continuity across the confining layers due to the fault heterogeneity (Rinaldi et al., 2014). Though the type of fault that we model is typical for sedimentary formations with alternating layers of clastic and clay-rich materials (Egholm et al., 2008), different lithology and geologic histories can lead to different fault structures (Faulkner et al., 2010). For example, the presence of a very stiff caprock, with low clay content and thus being brittle, may lead to permeability enhancement if fault reactivation occurs. But even with the fault structure considered here, differences in the degree of calcite cementation of the damage zone (Alikarami et al., 2013), or dissymmetry in the internal structure of the damage zone (Rohmer, 2014; Rohmer et al., 2014), may produce different geomechanical responses of the fault. Thus, subsurface uncertainty may play a relevant role in fault stability assessment (Pereira et al., 2014; Wei et al., 2015).

In this study, we assume brittle behavior of rock, i.e. elastic deformation up to failure. This is the least conservative situation, because for storage formation, fault, and caprock representatives, quasi-brittle or even ductile behavior is common at typical geologic carbon storage stress states (e.g. Popp and Salzer, 2007; Makhnenko and Labuz, 2015). This ductile behavior implies rock yielding before failure. Thus, between the onset of yield and the failure of the rock, a transition zone in which both elastic and plastic strains occur may allow accumulating large strain without inducing large stresses. Additionally, the dilatancy of the storage formation (Makhnenko and Labuz, 2015), the confining layers (e.g. Popp and Salzer, 2007), or the fault-forming material (Parry and Bruhn, 1990) would lead to pore pressure reduction. Furthermore, dilatant hardening may arrest the rupture, especially for the case of confining layers, where undrained deformation occurs.

Since we are assuming only elastic deformation, the mobilized friction angle reaches values above the actual friction angle typical of the rock types considered in the model, i.e. 30°. These high mobilized friction angles are due to the fact that no pressure management is carried out during the simulations. However, it permits identifying which is the most critical zone around the fault. The highest mobilized friction angle takes place in the pressurized region of the storage formation, around 0.5 m away from the damage zone. This observation may be correlated with the fact that the damage zone of faults tends to increase as shear slip events accumulate (Billi et al., 2003). If the most critical zone is located outside the fault, the rock there may fail and widen the thickness of the damage zone. However, this is not a straightforward process, since the friction angle of intact rock is higher than that of failed rock and therefore, the fault is more likely to fail earlier than the intact rock. Furthermore, once failure occurs, stresses are released and the mobilized friction angle is reduced around the fault. Thus, rock around the fault would not reach failure conditions despite the large values of mobilized friction angles observed on both sides of the fault (see Fig. 5).

The shear stress changes that occur in the fault have, in general, the opposite sign to the shear stress acting on the fault plane due to the regional normal faulting stress regime, especially when injecting in the hanging wall (Fig. 11e). This orientation of the shear stress increments is due to the fact that CO_2 injection causes the expansion of the storage formation. If CO_2 is injected in the hanging wall, the expansion pushes the upper half of the hanging wall upwards (contrary to the regional stress state) and the lower part downwards (in the same direction as the regional stress state) (Fig. 4e). On the other hand, if CO_2 is injected in the foot wall, the expansion pushes the upper half of the foot wall upwards (in the same direction as the regional stress state) and the lower part downwards (contrary to the regional stress state) (Fig. 9e). However, if shear failure conditions are reached in the fault, inelastic strain will bring the hanging wall downwards and the foot wall

Please cite this article in press as: Vilarrasa V, et al., Geomechanical analysis of the influence of CO_2 injection location on fault stability, Journal of Rock Mechanics and Geotechnical Engineering (2016), http://dx.doi.org/10.1016/j.jrmge.2016.06.006

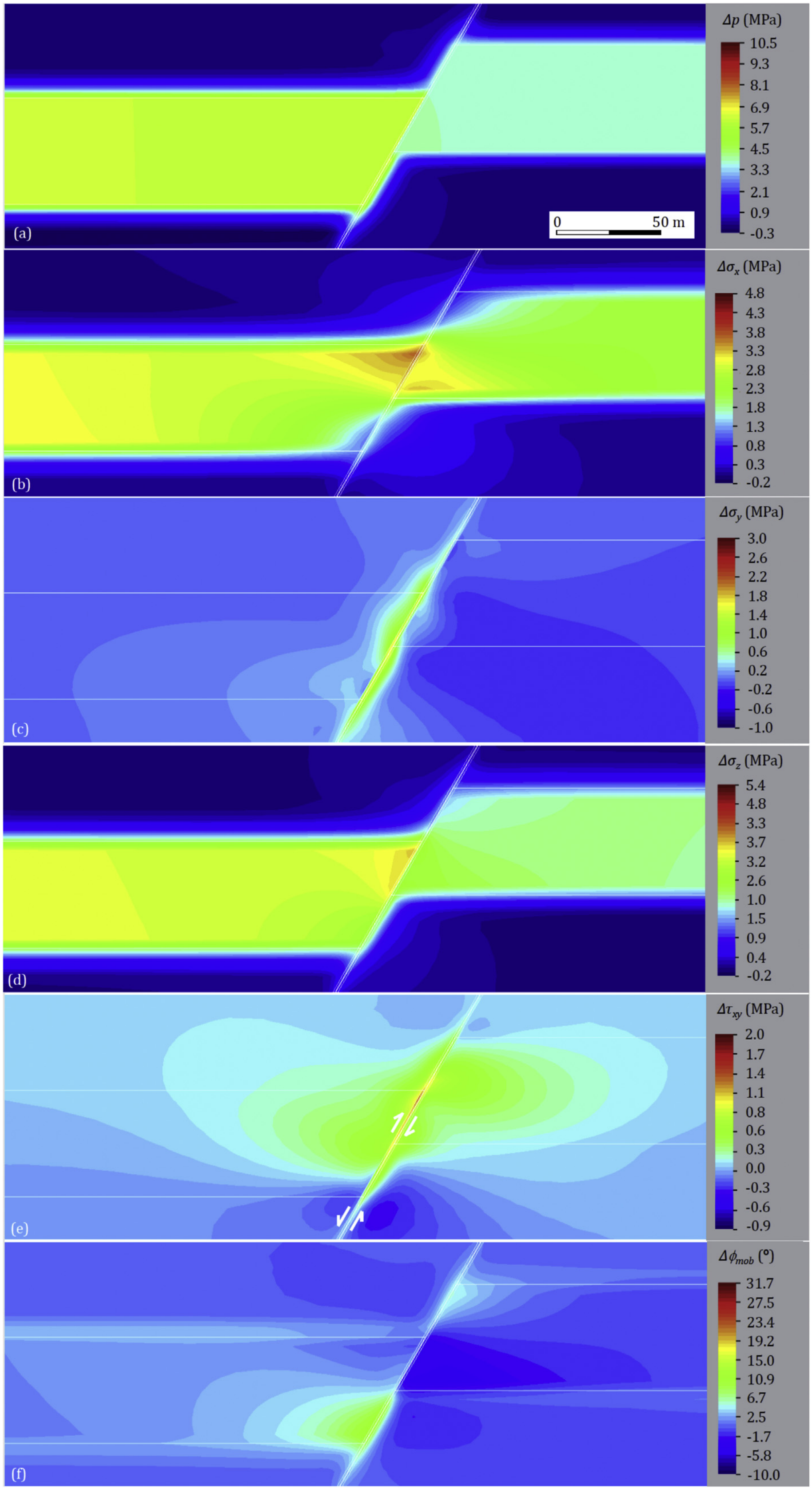

Fig. 11. Distribution of changes in (a) fluid pressure, (b) minimum horizontal total stress (in-plane), (c) vertical total stress, (d) maximum horizontal total stress (out-of-plane), (e) shear stress, and (f) mobilized friction angle after one year of injecting CO_2 in the hanging wall when the permeability of the fault core is of 10^{-17} m^2 (two orders of magnitude more permeable than that of the base case).

Please cite this article in press as: Vilarrasa V, et al., Geomechanical analysis of the influence of CO_2 injection location on fault stability, Journal of Rock Mechanics and Geotechnical Engineering (2016), http://dx.doi.org/10.1016/j.jrmge.2016.06.006

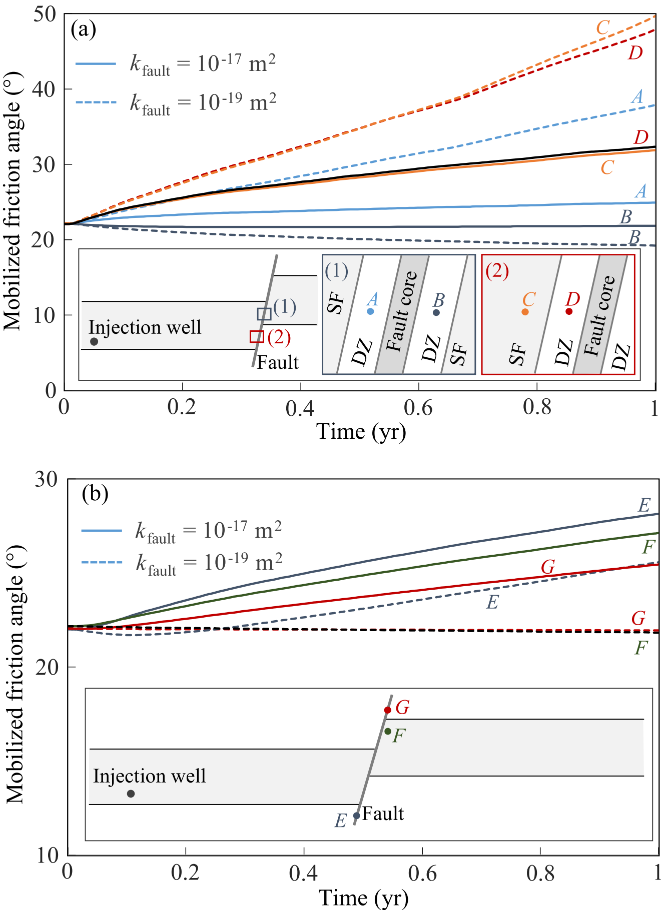

Fig. 12. Evolution of the mobilized friction angle at several points when injecting CO_2 in the hanging wall for a fault core permeability of 10^{-17} m^2 (the results for a fault core permeability of 10^{-19} m^2, in dashed lines, are shown for comparison) (a) in and close to the fault in the pressurized part of the storage formation and (b) below and above the storage formation and in the upper portion of the storage formation that is not pressurized.

upwards, because the shear stress acting on the fault due to the regional stress state is much larger than the shear stress changes induced by CO_2 injection.

Fault stability is mainly controlled, in our model, by the offset of the fault. The difference in the stiffness between the storage formation and the caprock and base rock, of one order of magnitude, leads to non-homogeneous total stress changes around the fault, which significantly affect its stability. In the case of a larger fault offset when only base rock or caprock is present on the other side of the fault, the storage formation around the fault would undergo a smaller increase in the horizontal total stress in the direction perpendicular to the fault. This may lead to unstable conditions due to the high deviatoric stress and reduced normal effective stress, i.e. the Mohr circle maintains its size and is displaced towards the failure envelope (Orlic and Wassing, 2013). In contrast, in the case of a small fault offset, which would imply having the storage formation on both sides of the fault, the horizontal total stress in the direction perpendicular to the fault would increase significantly around the fault due to the high stiffness of the storage formation. As a result, the size of the Mohr circle would become smaller, which would help to maintain fault stability (Gheibi et al., 2016). The changes in the vertical total stress are more difficult to be predicted without actually simulating these scenarios, but in principle, the stiffer the rock on the other side of the fault, the higher the increase in the total vertical stress. Nevertheless, vertical stress changes are smaller than horizontal stress changes, so they have less effect on fault stability.

Fault stability is also controlled by other factors, such as the initial stress state, fault dip and geometry of the storage formation. We have considered an initial stress state typical of sedimentary formations, which are usually not critically stressed and thus, a certain overpressure can be induced without reaching failure conditions (Vilarrasa and Carrera, 2015). However, initial stress states that are close to failure conditions, like that occurring in the crystalline basement, lead to fault reactivation for small overpressures (Figueiredo et al., 2015) and have the potential to induce larger earthquakes for a given injection rate (Cappa and Rutqvist, 2011a). We have considered a critically oriented fault in a normal faulting stress regime for a fault with a typical friction angle of 30°. Even though fault reactivation is possible in faults that are not critically oriented, a fault dip different from the considered one would have required a larger overpressure to reach shear failure conditions. As for the geometry of the storage formation, a thicker storage formation would lead to a higher transmissivity. Thus, the effect would be similar to that of a higher permeability or a lower injection rate. In all these cases, pressure build-up would have been slower, so failure conditions would have been reached at a later injection time.

For the considered injection mass flow rate, shear failure conditions are reached within the first year of CO_2 injection for the cases with a fault core permeability of 10^{-19} m^2. However, for the case of a fault core permeability of 10^{-17} m^2, the fault may remain stable, at least during the first year of injection. Thus, one could imagine the possibility that if a reactivation of a low-permeable fault occurs and leads to an increase in fault permeability by several orders of magnitude, the fault may remain stable afterwards even though the same injection rate is maintained. Nevertheless, fault permeability may not experience a significant increase after its reactivation in clay-rich formations (Laurich et al., 2014). In fact, we have experimentally observed that even if failure of clay-rich caprock and base rock representative (shale) or fault core material (remolded shale) occurs, the overall change in void ratio that contributes to the flow does not exceed 2% (see also Popp and Salzer, 2007). This increase in void ratio provides less than an order of magnitude increase in fault permeability, which, as shown in Section 3.3, leads to a smaller effect on its stability. Still, the safety of the storage procedure may be compromised if fluid pressure exceeds the maximum sustainable injection pressure. Thus, the overall safety of geologic storage projects, in terms of the possibility of CO_2 leakage through the fault or the caprock, is subjected to proper monitoring and pressure management.

5. Conclusions

Injection of CO_2 either in the hanging wall or in the foot wall has a very similar effect on fault stability changes. Simulation results show that the stress changes that occur around the fault as a result of CO_2 injection cause a significant reduction in fault stability. However, both the storage formation and the caprock remain stable at relatively short distances from the fault. Despite the large pressure build-up that takes place between the injection well and the fault, caprock stability around the injection well is not compromised and thus, its sealing capacity is maintained, so CO_2 leakage will not occur. The most critical zone occurs around 0.5 m outside the fault, which may result in the widening of the damage zone. We find that the permeability of the fault core has a significant influence on fault stability. The lower the fault core permeability is, the higher the induced overpressure and stress changes are. Thus, less permeable faults lead to less stable situations. Overall, pressure management should be performed to minimize the risk of inducing felt seismic events.

Please cite this article in press as: Vilarrasa V, et al., Geomechanical analysis of the influence of CO_2 injection location on fault stability, Journal of Rock Mechanics and Geotechnical Engineering (2016), http://dx.doi.org/10.1016/j.jrmge.2016.06.006

Conflict of interest

The authors wish to confirm that there are no known conflicts of interest associated with this publication and there has been no significant financial support for this work that could have influenced its outcome.

Acknowledgements

The first author acknowledges the support from the “EPFL Fellows” fellowship program co-funded by Marie Curie, FP7 (Grant No. 291771) and partial support from the “TRUST” project of the European Community’s Seventh Framework Programme FP7/2007–2013 (Grant No. 309607) and the “FracRisk” project of the European Community’s Horizon 2020 Framework Programme H2020-EU.3.3.2.3 (Grant No. 640979). Activities of the second author are sponsored by SCCER-SoE (Switzerland) (Grant No. KTI.2013.288) and Swiss Federal Office of Energy (SFOE) project CAPROCK (Grant No. 810008154). This publication has also been produced with partial support from the BIGCCS Centre (for the third author), performed under the Norwegian research program Centers for Environment-friendly Energy Research (FME). The third author acknowledges the following partners for their contributions: Gassco, Shell, Statoil, TOTAL, ENGIE, and the Research Council of Norway (193816/S60).

References

Alikarami R, Torabi A, Kolyukhin D, Skurtveit E. Geostatistical relationships between mechanical and petrophysical properties of deformed sandstone. International Journal of Rock Mechanics and Mining Sciences 2013;63:27–38.

Bear J. Dynamics of fluids in porous media. New York: Elsevier; 1972.

Bennion B, Bachu S. Drainage and imbibition relative permeability relation-ships for supercritical CO_2/brine and H_2S/brine systems in intergranular sandstone, carbonate, shale, and anhydrite rocks. SPE Reservoir Evaluation & Engineering 2008;11(3):487–96.

Billi A, Salvini F, Storti F. The damage zone-fault core transition in carbonate rocks: implications for fault growth, structure and permeability. Journal of Structural Geology 2003;25(11):1779–94.

Birkholzer JT, Zhou Q, Tsang CF. Large-scale impact of CO_2 storage in deep saline aquifers: a sensitivity study on pressure response in stratified systems. International Journal of Greenhouse Gas Control 2009;3(2):181–94.

Birkholzer JT, Oldenburg CM, Zhou Q. CO_2 migration and pressure evolution in deep saline aquifers. International Journal of Greenhouse Gas Control 2015;40:203–20.

Byerlee JD. Friction of rocks. Pure and Applied Geophysics 1978;116(4):615–26.

Caine JS, Evans JP, Forster CB. Fault zone architecture and permeability structure. Geology 1996;24(11):1025–8.

Cappa F, Rutqvist J. Impact of CO_2 geological sequestration on the nucleation of earthquakes. Geophysical Research Letters 2011a;38(17). http://dx.doi.org/10.1029/2011GL048487.

Cappa F, Rutqvist J. Modeling of coupled deformation and permeability evolution during fault reactivation induced by deep underground injection of CO_2. International Journal of Greenhouse Gas Control 2011b;5(2):336–46.

Cappa F, Rutqvist J. Seismic rupture and ground accelerations induced by CO_2 injection in the shallow crust. Geophysical Journal International 2012;190(3):1784–9.

Castelletto N, Gambolati G, Teatini P. Geological CO_2 sequestration in multi-compartment reservoirs: geomechanical challenges. Journal of Geophysical Research: Solid Earth 2013;118(5):2417–28.

Cesca S, Grigoli F, Heimann S, González Á, Buforn E, Maghsoudi S, Blanch E, Dahm T. The 2013 September–October seismic sequence offshore Spain: a case of seismicity triggered by gas injection? Geophysical Journal International 2014;198(2):941–53.

Chen F, Wiese B, Zhou Q, Kowalsky MB, Norden B, Kempka T, Birkholzer JT. Numerical modeling of the pumping tests at the Ketzin pilot site for CO_2 injection: model calibration and heterogeneity effects. International Journal of Greenhouse Gas Control 2014;22:200–12.

Detournay E, Cheng AHD. Fundamentals of poroelasticity. In: Comprehensive rock engineering: principles, practice and projects. Analysis and design method. New York: Pergamon Press; 1993. p. 113–71.

Egholm DL, Clausen OR, Sandiford M, Kristensen MB, Korstgård JA. The mechanics of clay smearing along faults. Geology 2008;36(10):787–90.

Ellsworth WL. Injection-induced earthquakes. Science 2013;341(6142). http://dx.doi.org/10.1126/science.1225942.

Faulkner DR, Jackson CAL, Lunn RJ, Schlische RW, Shipton ZK, Wibberley CAJ, Withjack MO. A review of recent developments concerning the structure, mechanics and fluid flow properties of fault zones. Journal of Structural Geology 2010;32(11):1557–75.

Figueiredo B, Tsang CF, Rutqvist J, Bensabat J, Niemi A. Coupled hydro-mechanical processes and fault reactivation induced by CO_2 injection in a three-layer storage formation. International Journal of Greenhouse Gas Control 2015;39:432–48.

Fisher QJ, Knipe RJ. The permeability of faults within siliciclastic petroleum reservoirs of the North Sea and Norwegian Continental Shelf. Marine and Petroleum Geology 2001;18(10):1063–81.

Fuss S, Canadell JG, Peters GP, Tavoni M, Andrew RM, Ciais P, Jackson RB, Jones CD, Kraxner F, Nakicenovic N, Le Quéré C, Raupach MR, Sharifi A, Smith P, Yamagata Y. Betting on negative emissions. Nature Climate Change 2014;4(10):850–3.

Gheibi S, Holt R, Vilarrasa V. Stress path evolution during fluid injection into geological formations. In: The 50th US Rock Mechanics/Geomechanics Symposium, Houston, USA. American Rock Mechanics Association; 2016. Paper 16–614.

Hansen O, Gilding D, Nazarian B, Osdal B, Ringrose P, Kristoffersen JB, Eiken O, Hansen H. Snøhvit: the history of injecting and storing 1 Mt CO_2 in the Fluvial Tubåen Fm. Energy Procedia 2013;37:3565–73.

Horton S. Disposal of hydrofracking waste fluid by injection into subsurface aquifers triggers earthquake swarm in central Arkansas with potential for damaging earthquake. Seismological Research Letters 2012;83(2):250–60.

Hsieh PA. Deformation-induced changes in hydraulic head during ground-water withdrawal. Ground Water 1996;34(6):1082–9.

Häring MO, Schanz U, Ladner F, Dyer BC. Characterisation of the Basel 1 enhanced geothermal system. Geothermics 2008;37(5):469–95.

International Energy Agency (IEA). Energy technology perspectives. Scenarios & strategies to 2050. Executive summary. IEA; 2010.

Laurich B, Urai JL, Desbois G, Vollmer C, Nussbaum C. Microstructural evolution of an incipient fault zone in Opalinus Clay: insights from an optical and electron microscopic study of ion-beam polished samples from the Main Fault in the Mt-Terri Underground Research Laboratory. Journal of Structural Geology 2014;67:107–28.

Makhnenko RY, Labuz JF. Dilatant hardening of fluid-saturated sandstone. Journal of Geophysical Research: Solid Earth 2015;120(2):909–22.

Makhnenko RY, Labuz JF. Elastic and inelastic deformation of fluid-saturated rock. Philosophical Transactions of the Royal Society A: Mathematical, Physical & Engineering Sciences 2016. http://dx.doi.org/10.1098/rsta.2015.0422.

Mazzoldi A, Rinaldi AP, Borgia A, Rutqvist J. Induced seismicity within geological carbon sequestration projects: maximum earthquake magnitude and leakage potential from undetected faults. International Journal of Greenhouse Gas Control 2012;10:434–42.

Oldenburg CM. The risk of induced seismicity: is cap-rock integrity on shaky ground? Greenhouse Gases: Science and Technology 2012;2(4):217–8.

Olivella S, Carrera J, Gens A, Alonso EE. Non-isothermal multiphase flow of brine and gas through saline media. Transport in Porous Media 1994;15(3):271–93.

Olivella S, Gens A, Carrera J, Alonso EE. Numerical formulation for a simulator (CODE_BRIGHT) for the coupled analysis of saline media. Engineering Computations 1996;13(7):87–112.

Orlic B, Wassing BBT. A study of stress change and fault slip in producing gas reservoirs overlain by elastic and viscoelastic caprocks. Rock Mechanics and Rock Engineering 2013;46(3):421–35.

Pan PZ, Rutqvist J, Feng XT, Yan F. Modeling of caprock discontinuous fracturing during CO_2 injection into a deep brine aquifer. International Journal of Greenhouse Gas Control 2013;19:559–75.

Pan PZ, Rutqvist J, Feng XT, Yan F. An approach for modeling rock discontinuous mechanical behavior under multiphase fluid flow conditions. Rock Mechanics and Rock Engineering 2014;47(2):589–603.

Parry WT, Bruhn RL. Fluid pressure transients on seismogenic normal fault. Tectonophysics 1990;179(3–4):335–44.

Pereira LC, Guimarães LJN, Horowitz B, Sánchez M. Coupled hydro-mechanical fault reactivation analysis incorporating evidence theory for uncertainty quantification. Computers and Geotechnics 2014;56:202–15.

Popp T, Salzer K. Anisotropy of seismic and mechanical properties of Opalinus Clay during triaxial deformation in a multi-anvil apparatus. Physics and Chemistry of the Earth, Parts A/B/C 2007;32(8–14):879–88.

Rinaldi AP, Jeanne P, Rutqvist J, Cappa F, Guglielmi Y. Effects of fault-zone architecture on earthquake magnitude and gas leakage related to CO_2 injection in a multi-layered sedimentary system. Greenhouse Gases: Science and Technology 2014;4(1):99–120.

Rinaldi AP, Vilarrasa V, Rutqvist J, Cappa F. Fault reactivation during CO_2 sequestration: effects of well orientation on seismicity and leakage. Greenhouse Gases: Science and Technology 2015;5(5):645–56.

Rohmer J. Induced seismicity of a normal blind undetected reservoir-bounding fault influenced by dissymmetric fractured damage zones. Geophysical Journal International 2014;197(1):636–41.

Rohmer J, Allanic C, Bourgine B, Sulem J, Suhett-Helmer G, Ghabezloo S, Pouya A, Renard F, Beucher H, Mehl C, Siavelis M, Tardieu N. Improving our knowledge on the hydro-chemo-mechanical behaviour of fault zones in the context of CO_2 geological storage. Energy Procedia 2014;63:3371–8.

Rutqvist J. The geomechanics of CO_2 storage in deep sedimentary formations. Geotechnical and Geological Engineering 2012;30(3):525–51.

Please cite this article in press as: Vilarrasa V, et al., Geomechanical analysis of the influence of CO_2 injection location on fault stability, Journal of Rock Mechanics and Geotechnical Engineering (2016), http://dx.doi.org/10.1016/j.jrmge.2016.06.006

Streit JE, Hillis RR. Estimating fault stability and sustainable fluid pressures for underground storage of CO_2 in porous rock. Energy 2004;29(9–10):1445–56.
Szulczewski ML, MacMinn CW, Herzog HJ, Juanes R. Lifetime of carbon capture and storage as a climate-change mitigation technology. Proceedings of the National Academy of Sciences of the United States of America 2012;109(14):5185–9.
Verdon JP. Significance for secure CO_2 storage of earthquakes induced by fluid injection. Environmental Research Letters 2014;9(6):064022.
Vidal-Gilbert S, Tenthorey E, Dewhurst D, Ennis-King J, Van Ruth P, Hillis R. Geomechanical analysis of the Naylor Field, Otway Basin, Australia: implications for CO_2 injection and storage. International Journal of Greenhouse Gas Control 2010;4(5):827–39.
Vilarrasa V, Carrera J, Olivella S. Hydromechanical characterization of CO_2 injection sites. International Journal of Greenhouse Gas Control 2013a;19:665–77.
Vilarrasa V, Silva O, Carrera J, Olivella S. Liquid CO_2 injection for geological storage in deep saline aquifers. International Journal of Greenhouse Gas Control 2013b;14:84–96.
Vilarrasa V, Olivella S, Carrera J, Rutqvist J. Long term impacts of cold CO_2 injection on the caprock integrity. International Journal of Greenhouse Gas Control 2014;24:1–13.
Vilarrasa V, Carrera J. Geologic carbon storage is unlikely to trigger large earthquakes and reactivate faults through which CO_2 could leak. Proceedings of the National Academy of Sciences of the United States of America 2015;112(19):5938–43.
Wei XC, Li Q, Li XY, Sun YK, Liu XH. Uncertainty analysis of impact indicators for the integrity of combined caprock during CO_2 geosequestration. Engineering Geology 2015;196:37–46.
Zhou Q, Birkholzer JT. On scale and magnitude of pressure build-up induced by large-scale geologic storage of CO_2. Greenhouse Gases: Science and Technology 2011;1(1):11–20.
Zoback MD, Gorelick SM. Earthquake triggering and large-scale geologic storage of carbon dioxide. Proceedings of the National Academy of Sciences of the United States of America 2012;109(26):10164–8.

Victor Vilarrasa obtained M.S. and Ph.D. degrees from the Technical University of Catalonia (UPC), Barcelona, Spain. He was a postdoctoral fellow at the Earth and Environmental Sciences Area at the Lawrence Berkeley National Laboratory (LBNL), Berkeley, USA and was awarded with an 'EPFL Fellows' Fellowship co-funded by Marie Curie at the École Polytechnique Fédérale de Lausanne, Switzerland. He is now staff scientist at the Institute of Environmental Assessment and Water Research, Spanish National Research Council (IDAEA-CSIC). His research, developed in several European and US research projects, deals with dimensional analysis and modeling of coupled thermo-hydro-mechanical-chemical (THMC) processes related to geo-energy and geo-engineering applications. He applies his research to several geo-energy and geo-engineering applications, such as CO_2 geologic storage, geologic nuclear waste disposal and enhanced geothermal systems. He has given several invited talks at conferences and seminars, including universities such as Stanford University, Swiss Federal Institute of Technology Zurich (ETHZ) and the Royal Institute of Technology (KTH), and research institutes such as the US Geologic Survey (USGS) and LBNL. He serves as a reviewer in many geoscience journals. Up to now he has received the Special Doctoral Award of the UPC, the Alfons Bayó Award to Young Researchers awarded by the International Association of Hydrogeologists (IAH) – Spanish Group, and the MIT Technology Review Award to Innovators Under 35.

Please cite this article in press as: Vilarrasa V, et al., Geomechanical analysis of the influence of CO_2 injection location on fault stability, Journal of Rock Mechanics and Geotechnical Engineering (2016), http://dx.doi.org/10.1016/j.jrmge.2016.06.006

Available online at www.sciencedirect.com

ScienceDirect

Energy Procedia 00 (2017) 000–000

Energy Procedia

www.elsevier.com/locate/procedia

13th International Conference on Greenhouse Gas Control Technologies, GHGT-13, 14-18 November 2016, Lausanne, Switzerland

Hydromechanical aspects of CO_2 breakthrough into clay-rich caprock

R.Y. Makhnenko[a,b], V. Vilarrasa[a,c], D. Mylnikov[a], L. Laloui[a]

[a]Laboratory of Soil Mechanics, École Polytechnique Fédérale de Lausanne, EPFL ENAC IIC LMS, GC – Station 18, CH-1015 Lausanne, Switzerland

[b]Department of Civil & Environmental Engineering, University of Illinois at Urbana-Champaign, 205 North Mathews Ave, Urbana, IL, 61801-2352, USA

[c]Institute of Environmental Assessment and Water Research, Spanish National Research Council (IDAEA-CSIC), Jordi Girona 18-26, 08034 Barcelona, Spain

---

Abstract

Caprock formations are intended to prevent upwards carbon dioxide (CO_2) migration to the surface during CO_2 geological storage. Caprock interaction with CO_2, as well as its potential consequences, requires to be predicted, and thus, need to be studied experimentally. Laboratory investigations of caprock behavior are complex due to its low permeability, and the scarcity of experimental studies involving high-pressure CO_2 injection into caprock representatives puts this difficulty into manifest. In this study, we perform laboratory experiments in an oedometric cell on intact and remolded Opalinus clay (Jurassic shale), evaluating the breakthrough pressure and permeability for liquid and supercritical CO_2. Intact and remolded shale specimens present intrinsic permeabilities of 10^{-21} m^2 to 10^{-20} m^2, respectively. Applied axial stress ranges from 27 MPa to 42 MPa and the pressure and temperature conditions are representative of a caprock at a depth of 800 m. We found that the microstructure of the caprock has a great effect on the material properties. The intrinsic permeability of a more tight material (intact Opalinus clay) is around two times lower than that of remolded shale, which has a more open microstructure. Additionally, the intact rock becomes 30 times less permeable to CO_2 than the remolded shale, which implies that the CO_2 relative permeability is 15 times smaller for intact rock than for remolded shale. On the other hand, CO_2 breakthrough pressure for the tighter material is almost three times lower than for the more permeable remolded shale. Breakthrough pressure of the remolded shale ranges from 3.9 MPa to 5.0 MPa for liquid CO_2 and from 2.8 MPa to 4.6 MPa for supercritical CO_2. For the intact shale, breakthrough pressure is 0.9 MPa for liquid CO_2 and 1.6 MPa for supercritical CO_2. Thus, the breakthrough pressure cannot be correlated with the intrinsic permeability of the caprock.

Keywords: Caprock; shale; liquid and supercritical CO_2; breakthrough pressure; permeability.

---

1. Introduction

The main function of a caprock within carbon dioxide (CO_2) geological storage systems is preventing or minimizing CO_2 leakage to the surface within the timescale of permanent storage projects, i.e., in the order of tens of thousands of years. However, the buoyancy of CO_2, combined with its acidity and potential thermo-mechanical effects, may lead to CO_2 leakage across the caprock. For example, during the first three years of operation at the Sleipner field storage project in the North Sea (Norway), CO_2 propagated upwards through several thin caprock barriers with a total thickness of 17 meters [1]. Furthermore, there are reported cases of naturally accumulated CO_2 invading caprock formations even at relatively small overpressures [e.g., 2, 3]. Since high pressure and large areal extent of CO_2 plumes are expected in industrial scale projects, the risk of CO_2 propagation into the seal increases. In order to plan geological storage projects properly and to perform risk assessment associated with CO_2 propagation through the caprock, the International Energy Agency [4] suggests that each formation should be investigated in terms of its properties (geomechanical and petrophysical) evolution due to interaction with CO_2.

Shales and mudstones are the most typical caprock formations for current and potential CO_2 storage sites due to their low permeability and wide spread in the Earth crust [5]. Existing studies on clay-rich materials' interactions with CO_2 show significant effect of chemical reactions on rock properties and mineral composition [6]. Dissolution of carbonate and feldspar minerals within shales is reported, as well as further secondary carbonate precipitation [7]. While self-sealing caused by CO_2 flow occurs in some occasions due to porosity decrease [e.g., 8] or clogging of fractures [9], other studies show increase of permeability and amount of large pores (> 1 μm) due to interaction with CO_2 [10, 11].

Apart from geochemical reactions, cooling of the lower portion of the caprock may occur [12, 13]. Cooling is likely to be common because injecting CO_2 in liquid state is energetically more efficient than doing so in supercritical state (pressure > 7.382 MPa and T > 31.04 ˚C). It is also more optimal from a storage engineering point of view because liquid CO_2 is denser than supercritical CO_2 [14]. As a result, for a given mass of CO_2, a smaller volume of formation fluid will be displaced leading to a lower overpressure in the reservoir and the increased weight of liquid CO_2 in the injection well implies that a far lower pressure is required at the wellhead. On the other hand, CO_2 will generally reach the storage formation at a colder temperature than that corresponding to the geothermal gradient, because it does not thermally equilibrate with the surrounding rock as it flows downwards along the injection well [15]. The colder CO_2 will form a cooler region around the injection well that advances much behind the desaturation front [12] and that will cool down the caprock by conduction [16]. Moreover, in the case of continuous industrial scale injection, the temperature at which CO_2 enters into the storage formation may be significantly lower than that of the surrounding rock [14, 17]. Hence, strong cooling of the caprock is likely to occur near-the-wellbore and CO_2-caprock interaction should also be studied at temperatures below 31˚C (Fig. 1).

The overarching goal of this study is to identify the main challenges for the caprock integrity (e.g., temperature and chemical effects, long-term permeability, strength evolution) and to study them experimentally for a caprock representative. In this paper, we concentrate on injection of CO_2 inside low-permeable clayey specimens and discuss relative permeability to brine and CO_2 and CO_2 breakthrough pressure. After a brief background section, we introduce the properties of tested materials, experimental setup, and methods, and then provide results, discuss them, and conclude with projections for further studies.

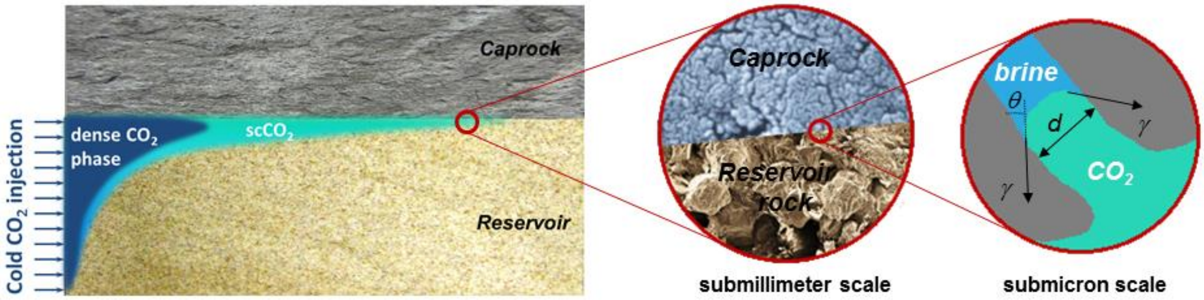

Figure 1. Sketch of CO_2 injection in reservoir rock and its trapping under caprock formation; $scCO_2$ stands for supercritical CO_2.

2. Background

Geomechanical response of a caprock to CO_2 injection involves studying processes that affect elastic and inelastic rock properties and evolution of porosity-permeability relationship [4]. One of the critical parameters for the caprock sealing efficiency is breakthrough pressure, i.e., the excess of CO_2 pressure above initial pore fluid pressure in the caprock that is enough to initiate CO_2 flow through the sealing layer. As a result of CO_2 (non-wetting phase) injection into brine-saturated caprock, its pressure, p_{CO2}, becomes higher than the pressure of brine that initially saturates shale, p_{br}. The difference between the fluid pressure of the non-wetting and wetting phases is the capillary pressure

$$p_{cap} = p_{CO_2} - p_{br} \,. \tag{1}$$

The larger the amount of CO_2 that is injected, the more compressed it becomes and the higher is p_{CO2}. Capillary pressure rises according to (1), until it reaches the gas entry pressure, p_c, and CO_2 enters the caprock pore system. The threshold capillary pressure p_c is an intrinsic property of each particular pore throat, and for an ideal cylinder of diameter d, it is given by the Young-Laplace equation,

$$p_c = \frac{4\gamma\cos\theta}{d} \,, \tag{2}$$

where γ is the surface tension acting at the brine-CO_2 interface and θ is the contact angle of brine-CO_2 surface with respect to the solid phase (Fig. 1). Thus, for a given brine-saturated pore throat of diameter d, CO_2 will enter into it if the CO_2 pressure reaches

$$p_{CO_2} = p_{br} + \frac{4\gamma\cos\theta}{d} \,. \tag{3}$$

A number of studies are dedicated to breakthrough of non-wetting fluids, including CO_2, into shales and other clay-rich materials. The simplest method suggested by IEAGHG [4] involves prediction of the CO_2 entry pressures from the knowledge of corresponding interfacial tensions and contact angles and mercury intrusion porosimetry results for a given caprock. Additionally, the breakthrough pressure can be measured using direct methods, where excess CO_2 pressure is slowly and gradually increased until continuous CO_2 flow is observed [18]. Tanai et al. [19] showed that breakthrough pressures are reproducible, because the pathways created by the first breakthrough experiment are further closed by water imbibition in the absence of fabric damage and become drained again for successive CO_2 breakthrough tests.

Due to the time-consuming nature of direct breakthrough pressure measurements, Hildenbrand et al. [20] and Egermann et al. [21] introduced an indirect experimental technique. They studied a capillary threshold pressure, sometimes referred to as snap-off pressure, and defined the breakthrough pressure as the one at which CO_2 stops flowing through the specimen after its injection is finished. After ceasing the injection, CO_2 upstream pressure starts decreasing due to the resistance of capillary pressure within the pore space, but downstream pressure is maintained constant (see [22] for details). Application of direct and indirect methods gives different breakthrough pressure values for the same material, with variations of 100% and more [23]. Proper explanation of these differences is of great importance because reduction in the breakthrough pressure means reduction in the sealing efficiency of a geological storage system.

Apart from the breakthrough pressure, the effectiveness of a seal is characterized by CO_2 relative permeability. Bocquet and Charlaix [24] demonstrated that the Navier-Stokes equations – and hence Darcy’s law – are valid for pore diameters as low as 1 nm, thus are applicable for most of clay-rich materials. An attempt to measure CO_2 relative permeability was performed by Harrington et al. [25], but the low-permeability of shale makes it difficult to interpret the results.

The materials that are considered as potential caprocks for geological storage present permeabilities below 10^{-18} m^2 and high CO_2 entry pressures (~ 1-10 MPa) [26]. The required high-pressure (> 10 MPa) injection tests at elevated temperatures (> 32 ºC) representing in situ conditions and long experimental timescales (~ months) limit laboratory studies. Nevertheless, comprehensive experimental work should allow for proper description of geomechanical and petrophysical properties of clay-rich rocks during CO_2 injection.

3. Experimental methods

3.1. Material

Opalinus clay (shaly facies of Jurassic shale) is a ductile clay-rich (around 60%) material with nano-scale porosity of around 0.12 (Fig. 2), permeability ~ 10^{-20} m^2 [27], and predicted CO_2 entry pressure in the order of a few MPa. Hence, it satisfies the requirements for a potential caprock [26]. In the scope of the current study, two types of fully saturated Opalinus clay specimens are investigated: intact and remolded (i.e., reconstituted) rock. The latter one is assumed to represent material in proximity of faults and fractures within a shale layer [28]. Remolded shale possesses strongly effective mean stress dependent permeability in the range of 10^{-20} – 10^{-18} m^2.

Remolded shale specimens are prepared by crushing the intact material in a grinder and sieving the particles with a size smaller than 0.5 mm. Then, brine corresponding to approximately 1.5 times the liquid limit (or 60%) is added and mixed with the powder. The obtained clay-rich material is consolidated for at least 72 hours in one-dimensional conditions by putting it in the steel-walled tube and applying the axial stress of 350 MPa. The obtained cylindrical specimens have porosity of 0.33 and the degree of saturation of 0.85 - 0.90. Crushing of the clay preserves the flake-like structure of an intact material, but significantly changes the shale properties (e.g., porosity, permeability, bulk moduli) at low effective stresses. However, at the high effective stresses, porosity reduces to 0.15, permeability drops by two orders of magnitude, and bulk modulus increases by a factor of 200, so the material properties appear to be close to those of the intact rock. Additionally, consolidation at high effective stresses makes pore size distribution for remolded shale look similar to the one of intact material (Fig. 2b). In this paper, the remolded shale is referred to as RS, while the intact shale specimen is called OPA.

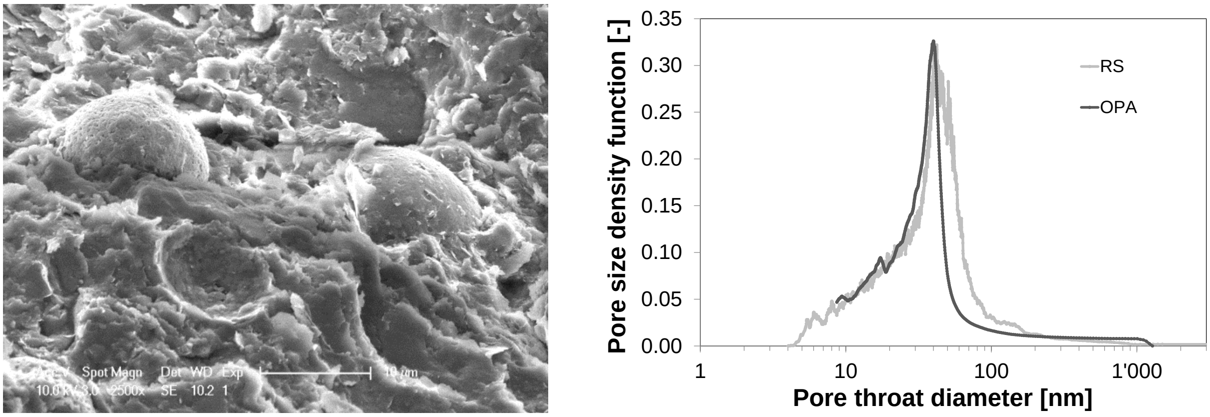

(a) (b)

Figure 2. Unconfined shale specimens: (a) surface electron microscopy of OPA with 2500x magnification and (b) mercury intrusion porosimetry (MIP) test results on OPA and RS.

3.2. Experimental apparatus and technique

Cylindrical specimens (height h = 12.5 mm, diameter D = 35 mm) of remolded and intact shale are prepared and loaded in the oedometric cell, which provides zero lateral strain conditions (Fig. 3). The total mean stress P can be calculated from the generalized Hooke's law knowing the applied vertical stress σ_{ax} and Poisson ratio ν,

$$P = \frac{1+\nu}{3(1-\nu)}\sigma_{ax} \tag{4}$$

The upstream and downstream pressure/volume controllers (GDS Instruments, UK) are utilized to induce pore pressure inside the rock and measure volume of fluid that enters or leaves the specimen. The syringe pump (Teledyne ISCO, USA) is connected in parallel with the upstream pressure/volume controller and is used to inject CO_2 into the sample. The upstream and the downstream pressure lines are instrumented with valves that can prevent the flow and pore pressure transducers providing accurate pore pressure measurements (Fig. 3). In this work, axial stress was imposed in the range from 27 to 42 MPa, pore fluid pressure – from 8 to 20 MPa, and temperature – at 24 °C and 40 °C. The lower temperature represents near-wellbore case where CO_2 is in liquid state, while imposing the higher temperature allows studying far-from-the-wellbore case with supercritical CO_2. The oedometric cell at the EPFL gives an advantage in studying deformation and fluid flow in low-permeable geomaterials due to relatively small specimen height comparing to conventional triaxial configurations (12.5 mm vs ~ 100 mm). It reduces the experimental time for fluid flow by an order of magnitude and the characteristic diffusion time by two orders of magnitude. All the equipment is placed inside a thermostat room providing constant and well-maintained (within 0.2 °C) temperature during testing and excluding undesirable CO_2 phase transition within the system.

Rock was fully-saturated with the brine having the chemical composition of the formation pore fluid [29] that is supposed to have no chemical effect on the material at in situ conditions. Back pressure saturation method is implemented for ten days with graduate increase of the upstream and downstream pressures and promoting the flow through the specimen. It allows achieving full saturation at brine pressures $p > 8$ MPa that is confirmed by measurements of constant Skempton's B coefficient values while the effective mean stress (P') is preserved to be constant [30] and equal to 8 MPa. Recorded undrained pore pressure increments are corrected for the influence of "dead" volume [31] and provide $B = 0.85$ for RS and $B = 0.81$ for OPA, though the latter one might be affected by the anisotropy of loading. Effective mean stress and bulk moduli are calculated from applied vertical stress and vertical deformation using the following values of drained Poisson ratio ν: 0.30 for RS (at $P' < 1$ MPa) and 0.33 for OPA (perpendicular to the bedding planes), both measured in conventional triaxial tests.

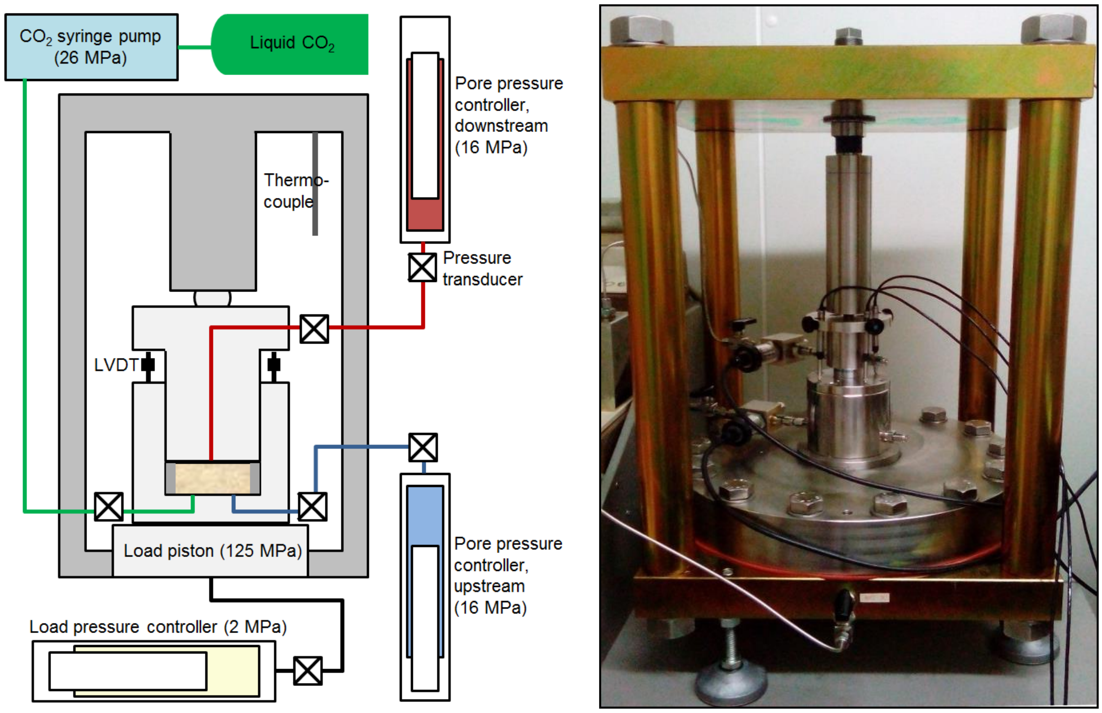

(a) (b)

Figure 3. (a) Schematic diagram and (b) photo of the oedometric loading setup at the EPFL that allows studying flow and mechanical properties of low-permeable rock saturated with brine and high-pressure CO_2.

Intrinsic permeability, k_{int}, is determined from Darcy's law after achieving steady-state flow conditions in the brine saturated specimens

$$k_{int} = -\frac{4\eta_{br} h \Delta V}{\pi D^2 p_{diff} \Delta t}, \tag{5}$$

where η_{br} is brine viscosity (0.001 Pa•s) , p_{diff} is the differential fluid pressure between downstream and upstream of the specimen, and ΔV is fluid volume that passed through the sample during the time period Δt. Considering all the contributing factors, permeability is measured with an accuracy of 2.5% when the duration of steady-state flow exceeds 12 hours. Consistence of measurements is ensured by obtaining constant permeability values with standard deviation of 2.5% for several consecutive measurements at constant differential fluid pressure.

After shale permeability is measured using brine as the only pore fluid, CO_2 is injected into the specimen. Residual pressure technique for the breakthrough pressure measurements [20] is utilized. The downstream pressure/volume controller (Fig. 3) is set to hold the brine pressure at a constant value, 8 MPa in this study. The upstream CO_2 controller is maintaining a pressure that is higher than the downstream brine pressure. It is essential to set p_{diff} larger than the estimated value of CO_2 breakthrough pressure p_{break} to promote CO_2 flow through the rock. The valve within the upstream fluid line is then closed and CO_2 pressure at the upstream side starts decreasing as the flow goes on. As soon as the differential pressure reaches p_{break} value, the reading of the upstream pressure transducer stops decreasing and maintains a constant value. The downstream pressure/volume controller measurements confirm that the fluid flow is blocked by the capillary forces. Measured residual value of p_{diff} is considered as CO_2 breakthrough pressure. In the current study, obtained breakthrough pressure values were confirmed according to the breakthrough definition: CO_2 flow was achieved at p_{diff} being 0.1 MPa higher than p_{break}, while no flow was observed at p_{diff} lower than p_{break}. The accuracy of the breakthrough pressure measurements improves with the increase in the measured p_{break} value, starting from 2% for 0.8 MPa breakthrough pressure.

Following CO_2 breakthrough in the shale, its viscous flow through the material is assumed. The process of steady-state flow is described by Darcy's law with flow in vertical direction only. Darcy's law for the unidirectional case relates the flow rate of the i-th phase $\Delta V_i/\Delta t$ along considered direction to the gradient of differential fluid pressure $p_{diff}/\Delta x$, and can be written in terms of relative permeability of the CO_2 phase k_{rCO2}

$$k_{rCO2} = -\frac{4\Delta V_{CO_2}\eta_{CO_2}h}{k_{int}\pi D^2 p_{diff}\Delta t}, \qquad (6)$$

where η_{CO2} is the CO_2 viscosity, which range is $(7.0 - 9.5)\cdot 10^{-5}$ Pa•s for liquid CO_2 and $(2.2 - 7.4)\cdot 10^{-5}$ Pa•s for supercritical CO_2 at pressures between 8 and 18 MPa [32]. The intrinsic permeability is assumed to remain constant, unless microstructural changes occur inside the specimen. Consistent CO_2 permeability values (within standard deviation of 3%) obtained during several consecutive measurements at constant differential fluid pressure demonstrated relevance of steady-state CO_2 flow assumption.

4. Results

The material properties for remolded and intact shale measured at 27 MPa axial stress and 8 MPa pore pressure, which are representative of storage conditions at 800 m depth, are presented in Table 1. The properties of both materials are very similar, though the remolded shale has a higher porosity, with better interconnected pores than the intact rock, which leads to the permeability increase by almost a factor of two. On the other hand, the geomechanical properties of the two specimens are almost identical.

Table 1: Material properties of intact (OPA) and remolded (RS) shale at σ_{ax} = 27 MPa and p = 8 MPa.

Material	Porosity, n [-]	Permeability, k [m^2]	Bulk modulus, K [GPa]	Skempton's coef., B [-]	Poisson ratio, ν [-]
RS	0.15	$9\cdot 10^{-21}$	2.5	0.85	0.30
OPA	0.12	$5\cdot 10^{-21}$	2.6	0.81	0.33

Fig. 4a shows residual pressure measurement for RS at 35 MPa axial stress when flowing liquid CO_2 through the sample. Downstream fluid volume indicates when capillary forces block CO_2 flow. The obtained liquid CO_2 breakthrough pressure value of 5.0 MPa is confirmed via the direct method according to the definition of breakthrough (Fig. 4b). Downstream volume measurements in Fig. 4b evidence CO_2 flow at 5.3 MPa differential pressure, but the flow dramatically decreases at 5.0 MPa differential pressure and completely stops at 4.9 MPa. At this point, all brine in the specimen and connected system is CO_2-rich, because the chemical effect of CO_2 dissolution is much faster than the mechanical effect of breakthrough.

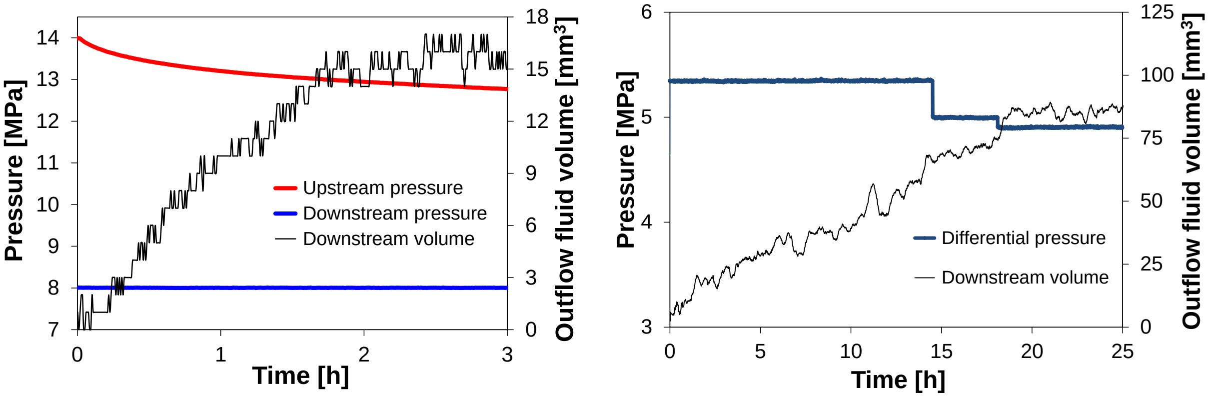

(a)

(b)

Figure 4. Measurement of liquid CO_2 breakthrough pressure for RS at 35 MPa axial stress. (a) Residual differential pressure is 5.0 MPa, when CO_2 flow stops; (b) confirmation of 5.0 MPa breakthrough pressure: no CO_2 flow at constant differential pressure value of 4.9 MPa.

The breakthrough pressure for liquid and supercritical CO_2 injection are similar regardless of the applied axial stress, except for remolded shale under an axial stress of 35 MPa (Fig. 5). Liquid CO_2 breakthrough pressure is almost 1.8 times higher than that for supercritical CO_2 at 35 MPa. In general, a lower breakthrough pressure is expected for supercritical CO_2 given its lower interfacial surface tension compared to liquid CO_2. However, the observed difference at σ_{ax} = 35 MPa is larger than expected and might be due to a possible heterogeneity generated during the sample preparation of remolded shale.

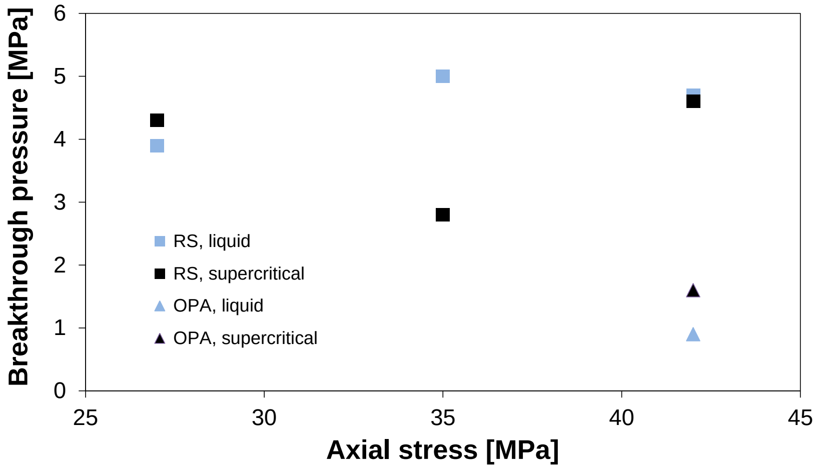

Figure 5. Summary of CO_2 breakthrough pressure measurements: liquid (blue) and supercritical (black) CO_2 in remolded (squares) and intact (triangles) shale specimens.

Fig. 6a shows the CO_2 breakthrough pressure measurements performed on remolded shale at an axial stress of 35 MPa for both liquid and supercritical CO_2. Breakthrough pressure of supercritical CO_2 appears to be lower than that of liquid CO_2 in remolded shale by almost a factor of two: 2.8 MPa vs 5.0 MPa. The low breakthrough pressure of supercritical CO_2 suggests that CO_2 may penetrate into the caprock, at least in regions where, for some reason, the breakthrough pressure is relatively low.

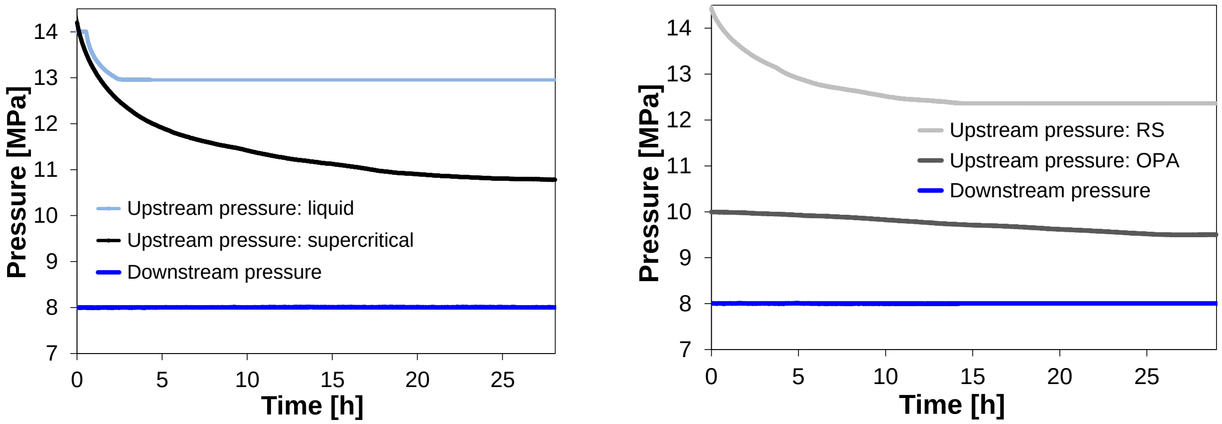

(a) (b)

Figure 6. (a) CO_2 breakthrough pressure measurements for remolded shale (RS) at 35 MPa axial stress when flowing supercritical and liquid CO_2; (b) Supercritical CO_2 breakthrough pressure measurements for remolded (RS) and intact (OPA) shale at 42 MPa axial stress.

Unlike RS, intact Opalinus clay specimen (OPA) is not an artificial rock, but a natural caprock representative. CO_2 breakthrough is studied for OPA at an axial stress of 42 MPa. Fig. 6b shows the breakthrough pressure measurements for OPA and RS for CO_2 flow in supercritical state. CO_2 breakthrough pressure turns out to be about three times lower for intact material than for remolded one: 1.6 MPa for OPA and 4.6 MPa for RS, which may be explained by heterogeneity of intact shale specimen where the channels with larger than dominant pore diameter can be found. Further tests are needed to properly assess this observation.

In the case of CO_2 entering into the caprock, the relative permeability to CO_2 would control CO_2 flow across the caprock. CO_2 relative permeability in shale is measured when steady-state flow of CO_2 through the material has been established. The steady-state nature of the flow is ensured once constant permeability values are calculated using equation (6) during several consequent time periods (Fig. 7a). Fig. 7b presents the measurements of the product of the intrinsic permeability and the relative permeability to CO_2 for remolded and intact shale. The only measurement for the intact material – with liquid CO_2 – was conducted at 42 MPa axial stress and resulted in the permeability value 30 times lower than that for the remolded material. Laboratory experiments of CO_2 flow in RS revealed that permeabilities of liquid and supercritical CO_2 are almost identical for remolded shale, both showing a decreasing trend with increasing axial stress. This trend may be related to pore squeezing, which is expected to be a result of axial and, thus, total and effective mean stress increase according to equation (4).

Finally, the saturation of remolded shale with liquid CO_2 is evaluated with the brine imbibition technique. After continuous CO_2 flow is established in the RS specimen at various differential pressures, the upstream channel is closed and brine from the downstream starts replacing CO_2 in the pores. The equilibrium in the system (i.e., constant downstream volume readings) is reached after injection of 140 – 200 mm^3 of brine, which provides the values of 0.10 to 0.14 for CO_2 saturation given that all brine in the system is already CO_2-rich.

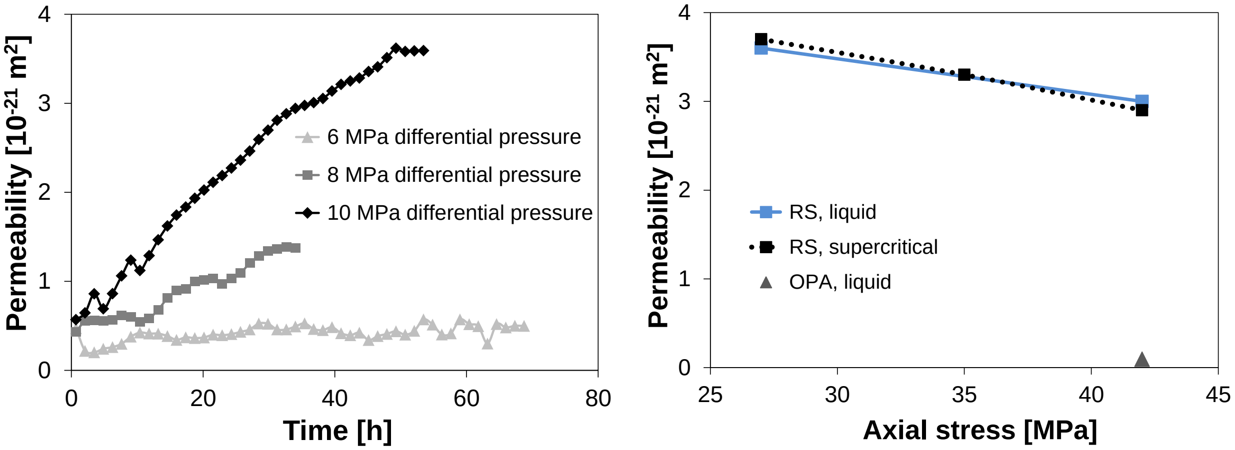

(a) (b)

Figure 7. CO_2 permeability (product of intrinsic permeability and CO_2 relative permeability) for remolded and intact Opalinus clay specimens: (a) time-scale for establishing steady-state flow at various differential pressure values for RS at 27 MPa axial stress; (b) summary of permeability (product of intrinsic permeability and CO_2 relative permeability) measurements for supercritical and liquid CO_2 in RS and OPA at a differential pressure of 10 MPa.

5. Discussion and conclusion

This study highlights the importance of testing shales representative of potential caprocks at realistic conditions that may be encountered in actual CO_2 storage sites. We have tested both remolded and intact Opalinus clay in the oedometric cell at several axial stress values and flowing either liquid or supercritical CO_2. Given fixed pressure and temperature values, most of the tests provided similar (within 5%) values for CO_2 breakthrough pressure measured by two different methods: direct (with the establishment of continuous CO_2 flow) and indirect (through a residual capillary pressure evaluation). From the obtained results, it can be concluded that CO_2 breakthrough pressure and permeability strongly depend on the caprock microstructure and this relationship appears to be of complex nature. This study shows that the intrinsic permeability of a tighter material (intact Opalinus clay) is around two times lower than that of remolded shale, which has a more open microstructure. The pore size has a greater effect on the CO_2 relative permeability, because the intact rock becomes 30 times less permeable to CO_2 than the remolded shale (Fig. 7b). This implies that for a similar CO_2 saturation, the CO_2 relative permeability of intact rock is 15 times smaller than for remolded shale. However, CO_2 breakthrough pressure for the tighter material is almost three times lower than for more permeable material (Figs. 5 and 6b). Thus, the breakthrough pressure cannot be correlated with the intrinsic permeability of the caprock, which is sometimes done in literature [33]. Instead, careful investigation of CO_2 breakthrough and permeability into the caprock has to be conducted, considering various materials under different axial and lateral stresses. Such studies require long experimental times given the low permeability of shales. Although, proper testing as well as the microstructure evolution investigation are necessary to provide the data for improving the fundamental understanding of the phenomena, leading to enhancement in the planning of storage projects.

Acknowledgements

Opalinus clay cores were provided by Swisstopo in the framework of Mont Terri Project, CS-C experiment. R. Makhnenko activities are sponsored by SCCER-SoE (Switzerland) grant KTI.2013.288 and Swiss Federal Office of Energy (SFOE) project CAPROCK #810008154. V. Vilarrasa acknowledges support from the ‘EPFL Fellows’ fellowship programme co-funded by Marie Curie, FP7 Grant agreement no. 291771.

References

[1] Cavanagh AJ, Haszeldine RS. The Sleipner storage site: Capillary flow modeling of a layered CO_2 plume requires fractured shale barriers within the Utsira Formation. International Journal of Greenhouse Gas Control 2014; 21:101-112.

[2] Sorey ML, Evans WC, Kennedy BM, Farrar CD, Hainsworth LJ, Hausback B. Carbon dioxide and helium emissions from a reservoir of magmatic gas beneath Mammoth Mountain, California. Journal of Geophysical Research 1998; 103:15303-15323.

[3] Miocic JM, Gilfillan S, McDermott C, Haszeldine RS. Mechanisms for CO_2 leakage prevention – A global dataset of natural analogues. Energy Procedia 2013; 40:320-328.

[4] IEAGHG. Caprock systems for CO_2 geological storage. IEA Environmental Projects Ltd 2011.

[5] Orr FM Jr. Onshore geologic storage of CO_2. Science 2009; 325:1656-1658.

[6] Song J, Zhang D. Comprehensive review of caprock-sealing mechanisms for geologic carbon sequestration. Environmental Science & Technology 2012; 47(1):9-22.

[7] Liu L, Yu Z, Yang S, Li S, Yang Y. An experimental study of CO_2–brine–rock interaction at in-situ pressure–temperature reservoir conditions. Chemical Geology 2012; 326-327:88-101.

[8] Espinoza DN, Santamarina JC. Clay interaction with liquid and supercritical CO_2: The relevance of electrical and capillary forces. International Journal of Greenhouse Gas Control 2013; 10:351-362.

[9] Noiriel C, Made B, Gouze P. Impact of coating development on the hydraulic and transport properties of argillaceous limestone fractures. Water Resources Research 2007; 43:W09406.

[10] Angeli M, Soldal M, Skurtveit E, Eyvind Aker E. Experimental percolation of supercritical CO_2 through a caprock. Energy Procedia 2013; 1: 3351–3358.

[11] Olabode A, Radonjic M. Shale caprock/acidic brine interaction in underground CO_2 storage. Journal of Energy Resources Technology 2014; 136:042901-1 - 042901-6.

[12] Gor YG, Elliot TR, Prévost JH. Effects of thermal stresses on caprock integrity during CO_2 storage. International Journal of Greenhouse Gas Control 2013; 12:300-309.

[13] Vilarrasa V, Rutqvist J, Rinaldi AP. Thermal and capillary effects on the caprock mechanical stability at In Salah, Algeria. Greenhouse Gases: Science and Technology 2015; 5:449-461.

[14] Vilarrasa V, Olivella S, Carrera J, Rutqvist J. Long term impacts of cold CO_2 injection on the caprock integrity. International Journal of Greenhouse Gas Control 2014; 24:1-13.

[15] Paterson L, Lu M, Connell LD, Ennis-King J. Numerical modeling of pressure and temperature profiles including phase transitions in carbon dioxide wells. In: SPE Annual Technical Conference and Exhibition, 21–24 September 2008, Denver.

[16] Vilarrasa V, Silva O, Carrera J, Olivella S. Liquid CO_2 injection for geological storage in deep saline aquifers. International Journal of Greenhouse Gas Control 2013; 14:84-96.

[17] Garapati N, Randolph JB, Saar MO. Brine displacement by CO_2, energy extraction rates, and lifespan of a CO_2-limited CO_2-Plume Geothermal (CPG) system with a horizontal production well. Geothermics 2015; 55:182-194.

[18] Thomas LK, Katz DL, Tek MR. Threshold pressure phenomena in porous media. SPE Journal 1968; 243:174-184.

[19] Tanai K, Kanno T, Gallé C. Experimental study of gas permeabilities and breakthrough pressures in clays. Materials Research Society Symposium Proceedings 1997; 465:995-1002.

[20] Hildenbrand A, Schlömer S, Krooss BM. Gas breakthrough experiments on fine-grained sedimentary rocks. Geofluids 2002; 2:3-23.

[21] Egermann P, Lombard J-M, Bretonnier P. A fast and accurate method to measure threshold capillary pressure of caprocks under representative conditions. International Symposium of the Society of Core Analysts, Trondheim, Norway; 12–16 September 2006.

[22] Amann-Hildenbrand A, Kroos BM, Bertier P, Busch A. Laboratory testing procedures for CO_2 capillary entry pressures on caprocks. In Gerdes KF (ed.), Carbon Dioxide Capture for Storage in Deep Geological Formations 2015; vol. 4, ch. 25.

[23] Boulin PF, Bretonnier P, Vassil V, Samouillet A, Fleury M, Lombard J-M. Sealing efficiency of caprocks: Experimental investigation of entry pressure measurement methods. Marine and Petroleum Geology 2013; 48:20-30.

[24] Bocquet L, Charlaix E. Nanofluidics, from bulk to interfaces. Chemical Society Reviews 2010; 39:1073–1095.

[25] Harrington JF, Noy DJ, Horsernall ST, Birchall DJ, Chadwick RA. Laboratory study of gas and water flow in the Nordland Shale, Sleipner, North Sea. State of the science: AAPG Studies in Geology 2009; 59:527-543.

[26] IPCC. Special report on carbon dioxide capture and storage. Cambridge University Press 2005.

[27] Bossart P. Characteristics of the Opalinus Clay at Mont Terri. 2012. http://www.mont-terri.ch/internet/montterri/de/home/geology/ key_ characteristics.html

[28] Egholm DL, Clausen OR, Sandiford M, Kristensen MB, Korstgard JA. The mechanics of clay smearing along faults. Geology 2008; 36:787-790.

[29] Pearson FJ. PC experiment: recipe for artificial pore water. Mont Terri Project, Technical Note 2002-17.

[30] ASTM D4767. Standard Test Method for Consolidated Undrained Triaxial Compression Test for Cohesive Soils 2011.

[31] Makhnenko RY, Labuz JF. Elastic and inelastic deformation of fluid-saturated rock. Philosophycal Transactions of Royal Society A 2016; 374:20150422.

[32] Span R, Wagner W. A New Equation of State for Carbon Dioxide Covering the Fluid Region from the Triple-Point Temperature to 1100 K at Pressures up to 800 MPa. Journal of Physical and Chemical Reference Data 1996; 25:1509.

[33] Amann-Hildenbrand A, Bertier P, Busch A, Krooss BM. Experimental investigation of the sealing capacity of generic clay-rich caprocks. International Journal of Greenhouse Gas Control 2013; 19:620-641.

Available online at www.sciencedirect.com

ScienceDirect

Energy Procedia 00 (2017) 000–000

Energy Procedia

www.elsevier.com/locate/procedia

13th International Conference on Greenhouse Gas Control Technologies, GHGT-13, 14-18 November 2016, Lausanne, Switzerland

Quantification of viscous creep influence on storage capacity of caprock

Ludovic Räss[a]*, Roman Y. Makhnenko[b,c], Yuri Podladchikov[a], Lyesse Laloui[b]

[a]*Institute of Earth Sciences, University of Lausanne, Geopolis UNIL-Mouline, CH-1015 Lausanne, Switzerland*
[b]*Laboratory of Soil Mechanics, École Polytechnique Fédérale de Lausanne, EPFL ENAC IIC LMS, GC – Station 18, CH-1015 Lausanne, Switzerland*
[c]*Department of Civil & Environmental Engineering, University of Illinois at Urbana-Champaign, 205 North Mathews Ave, Urbana, IL, 61801-2352, USA*

Abstract

In the light of growing concerns for the climate change, it is of particular interest for governments to encourage efficient capture and safe storage of large amounts of carbon dioxide in the subsurface. In this perspective and in order to accurately predict the short and long-term response of the reservoir, a precise characterization of the geomechanical properties has to be carried out. In addition to the classical poroelastic properties, time-dependent deformation, such as viscous creep should also be considered. Storage capacity of a caprock may be seriously affected by local creep deformation allowing fast vertical fluid flow through an a priori very impermeable formation. Within this study, we investigate the ease to creep of Opalinus clay (Jurassic shale) under shallow geological storage conditions and predict the propagation of high porosity channels at operational time scales. The effective poroviscoelastic parameters of rock are inferred from the novel laboratory experiments that allow evaluation of time-dependent deformation. The bulk viscosity of the shale is found to be ~ 10^{14} - 10^{15} Pa·s and it decreases with rise of temperature and pore fluid pressure to total mean stress ratio. Furthermore, the propagation speed of high porosity channels (porosity waves) is calculated to be on the order of the centimeters per year.

Peer-review under responsibility of the organizing committee of GHGT-13.
Keywords: geomechanics; shale; Opalinus clay; poromechanics; bulk viscosity; porosity waves; numerical modeling; GPU.

---

* Corresponding author. Tel.: +41 21 692 44 19
E-mail address: ludovic.raess@unil.ch

Peer-review under responsibility of the organizing committee of GHGT-13.

1. Introduction

Carbon dioxide (CO_2) storage security is largely influenced by the caprock integrity, especially at the early stages after the start of injection. The lower boundary of the caprock will then be in contact with CO_2-rich brine or pore fluid that consists almost of pure CO_2. Thermal and chemical interactions between the pore fluid and the caprock may change the material properties of the latter one. Geomechanical stability is also crucial for the caprock, since failure would potentially lead to a significant permeability increase and induced seismicity [1]. Considering clay-rich materials (e.g., shales) as potential seals has several advantages. In case the reservoir overpressure is not very important, the thermal, chemical and inelastic deformations of the clay-rich ductile formation might not affect the caprock integrity. Another advantage of considering clay-rich materials as a potential seal is that the upward movement of CO_2 through the pore system is resisted by capillary pressure; the breakthrough pressure (CO_2 entry pressure) for shale is on the order of mega Pascals [2, 3, 4].

Although clay-rich formations show interesting self-sealing features, their ease to flow (or creep) might become a serious issue when assessing long-term storage integrity of a reservoir [5]. Viscous (time-dependent) deformation of shales has been considered experimentally [e.g., 6, 7, 8], but little attention was payed to studying material behavior at high pore pressures as it is in geological storage. In general, geomaterials, even partially saturated with water, have a nonlinear rheology and time-dependent behavior of rock is a function of mean and differential stress, pore pressure, chemistry of a pore fluid, temperature, and microstructural properties of the rock among others [e.g. 9, 10, 11].

Viscous compaction of fluid-filled porous media allows a generation of a special type of fluid flow instability that leads to formation of high-porosity, high-permeability domains that are able to self-propagate upwards due to interplay between buoyancy and viscous resistance of the deforming porous matrix. This instability is known as "porosity wave" [12, 13] and its formation is possible under conditions applicable to carbon dioxide storage in reservoirs and explains creation of high-porosity channels and chimneys [14].

In this study, time-dependent or poroviscoelastic processes are included in the constitutive equations by analogy with Biot's poroelastic relationships. We present the experimental methods to measure the parameters related to the model and the values of this parameters at in situ conditions for a caprock representative - Opalinus clay (Jurassic shale). We use the values obtained in the lab experiments to feed the numerical models in order to predict the time and length scale of possible porosity wave propagation in conditions relevant for caprock integrity.

2. Background

To predict the porosity evolution, thus the possible formation of high permeability and porosity pipe structures in saturated porous media, we use a closed system of equation proposed by [15] were time dependent or creep effects are taken into account using the viscoelastic correspondence principle. The model reduces to Biot linear theory in the elastic limit [16] and verifies the viscous solution in the incompressible limit [17]. The set of proposed equations forms a closed system that ensures thermodynamic consistency and non-negativity of entropy production. Within this section, we highlight some relevant parts of the full derivation that can be found in [15].

The variable ϕ represents the interconnected porosity, υ^s and υ^f are solid and fluid velocity, respectively. Fluid and solid pressures, p^f and p^s respectively, can be expressed through the fluid bulk modulus K_f, the unjacketed bulk modulus K_s', and the unjacketed pore bulk modulus K_s'' [18]. The main rheological assumption adopted here is the Maxwell bulk viscoelasticity:

$$\nabla_k \upsilon_k^s = -\frac{1}{K_d}\frac{\partial \bar{p}}{\partial t} + \left(\frac{1}{K_d} - \frac{1}{K_s'}\right)\frac{\partial p^f}{\partial t} - \frac{\bar{p} - p^f}{(1-\phi)\eta_\phi} \tag{1}$$

Here, K_d is the drained bulk modulus and η_ϕ is the effective bulk viscosity, which reflects properties of porous rock such as its pore structure and viscous and failure parameters of its mineral grains. The viscous part is governed by the Terzaghi effective stress: $p^e = \bar{p} - p^f$. Substituting equation (1) into the solid mass balance equation provides an expression for viscous and elastic evolution of the porosity [15, 18]:

$$\frac{\partial \phi}{\partial t} = -\left(\frac{1-\phi}{K_d} - \frac{1}{K_s{}'}\right)\frac{\partial p_e}{\partial t} + \phi\left(\frac{1}{K_s{}'} - \frac{1}{K_s{}''}\right)\frac{\partial p^f}{\partial t} - \frac{p_e}{\eta_\phi} \tag{2}$$

The increment of fluid content is recovered by substituting equation (1) into the sum of fluid and solid mass balance equations to eliminate the time derivatives of densities and the porosity and the divergence of solid velocity [15]:

$$\nabla_j\left(\phi\left(\upsilon_k^f - \upsilon_k^s\right)\right) = \left(\frac{1}{K_d} - \frac{1}{K_s{}'}\right)\left(\frac{\partial \bar{p}}{\partial t} - \frac{1}{B}\frac{\partial p^f}{\partial t}\right) + \frac{p_e}{(1-\phi)\eta_\phi} \tag{3}$$

where B is Skempton's [18, 19] coefficient:

$$B = \frac{\dfrac{1}{K_d} - \dfrac{1}{K_s{}'}}{\dfrac{1}{K_d} - \dfrac{1}{K_s{}'} + \phi\left(\dfrac{1}{K_f} - \dfrac{1}{K_s{}''}\right)} \tag{4}$$

3. Methods

3.1 Experimental technique

The parameters introduced in section 2 that govern poroelastic behavior of isotropic fluid-saturated rock, i.e. the drained bulk modulus K_d, the unjacketed bulk modulus $K_s{}'$, and Skempton's coefficient B, can be measured experimentally under the three limiting conditions: drained, unjacketed, and undrained [18]. Another unjacketed parameter - $K_s{}''$ is rarely reported, because its measurements are associated with very small pore volume changes under constant effective stress. Although, it can be calculated from equation (4) if other parameters are known.

$K_s{}'$ is measured under the unjacketed boundary conditions, which are achieved in hydrostatic ($\sigma_1 = \sigma_2 = \sigma_3 = \bar{p}$ compression experiments [20]. Prismatic specimen (50 × 35 × 35 mm) with strain gage rosettes on its sides is saturated with the confining fluid (hydraulic oil), which seemed to have no chemical effect on the tested rock in a short-term. After at least 10 days of gradual increase of pore pressure up to 60 MPa, unjacketed unloading ($\bar{p} = p^f$ and $d\bar{p} = dp^f$) is performed.

Drained (constant pore pressure) and undrained (constant fluid content) compression experiments are conducted on cylindrical specimens (height = 100mm and diameter = 50 mm) in the GDS Advanced triaxial cell at the EPFL. The setup is calibrated for testing of fluid-saturated rock at elevated temperatures (Fig. 1). Back pressure saturation technique (described in [21]) is implemented: the increments of pore (or back) pressure are applied while keeping the effective mean stress approximately the same. Then, so-called B-checks are performed and achievement of constant value of B independent of the magnitude of the pore pressure indicates full saturation. Measured Skempton's B coefficient values are corrected to consider the contribution of the "dead" volume and the compressibility of the pore pressure measuring system. Drained bulk modulus K is calculated directly from the measured axial and radial displacements and indirectly from the volume of the fluid that escaped the specimen during compression under constant pore pressure. Knowledge of $K_s{}'$ then can provide a proper evaluation of K [18].

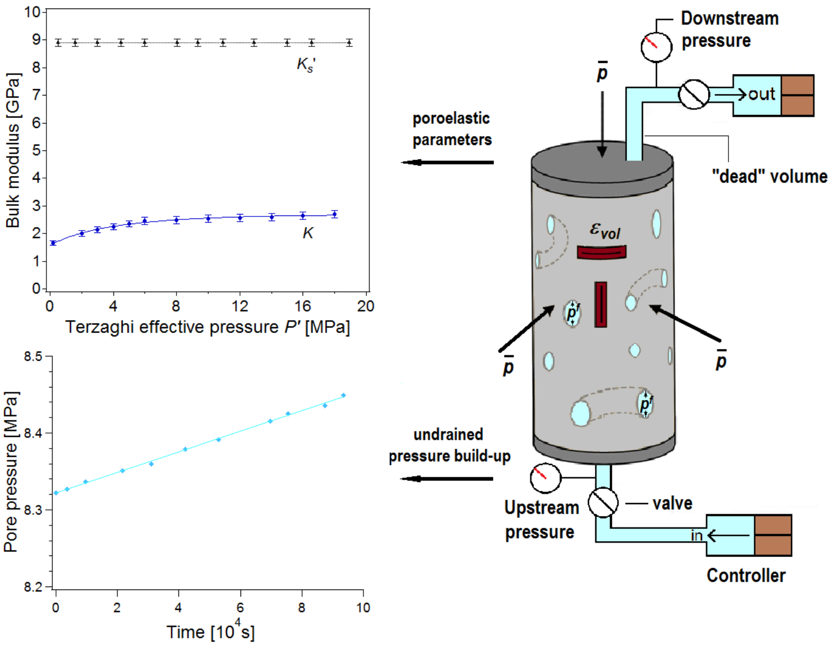

Fig 1. Experimental setup within the Advanced triaxial cell at the EPFL with indication of performed measurements; precise stress and strain measurements at different limiting regimes allow for calculation of poroelastic parameters and observation of undrained pore-pressure build-up for fully saturated specimens provides the evaluation of material's bulk viscosity.

Equation (1) provides the following method for calculating the bulk viscosity under constant mean stress, $d\bar{p}/dt = 0$, and drained boundary conditions, $dp^f/dt = 0$, which can be referred to as the "direct" method,

$$\eta_\phi = -\frac{\bar{p} - p^f}{(1-\phi)\nabla_k \upsilon_k^s} \tag{5}$$

Here $\nabla_k \upsilon_k^s$ can be treated as the volume strain rate, and considering the accuracy of volume strain measurements (1 x 10^{-5}) and the level of applied effective mean stresses (~ MPa), the observation time for calculating the bulk viscosity with two significant figures is ~ 10^5 sec. The time scales should be even longer to compensate for the effects of temperature and pressure perturbations; hence the bulk viscosity of shallow rock is rarely reported.

For porous materials, the degree of saturation is the critical parameter to govern their viscous response: if saturation is not full – pore pressure does not increase significantly under the undrained condition, but rather decreases while the air bubbles dissolve in pore water. However, when the full saturation is achieved and material deformation can be considered poroviscoelastic, then equation (3) predicts pore pressure build-up with time at constant total stress conditions. Changes in pore pressure for the fully saturated specimens can be measured more accurately than volume strain; hence, it can be used as the monitoring parameter for viscous behavior and for the calculation of bulk viscosity [22]. The simplified form of equations (2) and (3) for the case of undrained deformation (no flow condition: $\nabla_j\left(\phi\left(\upsilon_j^f - \upsilon_j^s\right)\right) = 0$) at constant mean stress ($d\bar{p}/dt = 0$) leads to another method (referred as "indirect") of evaluating η_ϕ,

$$\eta_\phi = \frac{B\left(\bar{p} - p^f\right)}{(1-\phi)\dfrac{dp^f}{dt}\left(\dfrac{1}{K_d} - \dfrac{1}{K_s'}\right)} \tag{6}$$

The bulk viscosity calculation then requires accurate measurements of poroelastic parameters. However, due to the accuracy of pore pressure measurements this method is significantly less time consuming (~ 10^4 sec).

3.2 Numerical methods

Numerically, the system of partial differential equations is solved on a three-dimensional (3D) staggered grid with regular grid spacing, using a finite difference (FD) discretization. Pressures and material properties are defined at the cell centers, while the Darcy fluxes and solid velocities are defined at the cell mid-faces. Shear components are located at the cell corners. The 3D model is written in C language with CUDA features and is solved on many graphical processing units (GPUs) in parallel, using the standard Message Passing Interface (MPI) routine for inter processes communications.

An iterative pseudo-transient, thus matrix-free, scheme is used to solve the system of partial differential equations. The advantages of using this approach are the lowest possible memory usage that scales $O(n)$ while only local stencil operation to update variables and minimum point to point communication between parallel processes are needed. Such algorithm, therefore, scales linearly with number of parallel processors due to and ensured by its minimalistic construction.

The workflow of the algorithm can be summarized in the following steps, that will be repeated within the time step loop: 1) update values of total and fluid pressures and porosity solving for their time derivatives in the equations (1), (2), and (3); 2) compute the nonlinear viscoelastic rheology as function of the updated porosity and pressures fields; 3) solve the momentum equation (force balance) for the solid velocities; 4) verify the nonlinear residual of the momentum equation and the errors of the equations (1) – (3) and of the nonlinear rheology. Once step 4) is verified and all errors converged to targeted nonlinear tolerance, the porosity can be explicitly advected using a flux limiting upwind scheme [23].

The nonlinear nature of the poroviscoelastic equations sets important challenges in terms of numerical solutions. Strong localization in space and time might spontaneously occur, and a wide range of length scales are involved. To overcome this and to resolve the instabilities, a very high resolution in space and time is required to predict accurate system evolution in time. We therefore employ a numerical resolution of more than $2.5 \cdot 10^8$ grid points in order to have 500 x 500 x 1000 cells in x, y, and z directions, respectively. The GPUs accelerators efficiently speed up the algorithm execution, allowing us to run the full 3D simulation in not more than a five-days wall time on our in-house high performance computing GPU cluster *octopus* [24], designed by the Scientific Computing Group at the Earth Sciences Institute and hosted by the University of Lausanne.

3.3 Material

Opalinus clay (shaly facies) is the Jurassic shale that is studied in the current work as the caprock representative. The shale contains 55-60% of clay (illite, kaolinite, chlorite, and smectite), 25-30% carbonate, 5-10% quartz, and 10-15% organic matter [25]. Interconnected porosity is 0.12, dominant pore throat diameter ~ 30 nm, and intrinsic permeability ~ 10^{-21} - 10^{-20} m^2 [4]. If preserved properly after coring, shale specimens have 80 – 90 % brine saturation, so the natural brine [26] was used as the pore fluid to minimize the chemical effect and its bulk modulus K_f is found to be 2.0 GPa, slightly less than the one for pure water.

The characteristic time for dissipation of the induced pore pressure in a specimen of length L drained at the two ends is on the order of $L^2/4c$, where c is the diffusion coefficient [27], which can be expressed from the permeability k, fluid viscosity μ, and the poroelastic parameters:

$$c = \frac{kB}{\mu\left(\frac{1}{K_d} - \frac{1}{K_s'}\right)} \tag{7}$$

Values of c for the tested shale are ~ 10^{-8} m^2/s for the case of brine saturation. The characteristic time scale for equilibration of the pore pressure inside the rock at the range of stresses applied is on the order of 10^{-5} s for 100-mm-long specimens (used in drained tests) and on the order of 10^{-4} s for the 35-mm-long specimen (used in the unjacketed test). In the latter case though, oil has partially penetrated into the unjacketed sample and increased the viscosity of the pore fluid, hence, the characteristic time scale for pressure dissipation. Finally, each new step in unjacketed test required 24 hours waiting period and the whole test took 15 days. At least 72 hours were spent between the consecutive steps during the drained loading.

4. Results and discussion

The unjacketed compression test provided constant (stress-independent) value of $K_s' = 8.9$ GPa for Opalinus clay after 15 days of gradual unloading from 60 MPa. Three different types of conventional triaxial tests were performed on the cylindrical shale specimens cored perpendicular to the bedding planes to measure the poroelastic parameters of the rock and evaluate its bulk viscosity. One of the specimens was tested at 24 ˚C under low mean stresses and pore pressures (around 2 MPa), approximately corresponding to the in-situ conditions at the Mont Terri underground rock laboratory from where the rock was recovered [25]. Full brine saturation in this case took about 75 days. Another specimen was gradually loaded to total isotropic stress of 10 – 30 MPa and saturated at pore fluid pressure of 8 MPa in 15 days, and its poroviscoelastic parameters were measured at 24 ˚C and 40 ˚C. Drained bulk modulus K and Skempton's B coefficient showed weak stress-dependence: $K = 2$ - 3 GPa and $B = 0.81$ – 0.93 for $p_e = 2$ – 20 MPa. Additionally, brine permeability of shale was measured by steady-state flow method and found to be strongly stress-dependent, changing by an order of magnitude for $p_e = 0.2$ – 5 MPa from ~ 10^{-20} m^2 to ~ 10^{-21} m^2.

The response of Opalinus clay was monitored after each B-check, while a constant isotropic total stress $\overline{p}$ was acting on the specimens. If the behavior of rock is purely poroelastic, application of constant total stress should not produce any pore fluid pressure perturbations. However, the pore pressure build-up occurred for fully saturated specimens at different initial total and pore pressures for all three tested cases (schematically shown in Fig. 1). Note that during the undrained loading when all-around stress is applied to the specimen, it is assumed that it affects the pore pressure immediately and equally inside all the pores. For the tested shale, it was found that pore pressure dissipation in the system takes a few tens of minutes and all further pore pressure changes should be associated with the time-dependent material behavior.

The observation times for the pore pressure build-up ranged from $4\cdot10^4$ to $1.5\cdot10^5$ seconds and provided approximately linear response given that the perturbations of total stress and temperature imposed by the loading system were very small. The effective stress does not appear to be the only governing parameter for the bulk viscosity for a number of sedimentary rock representatives, but rather it is the ratio between the pore pressure and total (isotropic) stress $p^f/\overline{p}$ [22]. The bulk viscosity η_ϕ of shale is calculated to be on the order of 10^{14} - 10^{15} Pa·s and have a decreasing trend with increasing $p^f/\overline{p}$ ratio (Fig. 2). Increase of temperature from 24 ˚C to 40 ˚C is found to have an insignificant effect on poroelastic parameters, but reduces the permeability by 40% and bulk viscosity by a factor of 2. Also, for the shale tested at low pressure, η_ϕ trend is different from the other two cases with a steeper decrease at p^f approaching $\overline{p}$, which may be related to the fact that the shale was subjected to lower than in situ stresses and behaved like underconsolidated material. Values of the bulk viscosity corresponding to the largest achieved $p^f/\overline{p}$ ratios for the three considered cases (low and high pressure hydrostatic compression at 24 ˚C and high pressure compression at 40 ˚C) along with the poroelastic parameters used for calculation are presented in Table 1.

Table 1. Material properties, poroelastic parameters, and bulk viscosity for the largest achieved $p^f/\overline{p}$ ratios for three studied cases.

	ϕ	k	K_d	K_s'	K_f	B	η_ϕ
Testing conditions	[-]	[m^2]	[GPa]	[GPa]	[GPa]	[-]	[Pa•s]
24 ˚C, $\overline{p} = 1.8$ MPa $p^f = 1.6$ MPa	0.12	$3\cdot10^{-20}$	1.65	8.9	2.0	0.93	$2.2\cdot10^{14}$
24 ˚C, $\overline{p} = 15.5$ MPa $p^f = 12.8$ MPa	0.12	$0.9\cdot10^{-20}$	2.2	8.9	2.0	0.90	$9.5\cdot10^{14}$
40 ˚C, $\overline{p} = 11.2$ MPa $p^f = 8.7$ MPa	0.12	$0.5\cdot10^{-20}$	2.2	8.9	2.0	0.90	$4.6\cdot10^{14}$

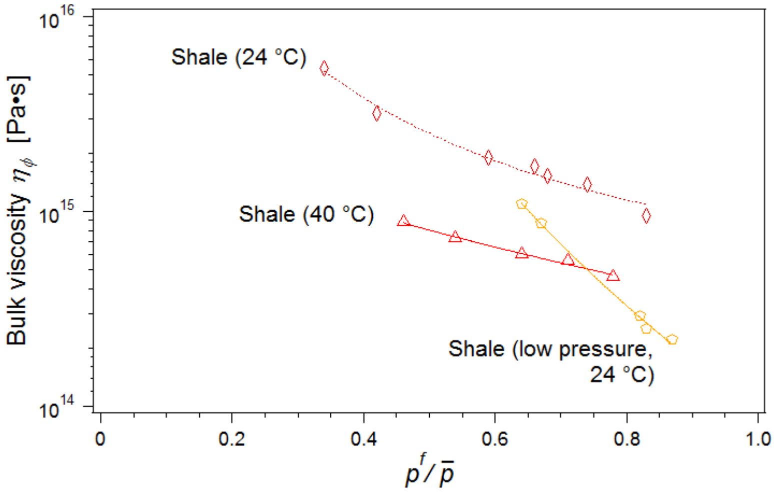

Fig 2. Calculated values of the bulk viscosity of shale plotted as functions of $p^f/\bar{p}$ ratio for the three considered cases: low pressure at 24 ˚C (orange pentagons), high pressure at 24 ˚C (maroon diamonds), and high pressure at 40 ˚C (red triangles).

Additionally, the bulk viscosity calculated for the shale at high pressure at 24 ˚C is plotted against the viscosity trends for two other sedimentary rocks: Berea sandstone and Apulian limestone tested at the same temperature [22] (Fig. 3). Increasing pore pressure at constant mean stress should lead to the increase in porosity if a geomaterial is deforming poroelastically. However, all the tested specimens were experiencing time-dependent compaction and measured volume strains were in agreement with porosity changes predicted by the presented poroviscoelastic relationships, which can be viewed as the model validation.

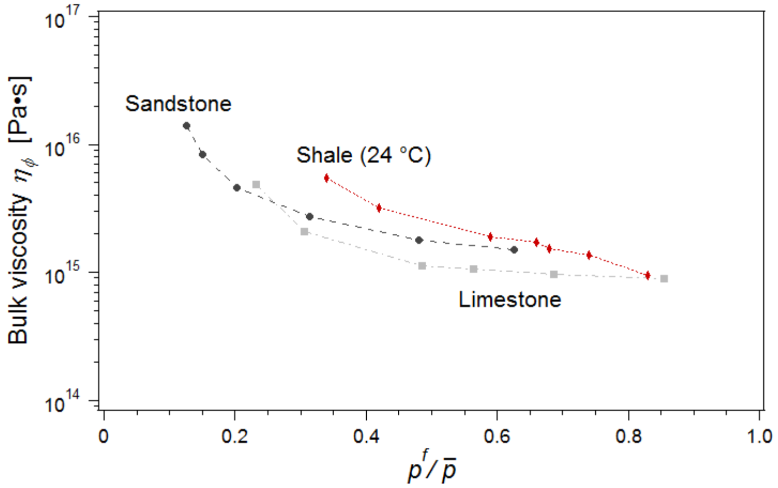

Fig 3. Bulk viscosity of Opalinus clay (maroon diamonds) in comparison to the trends of measured viscosities for Berea sandstone (dark grey circles) and Apulian limestone (light grey squares), all tested at 24 ˚C and plotted as functions of $p^f/\bar{p}$ ratio.

The measurements inferred from the lab are then used to constrain the important parameters of the numerical model. The initial setup (Fig. 4) used for the numerical simulation is a 3D cubic domain of viscoelastically deforming porous media saturated with pore fluid subject to gravity acceleration in the *z* (depth) coordinate. A high porosity horizontal ellipsoid is located at the first quarter of the total depth with porosity values twice higher than the background value. This setup should represent the analogy of a buoyant fluid plume, thus an elevated porosity anomaly, located in a less permeable and less porous reservoir. Porosity evolution through time can be predicted and used to estimate the time and length scale representative for this wave propagation phenomenon.

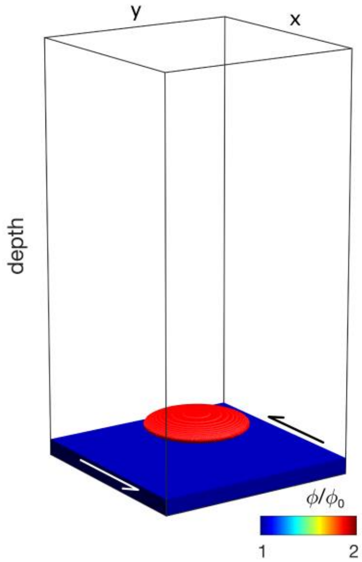

Fig 4. The setup used to model two-phase flow. The resolution is 500 x 500 x 1000 grid points in respectively *x*, *y*, and *z* (depth) dimensions. The domain was decomposed into 64 subdomains, each of them computed on a Nvidia Titan X GPU.

The outcome of the numerical simulations show elongated pipe features developing over time due to highly focused fluid flow through the deforming porous media (Fig. 5). The channel formation, and thus asymmetry in decompaction versus compaction rates is the result of viscosity dependence on $p^f/\overline{p}$ ratio. The effective viscosity drops in region where the pore fluid pressure gets closer to the total stress (red areas on the channel tip in Fig. 5). The created channels are referred to porosity waves, as the solid grains only get displaced very locally, allowing the fluid to go through the porous media in a wave like motion. The associated fluid pressure (Fig. 5) and its gradient will tend to move fluid from the near channel region into the channels. This mechanism enhances the self-sustainability of the porosity wave by providing significant amount of surrounding fluid to flow into the channel. The surrounding fluid being expelled from the near channel areas, the walls of the pipe compact as result of mass balance. The resulting channels wall bulk and shear viscosities increase, freezing their shape over time. The expression of this mechanism in natural system such shallow reservoirs can be related to seismic chimneys visible on seismic surveys cross section [14, 23].

Using the laboratory data on shale behavior, we can scale the numerical simulation in order to predict propagation velocities of the high porosity, thus high permeability channels. Permeability increase inside the channels is of more than three orders of magnitude, enabling pore fluid or brine to travel with a vertical speed proportionally to permeability increase (i.e. three orders of magnitude), instead of the background Darcian flow regime. The characteristic time *t** and length *L** are given by

$$t^* = \sqrt{\frac{\eta_\phi \mu}{k}} (\Delta\rho g)^{-1} \tag{8}$$

$$L^* = \sqrt{\frac{\eta_\phi k}{\mu}} \tag{9}$$

The travelling velocity for the porosity waves through the domain (in meters per year) can be computed as

$$V_{porosity\_wave} = \frac{L_{run} \cdot L^*}{t_{run} \cdot t^*} 3600 \cdot 24 \cdot 365 \quad \text{[m/year]} \tag{10}$$

where L_{run}/t_{run} is the dimensionless velocity obtained from the numerical simulation. Finally, the porosity wave velocity calculated using the poroviscoelastic properties of Opalinus clay appears to be on the order of centimeters per year for a very low permeable (~10^{-20} m^2) formation.

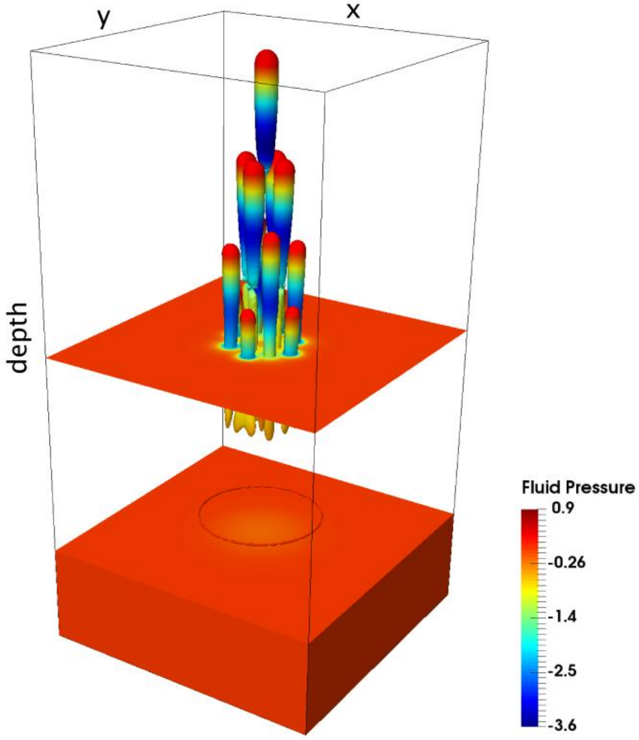

Fig 5. Fluid pressure values plotted on top of the isosurface values of normalised porosity equal to 4 as evolving form the initial high porosity ellipsoid (Fig.1) after dimensionless time of 0.024. Low fluid pressure values are observed within the high porosity channels. Box dimensions are 30 x 30 x 60 compaction lengths in *x*, *y*, and *z* directions respectively, or a numerical resolution of 500 x 500 x 1000 grid points. The visualisation is performed in parallel on 64 Titan X GPUs using the ParaView software in a remote client-server configuration on the *octopus* GPU cluster.

5. Conclusions

We show that viscous effect should not be excluded when assessing long-term behavior of clay-rich materials, such as shales. The modeling results using parameters from the laboratory experiments on low-permeable shale predict that nonlinear porosity-dependent permeability can increase up to three orders of magnitude within the porosity waves. Long-term projections for storage behavior should therefore include time-dependent (viscous) deformation of the potential caprocks.

Laboratory measurements performed to obtain both the permeability and viscosity values for the clay-rich rock types dramatically influence the prediction for the relevance of in-channel formation and propagation. Orders of magnitude changes in permeability will lead to proportionally faster or slower propagation velocities, as this quantity scales the dimensionless velocity of the model. Significantly low effective viscosity values obtained from the laboratory experiments dramatically decrease the characteristic propagation time of the fluid focusing instabilities. This might lead to the generation and propagation of high permeability tubular features in an operational time scale. The viscous or creep effect should therefore be considered while assessing storage integrity, especially for systems where clay-rich caprock formations are investigated. Under certain conditions, creeping ductile rock may locally flow away, leading to the formation of the vertical pipes of high permeability and porosity.

Acknowledgements

Opalinus clay cores were provided by Swisstopo in the framework of Mont Terri Project, CS-C experiment. R. Makhnenko acknowledges the support from SCCER-SoE (Switzerland) grant KTI.2013.288 and Swiss Federal Office of Energy (SFOE) project CAPROCK #810008154.

References

[1] IEAGHG. Caprock systems for CO_2 geological storage. IEA Environmental Projects Ltd 2011.

[2] Amann-Hildenbrand A, Bertier P, Busch A, Krooss BM. Experimental investigation of the sealing capacity of generic clay-rich caprocks. International Journal of Greenhouse Gas Control 2013;19:620-641.

[3] Boulin PF, Bretonnier P, Vassil V, Samouillet A, Fleury M, Lombard J-M. Sealing efficiency of caprocks: Experimental investigation of entry pressure measurement methods. Marine and Petroleum Geology 2013;48:20-30.

[4] Makhnenko RY, Vilarrasa V, Mylnikov D, Laloui L. Hydromechanical aspects of CO_2 breakthrough into clay-rich caprocks. Energy Procedia 2017 (this issue).

[5] Simon NSC. Compaction Driven Flow in Porosity Waves - A Threat to Caprock Integrity? Third EAGE CO2 Geological Storage Workshop 2012.

[6] Zhang C-L, Rothfuchs T, Su K, Hoteit N. Experimental study of the thermohydro-mechanical behaviour of indurated clays. Physics & Chemistry of Earth 2007; 32:957 – 965.

[7] Yang DS, Bornert M, Chanchole S. Experimental investigation of the delayed behaviour of unsaturated argillaceous rocks by means of Digital Image Correlation techniques. Applied Clay Sciences 2011; 54, 53–62.

[8] Sone H, Zoback MD. Time-dependent deformation of shale gas reservoir rocks and its long-term effect on in-situ state of stress. International Journal of Rock Mechanics & Mining Sciences 2014; 69:120-132.

[9] Elsworth D, Yasuhara H. Short-timescale chemo-mechanical effects and their influence on transport properties of fractured rock. Pure & Applied Geophysics 2006; 163:2051-2070.

[10] Bürgmann R, Dresen G. Rheology of the lower crust and upper mantle: Evidence from rock mechanics, geodesy, and field observations. Annual Review of Earth and Planetary Sciences 2008; 36(1):531.

[11] Brantut N, Heap MJ, Meredith PG, Baud P. Time-dependent cracking and brittle creep in crustal rocks: A review. Journal of Structural Geology 2013; 52:17-43.

[12] Connolly JAD, Podladchikov YY. An analytical solution for solitary porosity waves: dynamic permeability and fluidization of nonlinear viscous and viscoplastic rock. Geofluids 2015; 15(1‐2):269‐292.

[13] Yarushina VM, Podladchikov YY, Connolly JAD. (De)compaction of porous viscoelastoplastic media: Solitary porosity waves. Journal of Geophysical Research Solid Earth 2015; 120:4843-4862.

[14] Räss L, Yarushina VM, Simon NS, Podladchikov YY. Chimneys, channels, pathway flow or water conducting features-an explanation from numerical modelling and implications for CO_2 storage. Energy Procedia 2014; 63:3761-3774.

[15] Yarushina VM, Podladchikov YY. (De)compaction of porous viscoelastoplastic media: Model formulation, Journal of Geophysical Research Solid Earth 2015; 120:4146–4170.

[16] Wang HF, Theory of Linear Poroelasticity with Applications to Geomechanics and Hydrogeology. Princeton University Press 2000.

[17] Connolly JAD, Podladchikov YY. Decompaction weakening and channeling instability in ductile porous media: Implications for asthenospheric melt segregation. Journal of Geophysical Research Solid Earth 2007; 112:B10.

[18] Detournay E, Cheng A. Fundamentals of poroelasticity. In Fairhurst C (ed.) Chap. 5 in Comprehensive Rock Engineering: Principles, Practice and Projects, Vol. II, Analysis and Design Methods, Pergamon Press, Oxford 1993; pp. 113 – 171.

[19] Skempton AW. The pore-pressure coefficients A and B. Geotechnique 1954; 4:143-147.

[20] Makhnenko RY, Labuz JF. Elastic and inelastic deformation of fluid-saturated rock. Philosophycal Transactions of Royal Society A 2016; 374:20150422.

[21] Makhnenko RY, Labuz JF. Saturation of porous rock and measurement of the *B* coefficient. In Proceedings of the 47th U.S. Rock Mechanics/ Geomechanics Symposium, San Francisco, CA 23-26 June 2013; paper No. 468.

[22] Makhnenko RY, Podladchikov YY. Experimental poroviscoelasticity of common sedimentary rocks. In preparation 2017.

[23] Räss L, Yarushina V, Duretz T, Podladchikov Y. High-resolution numerical modeling to resolve the dynamics of pipe structures in porous media. EAGE ECMOR X conference 2016, Amsterdam.

[24] Scientific Computing Group, specification of the octopus GPU cluster. 2015: http://wp.unil.ch/geocomputing/computing-systems/octopus/

[25] Bossart P. Characteristics of the Opalinus Clay at Mont Terri. 2012: http:/mont-terri.ch/internet/montterri/de/home/geology/key_characteristics.html.

[26] Pearson FJ. PC experiment: recipe for artificial pore water. Mont Terri Project, Technical Note 2002-17.

[27] Zimmerman RW. Compressibility of sandstones. Elsevier, New York 1991.

Available online at www.sciencedirect.com

ScienceDirect

Energy Procedia 00 (2017) 000–000

Energy Procedia

www.elsevier.com/locate/procedia

13th International Conference on Greenhouse Gas Control Technologies, GHGT-13, 14-18 November 2016, Lausanne, Switzerland

Potential for Fault Reactivation due to CO_2 Injection in a Semi-Closed Saline Aquifer

Victor Vilarrasa[a,b]*, Roman Y. Makhnenko[a,c], Lyesse Laloui[a]

[a]Laboratory of Soil Mechanics, École Polytechnique Fédérale de Lausanne, EPFL ENAC IIC LMS, GC – Station 18, 1015 Lausanne, Switzerland
[b]Institute of Environmental Assessment and Water Research, Spanish National Research Council (IDAEA-CSIC), Jordi Girona 18-26, 08034 Barcelona, Spain
[c]Department of Civil & Environmental Engineering, University of Illinois at Urbana-Champaign, 205 North Mathews Ave, Urbana, IL, 61801-2352, USA

Abstract

CO_2 injection in extensive saline aquifers that present no faults is unlikely to damage the caprock sealing capacity. In contrast, CO_2 injection in closed reservoirs will induce a large pressure buildup that may reactivate the low-permeable faults that bound the reservoir. However, the vast majority of CO_2 storage formations will be extensive saline aquifers bounded by a limited number of low-permeable faults. Such storage formations have received little attention and are the focus of this study. We model an extensive aquifer bounded by a heterogeneous low-permeable fault on one side and having open boundaries on the other sides. Simulation results show that the storage formation pressurizes between the injection well and the low-permeable fault, causing total stress changes and effective stress reduction around the fault. These changes lead to yielding of the fault core that is next to the lower half of the storage formation when injecting in the hanging wall. The yield of the fault core would induce a sequence of microseismic events with accumulated seismic moment equivalent to an earthquake of magnitude 1.7, which would not be felt on the ground surface and would not enhance permeability of the ductile clay-rich fault.

Keywords: geomechanics; induced seismicity; overpressure; hydro-mechanical coupling

---

* Corresponding author. Tel.: +34-93-400-6100; fax: +34-93-204-5904.
E-mail address: victor.vilarrasa@upc.edu

1. Introduction

Large volumes of carbon dioxide (CO_2) will be injected in deep saline aquifers to mitigate climate change, inducing pressure buildup that may lead to fault reactivation. Failure conditions are unlikely to be reached in extensive aquifers [1]. As a result, the caprock sealing capacity will be maintained and CO_2 leakage across the caprock is improbable. However, in closed aquifers, overpressure will rapidly increase once the pressure perturbation cone reaches low-permeable boundaries of the aquifer [2, 3]. Thus, failure conditions may eventually be met in the low-permeable faults that bound aquifers. Fault reactivation may induce seismic events [4, 5], which could be potentially felt at the ground surface [6] and cause public opposition that may end up with the closure of CO_2 storage projects, as already occurred after the induced earthquakes in a geothermal project at Basel, Switzerland [7]. Thus, fault reactivation that could lead to felt induced seismicity should be avoided to achieve a successful deployment of CO_2 storage projects.

The vast majority of suitable storage formations will neither be extensive aquifers nor closed aquifers, but will correspond to relatively extensive aquifers bounded by a limited number of low-permeable faults [8-10]. However, this kind of aquifers has received limited attention and needs further consideration. The numerical models used for studying fault reactivation usually represent closed aquifers in which CO_2 injection induces a high overpressure [e.g., 11, 12]. Such models may be representative of compartmentalized reservoirs [13, 14], which can rapidly reach their storage capacity due to overpressure limitations [15, 16]. Nevertheless, in the presence of a limited number of low-permeable barriers or if the permeability across faults is relatively high, pressure builds up at a lower rate [17], and thus, fault reactivation may not be an issue.

In this study, we model an extensive aquifer bounded by a low-permeable fault on one side and having open boundaries on the other sides. First, we present the geometry and material properties of the considered model. Then, we analyze the effect of fault permeability on the potential of fault reactivation and discuss the implications for geologic carbon storage projects. Finally, we draw the conclusions of this study.

2. Methods

A schematic representation of the numerical model, which includes a fault on one side of the injection well, is shown in Fig. 1. On the other side of the well, the model extends laterally for 20 km, so that the boundary does not have any effect on the evolution of overpressure for the considered duration of CO_2 injection. The fault has an offset of 25 m and the aquifer has a thickness of 50 m. Therefore, half of the aquifer is still connected except for the presence of the fault. CO_2 is injected with a constant mass flow rate through a horizontal well on the hanging wall of the fault. The model is a 2D cross section, with plane strain symmetry given by the horizontal injection well, which injects $2.0 \cdot 10^{-3}$ kg/s of CO_2 per meter normal to the model during half a year. Initial pore pressure is hydrostatic and equal to 15 MPa at the top of the reservoir, which is placed at 1.5 km deep. The stress state corresponds to a normal faulting stress regime, in which the vertical stress has a gradient of 23 MPa/km and the horizontal stresses are 70 % of the vertical stress. The fault dips 60º, so it is critically oriented in normal faulting stress regimes [18].

We solve this hydro-mechanical problem using the fully coupled finite element code CODE_BRIGHT [19, 20], extended for CO_2 injection [21, 22]. To simulate CO_2 injection, mass and momentum conservation of each phase, i.e., CO_2 and brine, have to be solved. Momentum conservation in porous media is given by Darcy's law. Mass conservation of these two fluids is given by [23],

$$\frac{\partial(\varphi S_\alpha \rho_\alpha)}{\partial t} + \nabla \cdot (\rho_\alpha \mathbf{q}_\alpha) = 0, \qquad \alpha = c, w, \tag{1}$$

where φ [$L^3\ L^{-3}$] is porosity, S_α [–] is saturation of α -phase, ρ_α [$M\ L^{-3}$] is density of α -phase, t [T] is time, and $\mathbf{q}_\alpha$ [$L^3\ L^{-2}\ T^{-1}$] is the volumetric flux of α -phase. To account for the hydro-mechanical coupling, the momentum balance of the solid phase is solved simultaneously. If inertial terms are neglected, the momentum balance reduces to the equilibrium of stresses

$$\nabla \cdot \boldsymbol{\sigma} + \mathbf{b} = \mathbf{0}\,, \tag{2}$$

where $\boldsymbol{\sigma}$ [M L^{-1} T^{-2}] is the stress tensor and $\mathbf{b}$ [M L^{-2} T^{-2}] is the body forces vector. To assess the potential for fault reactivation, an elasto-plastic behavior of the geomaterials given by the Drucker-Prager yield function is adopted (see [24] for details).

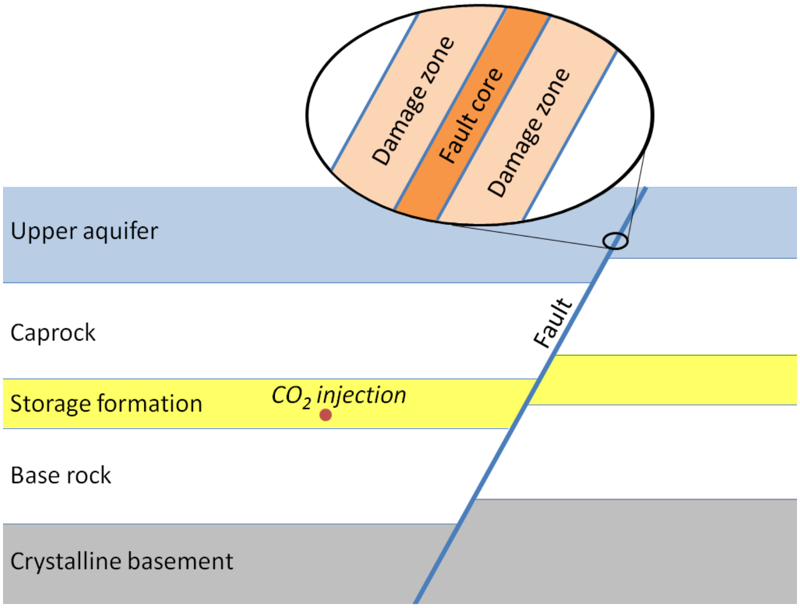

Fig 1. Schematic representation of the model for evaluating the potential of fault reactivation in a semi-closed storage formation.

3. Materials

The aquifer in which CO_2 is injected corresponds to Berea sandstone formation, the caprock and baserock are shales (Opalinus clay), the upper aquifer is the Indiana limestone formation, and the basement is made of Charcoal granite. Tables 1 and 2 include the hydraulic and geomechanical properties for the different rock types and fault, respectively, which have been measured in laboratory experiments at the EPFL or elsewhere [e.g., 25, 26]. Failure properties of shale and granite were adopted from the literature [27, 28], as well as the elastic properties of the granite [29]. CO_2 will flow relatively easy in the storage formation due to its high permeability and low entry pressure. On the other hand, the low permeability and high entry pressure of shale [30] will confine CO_2 in the storage formation and prevent CO_2 leakage through the caprock. The reported values of porosity for the confining layers, crystalline basement, and the fault core are the effective porosities, i.e., those that contribute to flow. Relative CO_2 and water permeabilities are taken as power functions of saturation, with a power of three for the sandstone and the limestone and six for the shale and the granite [31]. Low-permeability (~ 10^{-20} m^2) and relatively low (~ GPa) elastic moduli of caprock and baserock provide characteristic diffusion time for these formations to be ~ 10^9 sec (tens of years), and hence the undrained elastic properties of shale were considered.

The fault is composed by a fault core and a damage zone on both sides of the core (Figure 1). Both the geomechanical and hydraulic properties of the damage zone are different for the sections of the fault that cross clay-rich geomaterials, like the caprock, and siliciclastic or carbonate rocks, like aquifers [32, 33]. Including fault heterogeneity in the hydraulic properties hinders fluid migration if shear slip occurs in the fault [34]. Fault core is made of reconstituted shale, which properties along with the properties of other damaged materials were measured in the laboratory. These characteristics may vary depending on level of damage and applied effective stress. The friction angle of siliciclastic and carbonate rocks, i.e., aquifers, is high, above 30º, but it is low (< 30 º) for clay-rich materials, such as caprock and fault core [29, 30]. Thus, the aquifers are far from being critically stressed, but the clay-rich materials are close to shear failure conditions. Additionally, failure properties of the sandstone and the limestone were found to be intermediate stress-dependent [25, 35], though is not taken into account in the model. With the assumptions of purely drained (for the storage formation, upper aquifer, basement, fault core, and damage zones) or undrained (caprock and baserock) behavior, linear failure properties independent of intermediate stress, and power law type dependence of water and CO_2 permeabilities from the degree of saturation, the introduced model is assumed to be the first order approach to the problem of CO_2 injection in semi-closed aquifers.

Table 1. Hydraulic properties of the geomaterials included in the model.

Formation	Permeability, k (m^2)	Relative water permeability, k_{rw} (-)	Relative CO_2 permeability, k_{rc} (-)	Gas entry pressure, p_0 (MPa)	van Genuchten shape parameter m (-)	Porosity, φ (-)
Storage formation	$4 \cdot 10^{-14}$	S_w^3	S_c^3	0.02	0.8	0.23
Caprock	$8 \cdot 10^{-20}$	S_w^6	S_c^6	1.5	0.3	0.05
Base rock	$5 \cdot 10^{-20}$	S_w^6	S_c^6	1.5	0.3	0.05
Upper aquifer	$1 \cdot 10^{-14}$	S_w^3	S_c^3	0.20	0.8	0.13
Crystalline basement	$4 \cdot 10^{-20}$	S_w^6	S_c^6	12.0	0.3	0.01
Fault core	$1 \cdot 10^{-19}$	S_w^6	S_c^6	4.0	0.3	0.10
Damage zone reservoirs	$2 \cdot 10^{-13}$	S_w^3	S_c^3	0.02	0.8	0.25
Damage zone confinement layers	$1.5 \cdot 10^{-19}$	S_w^6	S_c^6	5.0	0.3	0.09
Damage zone basement	$1 \cdot 10^{-16}$	S_w^4	S_c^4	1.0	0.5	0.07

Table 2. Geomechanical properties of the geomaterials included in the model.

Formation	Young's modulus, E (GPa)	Poisson ratio, ν(-)	Cohesion, c' (MPa)	Friction angle, ϕ (º)
Storage formation	14.0	0.31	9	42
Caprock	2.8	0.40	6	24
Base rock	3.0	0.39	6	24
Upper aquifer	28.0	0.21	12	31
Crystalline basement	55.0	0.18	60	30
Fault core	1.0	0.30	0	24
Damage zone reservoirs	7.0	0.35	0	30
Damage zone confinement layers	1.4	0.42	0	24
Damage zone basement	42.0	0.30	0	30

4. Results

CO_2 injection in the presence of a low-permeable fault causes an additional pressurization of the aquifer in the region comprised between the well and the fault (Fig. 2a). However, on the other side of the injection well, the resident brine can migrate away from it without finding any flow barrier. This flow pattern leads to pressurization near the fault that is slower than the one that would occur in a closed aquifer. Nevertheless, fluid pressure tends to increase, and thus, failure conditions at the fault may be reached if the injection flow rate is maintained constant. Overpressure causes a decrease of the effective stresses, but also induces changes in the total stresses around the fault that may compromise fault stability (Fig. 2b-2d).

In our model, the onset of plastic strain (or yield that is taken here as a failure point for clay-rich fault) occurs after 40 days of injection. Plastic strain accumulates with time, mainly within the fault core coinciding with the lower half of the storage formation, as shown in Fig. 2e. The length of the fault core that undergoes plastic strain is of 20 m, with a magnitude close to 1%, which yields a mean slip of 0.15 m. The seismic moment can be estimated as the product of the shear modulus of the fault core, the mean slip, and the rupture area. Once the seismic moment is known, the magnitude of the induced earthquake can be calculated using the relationship proposed by Kanamori and Anderson [36]

$$M = \log_{10} \frac{M_0}{1.5} - 10.73, \tag{3}$$

where $M_0 = GAd$ is the seismic moment, G is the shear modulus, A is the rupture area, and d is the mean slip. Assuming that the rupture of the fault extends over the whole length of the injection well and a 2 km long horizontal well, the resulting magnitude of the simulated induced earthquake is 1.7. Since the magnitude is lower than 2, such event would not be felt on the surface and thus, it would be considered as a microseismic event. Such magnitude is similar to the maximum magnitude of the microseismic events that were recorded at In Salah storage site [37].

Figure 3 shows the stress path for the fault core material in deviatoric stress – mean effective stress diagram. Initially, the stress state is close to the yield surface. As overpressure increases due to CO_2 injection, the mean effective stress is reduced, approaching the yield surface. At certain moment (40 days of injection), the stress state touches the yield surface (Fig. 4) and plastic strain starts to develop. Within the framework of the considered model, fluid pressure continues to build up, decreasing the mean effective stress further, but the deviatoric stress evolves by maintaining the stress state on the yield surface (Fig. 3).

5. Discussion

One of the main issues related to geologic carbon storage is felt induced seismicity caused by fault reactivation. On the one hand, fault reactivation may enhance fault permeability and open up migration paths that may lead to CO_2 leakage [5]. However, the hydraulic properties of faults in the reservoir-caprock sequences where CO_2 is planned to be stored are highly heterogeneous, which significantly hinders upward CO_2 flow due to the presence of materials with high gas entry pressure [34]. On the other hand, felt seismic events may cause public opposition that may end up with the closure of CO_2 storage projects, as already occurred with a geothermal project at Basel in which several induced earthquakes were felt by the local population [7].

The earthquake that would be induced with the accumulated plastic strain simulated in our model (magnitude 1.7) is not enough to be felt on the surface. Furthermore, rather than a single event, the fault would likely rupture in a sequence of multiple microseismic events. Thus, the simulated fault reactivation would not cause any nuisances to the local population. Additionally, with on-site microseismic monitoring, correction measures on the flow rate could have been applied to halt fault reactivation.

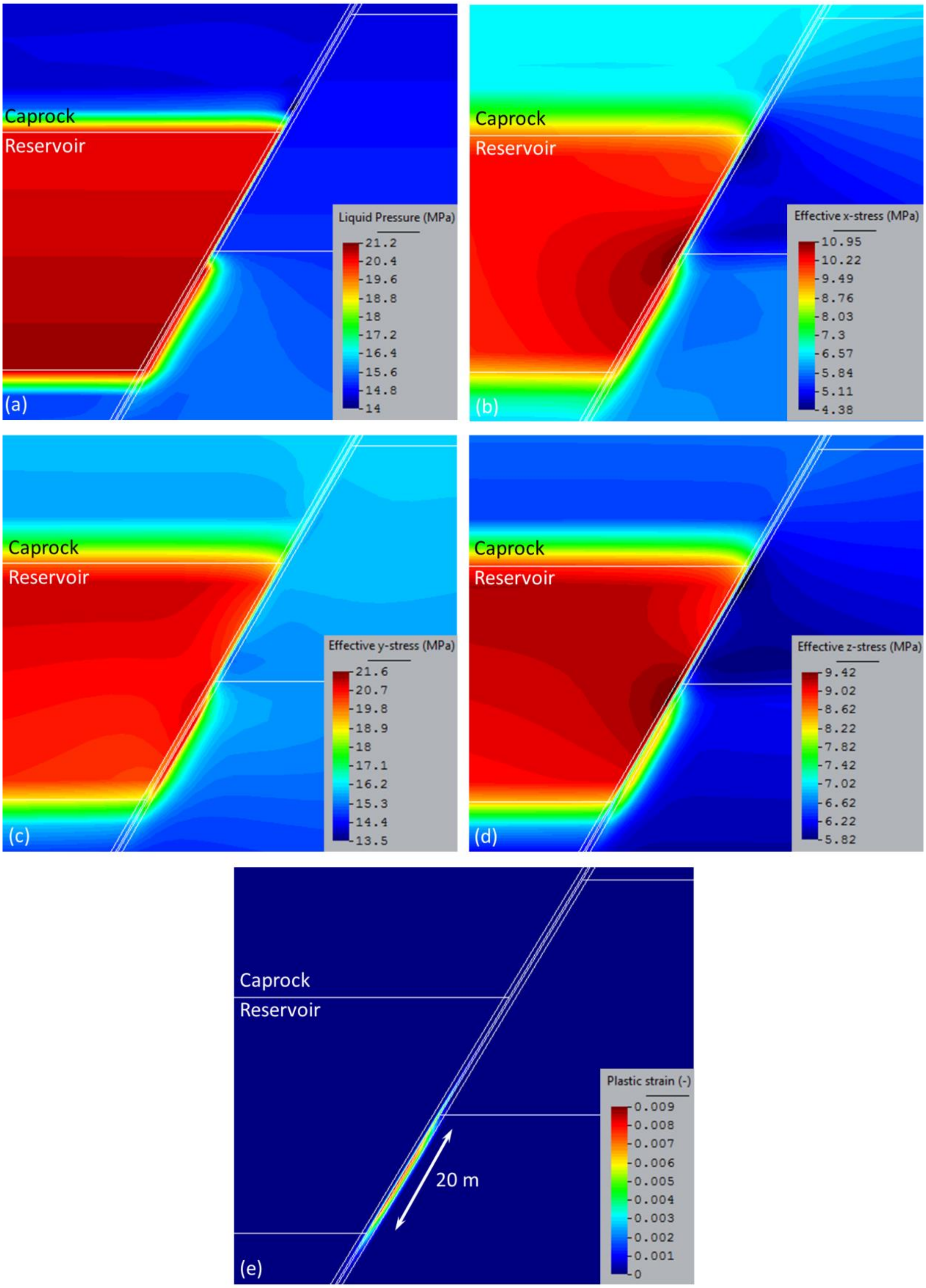

Fig 2. (a) Liquid pressure, (b) effective maximum horizontal stress (in-plane direction), (c) effective vertical stress, (d) effective minimum horizontal stress (out-of-plane direction) and (e) plastic strain after half a year of CO_2 injection.

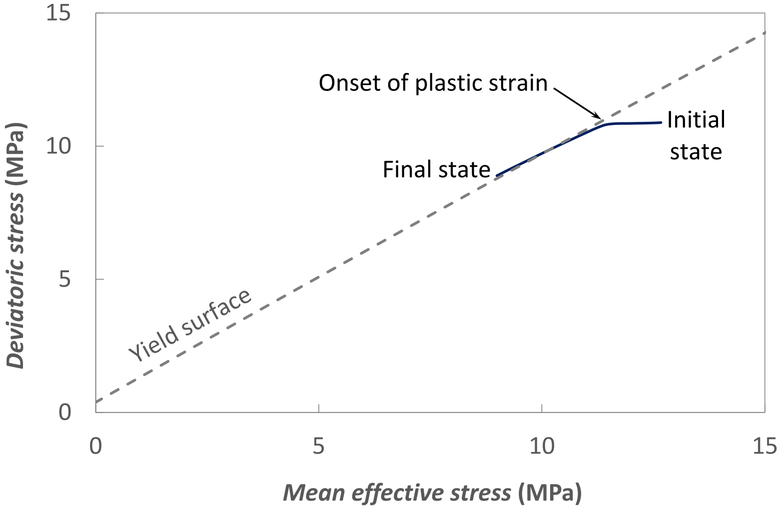

Fig 3. Deviatoric stress versus mean effective stress trajectory of the fault core during half a year of CO_2 injection.

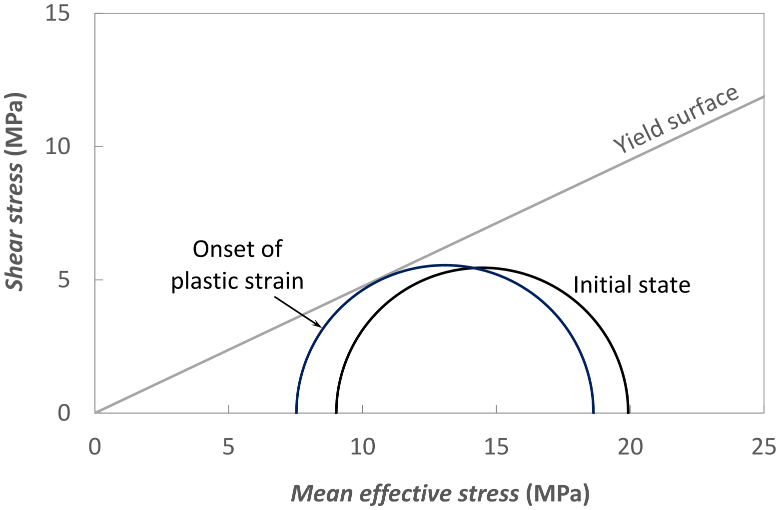

Fig 4. Mohr circles at the fault core prior to injection and at the onset of plastic strain due to CO_2 injection.

Our model includes the heterogeneity that is expected in faults that cross reservoir-caprock sequences in sedimentary basins. We consider a clay-rich fault core and a damage zone on both sides of the fault core and these damage zones are different for each layer. We have based the material properties on laboratory measurements of rocks representative of each geomaterial included in the numerical model. Still, the values of some of the properties that we have used in our model may vary significantly with the stress state and rock type. In particular, fault permeability may differ by several orders of magnitude depending on its structure, i.e., if the fault is a conduit instead of a flow barrier [38].

Another key aspect of induced seismicity is how friction coefficient of the fault evolves once shear failure conditions are reached. In our model, failure conditions do not propagate along the fault inducing a large earthquake, as could be the case if a strain-softening model is implemented [39]. Such kind of behavior may occur in brittle materials, but it is unlikely in faults with a high clay content due to their ductility. In particular, faults with high clay content may accumulate plastic strain aseismically [40], avoiding the brittle behavior that may trigger large magnitude seismic events. Further investigation on the behavior of clay rich faults is required to reduce the existing uncertainties on the response of faults to CO_2 injection.

Previous studies on fault reactivation considered CO_2 injection into a closed reservoir [e.g., 4, 6, 11]. We model a semi-closed reservoir, which is bounded only on one side. Even though pressure buildup is slower than in a closed reservoir, simulation results suggest that shear failure conditions will eventually be reached on the fault if the injection rate is maintained constant. Since low-permeable faults are expected to be present in extensive saline aquifers, a good characterization to map existing faults and a proper monitoring during CO_2 injection are needed to minimize the risk of fault reactivation that may lead to felt induced seismicity.

6. Conclusions

We model CO_2 injection in a semi-closed aquifer bounded by a low-permeable fault. We include heterogeneity in the structure of the fault, accounting for a fault core and a damage zone on both sides of the core that have different material properties depending on the rock layer they are in contact with, i.e., reservoirs, confining layers, or crystalline basement. Though there is not an excessive overpressure on the side of the storage formation where there is no fault because the resident brine can easily migrate away from the injection well, the low-permeability of the fault induces pressurization of the storage formation between the well and the fault. This pressurization causes total stress changes around the fault and reduces the effective stresses, leading to yield conditions in the fault core. Simulation results show that, when injecting in the hanging wall of the fault, plastic strain accumulates along 20 m in the fault core, coinciding with the lower half of the storage formation in the hanging wall. This plastic strain would cause a sequence of microseismic events with a cumulative moment magnitude equivalent to an earthquake of magnitude 1.7. Such low magnitude would not be felt at the ground surface and, according to laboratory experiments, would not enhance permeability of the ductile clay-rich fault.

Acknowledgements

V.V. acknowledges support from the 'EPFL Fellows' fellowship programme co-funded by Marie Curie, FP7 Grant agreement no. 291771. R.M. activities are sponsored by SCCER-SoE (Switzerland) grant KTI.2013.288 and Swiss Federal Office of Energy (SFOE) project CAPROCK #810008154.

References

[1] Vilarrasa, V, Carrera J. Geologic carbon storage is unlikely to trigger large earthquakes and reactivate faults through which CO_2 could leak. Proceedings of the National Academy of Sciences 2015; 112(19):5938-43.

[2] Zhou Q, Birkholzer JT, Tsang CF, Rutqvist J. A method for quick assessment of CO_2 storage capacity in closed and semi-closed saline formations. International Journal of Greenhouse Gas Control 2008; 2(4):626-39.

[3] Mathias SA, de Miguel GJGM, Thatcher KE, Zimmerman RW. Pressure buildup during CO_2 injection into a closed brine aquifer. Transport in Porous Media 2011; 89(3):383-97.

[4] Cappa F, Rutqvist J. Impact of CO_2 geological sequestration on the nucleation of earthquakes. Geophysical Research Letters 2011; 38(17), L17313, doi:10.1029/2011GL048487.

[5] Rinaldi AP, Vilarrasa V, Rutqvist J, Cappa F. Fault reactivation during CO_2 sequestration: Effects of well orientation on seismicity and leakage. Greenhouse Gases: Science and Technology 2015; 5(5):645-56.

[6] Cappa F, Rutqvist J. Seismic rupture and ground accelerations induced by CO_2 injection in the shallow crust. Geophysical Journal International 2012; 190(3):1784-9.

[7] Häring MO, Schanz U, Ladner F, Dyer BC. Characterisation of the Basel 1 enhanced geothermal system. Geothermics 2008; 37(5):469-95.

[8] Hitchon B, Gunter WD, Gentzis T, Bailey RT. Sedimentary basins and greenhouse gases: a serendipitous association. Energy Conversion and Management 1999; 40(8):825-43.

[9] Bachu S. Screening and ranking of sedimentary basins for sequestration of CO_2 in geological media in response to climate change. Environmental Geology 2003; 44(3):277-89.

[10] Verdon JP, Kendall JM, Stork AL, Chadwick RA, White DJ, Bissell RC. Comparison of geomechanical deformation induced by megatonne-scale CO_2 storage at Sleipner, Weyburn, and In Salah. Proceedings of the National Academy of Sciences 2013; 110(30):E2762-71.

[11] Cappa F, Rutqvist J. Modeling of coupled deformation and permeability evolution during fault reactivation induced by deep underground injection of CO_2. International Journal of Greenhouse Gas Control 2011; 5(2):336-46.

[12] Mazzoldi A, Rinaldi AP, Borgia A, Rutqvist J. Induced seismicity within geological carbon sequestration projects: maximum earthquake magnitude and leakage potential from undetected faults. International Journal of Greenhouse Gas Control 2012; 10:434-42.

[13] Vidal-Gilbert S, Tenthorey E, Dewhurst D, Ennis-King J, Van Ruth P, Hillis R. Geomechanical analysis of the Naylor Field, Otway Basin, Australia: Implications for CO_2 injection and storage. International Journal of Greenhouse Gas Control 2010; 4(5):827-39.

[14] Castelletto N, Gambolati G, Teatini P. Geological CO_2 sequestration in multi-compartment reservoirs: Geomechanical challenges. Journal of Geophysical Research: Solid Earth 2013; 118(5):2417-28.

[15] Szulczewski ML, MacMinn CW, Herzog HJ, Juanes R. Lifetime of carbon capture and storage as a climate-change mitigation technology. Proceedings of the National Academy of Sciences 2012; 109(14):5185-9.

[16] Hansen O, Gilding D, Nazarian B, Osdal B, Ringrose P, Kristoffersen JB, Eiken O, Hansen H. Snøhvit: the history of injecting and storing 1 Mt CO_2 in the Fluvial Tubåen Fm. Energy Procedia 2013; 37:3565-73.

[17] Tillner E, Langer M, Kempka T, Kühn M. Fault damage zone volume and initial salinity distribution determine intensity of shallow aquifer salinisation in subsurface storage. Hydrology and Earth System Sciences 2016; 20(3):1049-67.

[18] Vilarrasa V, Carrera J, Olivella S. Hydromechanical characterization of CO_2 injection sites. International Journal of Greenhouse Gas Control 2013; 19:665-77.

[19] Olivella S, Carrera J, Gens A, Alonso EE. Nonisothermal multiphase flow of brine and gas through saline media. Transport in Porous Media 1994; 15(3):271-93.

[20] Olivella S, Gens A, Carrera J, Alonso EE. Numerical formulation for a simulator (CODE_BRIGHT) for the coupled analysis of saline media. Engineering Computations 1996; 13(7):87-112.

[21] Vilarrasa V, Bolster D, Olivella S, Carrera J. Coupled hydromechanical modeling of CO_2 sequestration in deep saline aquifers. International Journal of Greenhouse Gas Control 2010; 4(6):910-9.

[22] Vilarrasa V, Silva O, Carrera J, Olivella S. Liquid CO_2 injection for geological storage in deep saline aquifers. International Journal of Greenhouse Gas Control 2013; 14:84-96.

[23] Bear J (ed.). *Dynamics of fluids in porous media*. Elsevier, New York, 1972.

[24] Vilarrasa V, Olivella S, Carrera J. Geomechanical stability of the caprock during CO_2 sequestration in deep saline aquifers. Energy Procedia 2011; 4:5306-13.

[25] Makhnenko RY, Labuz JF. Plane strain testing with passive restraint. Rock Mechanics Rock Engineering 2014; 47(6):2021-29.

[26] Makhnenko RY, Labuz JF. Elastic and inelastic deformation of fluid-saturated rock. Philosophycal Transactions of Royal Society A 2016; 374:20150422.

[27] Heuze F. Scale effects in the determination of rock mass strength and deformability. Rock Mechanics 1980; 12:167-92.

[28] Gräsle W. Multistep triaxial strength tests: investigating strength parameters and pore pressure effects on Opalinus clay. Physics and Chemistry of the Earth 2011; 36: 1898-1904.

[29] Labuz JF, Biolzi L. Characteristic strength of quasi-brittle materials. International Journal of Solids & Structures 1998; 35(31-32): 4191-203.

[30] Mylnikov D, Makhnenko RY, Vilarrasa V, Laloui L. Hydromechanical aspects of CO_2 breakthrough into clay-rich caprocks. Energy Procedia 2017 (this issue).

[31] Bennion B, Bachu S. Drainage and imbibition relative permeability relationships for supercritical CO_2/brine and H_2S/brine systems in intergranular sandstone, carbonate, shale, and anhydrite rocks. SPE Reservoir Evaluation & Engineering 2008; 11(03):487-96.

[32] Billi A, Salvini F, Storti F. The damage zone-fault core transition in carbonate rocks: implications for fault growth, structure and permeability. Journal of Structural Geology 2003; 25(11):1779-94.

[33] Egholm DL, Clausen OR, Sandiford M, Kristensen MB, Korstgård JA. The mechanics of clay smearing along faults. Geology 2008; 36(10):787-90.

[34] Rinaldi AP, Jeanne P, Rutqvist J, Cappa F, Guglielmi Y. Effects of fault-zone architecture on earthquake magnitude and gas leakage related to CO_2 injection in a multi-layered sedimentary system. Greenhouse Gases: Science and Technology 2014; 4(1):99-120.

[35] Makhnenko RY, Harvieux J, Labuz JF. Paul-Mohr-Coulomb failure surface of rock in the brittle regime. Geophysical Research Letters 2015; 42:6975-81.

[36] Kanamori H, Anderson DL. Theoretical basis of some empirical relations in seismology. Bulletin of the Seismological Society of America 1975; 65(5):1073-95.

[37] Stork AL, Verdon JP, Kendall JM. The microseismic response at the In Salah Carbon Capture and Storage (CCS) site. International Journal of Greenhouse Gas Control 2015; 32:159-71.

[38] Caine JS, Evans JP, Forster CB. Fault zone architecture and permeability structure. Geology 1996; 24(11):1025-8.

[39] Rutqvist J, Rinaldi AP, Cappa F, Jeanne P, Mazzoldi A, Urpi L, Guglielmi Y, Vilarrasa V. Fault activation and induced seismicity in geologic carbon storage - Lessons learned from recent modeling studies. Journal of Rock Mechanics and Geotechnical Engineering 2016; doi: 10.1016/j.jrmge.2016.09.001.

[40] Guglielmi Y, Cappa F, Avouac JP, Henry P, Elsworth D. Seismicity triggered by fluid injection–induced aseismic slip. Science 2015; 348(6240):1224-6.